

Numerical Analysis and Parameter Optimization of Portable Oscillating-Body Wave Energy Converters

Joseph Capper

Thesis submitted to the faculty of the Virginia Polytechnic Institute and State University in partial fulfillment of the requirements for the degree of

Master of Science
In
Mechanical Engineering

Lei Zuo, Chair
Rui Qiao
Shihong Lin

May 12, 2021
Blacksburg, VA

Keywords: Wave Energy Converter (WEC), Oscillating Surge Wave Energy Converter (OSWEC), Wave Attenuator, Seawater Desalination, Geometry Optimization, Resonance Tuning, Power Maximization

Numerical Analysis and Parameter Optimization of Portable Oscillating-Body Wave Energy Converters

Joseph Capper

ACADEMIC ABSTRACT

As a clean, abundant, and renewable source of energy with a strategic location in close proximity to global population regions, ocean wave energy shows major promise. Although much wave energy converter development has focused on large-scale power generation, there is also increasing interest in small-scale applications for powering the blue economy. In this thesis, the objective was to optimize the performance of small-sized, portable, oscillating-body wave energy converters (WECs). Two types of oscillating body WECs were studied: bottom hinged and two-body attenuator. For the bottom-hinged device, the goal was to show the feasibility of an oscillating surge WEC and desalination system using numerical modeling to estimate the system performance. For a 5-day test period, the model estimated 517 L of freshwater production with 711 ppm concentration and showed effective brine discharge, agreeing well with preliminary experimental results.

The objective for the two-body attenuator was to develop a method of power maximization through resonance tuning and numerical simulation. Three different geometries of body cross sections were used for the study with four different drag coefficients for each geometry. Power generation was maximized by adjusting body dimensions to match the natural frequency with the wave frequency. Based on the time domain simulation results, there was not a significant difference in power between the geometries when variation in drag was not considered, but the elliptical geometry had the highest power when using approximate drag coefficients. Using the two degree-of-freedom (2DOF) model with approximate drag coefficients, the elliptical cross section had a max power of 27.1 W and 7.36% capture width ratio (CWR) for regular waves and a max power of 8.32 W and 2.26% CWR for irregular waves. Using the three degree-of-freedom (3DOF) model with approximate drag coefficients, the elliptical cross section had a max power of 22.5 W and 6.12% CWR for regular waves and 6.18 W and 1.68% CWR for irregular waves. A mooring stiffness study was performed with the 3DOF model, showing that mooring stiffness can be increased to increase relative motion and therefore increase power.

Numerical Analysis and Parameter Optimization of Portable Oscillating-Body Wave Energy Converters

Joseph Capper

GENERAL AUDIENCE ABSTRACT

As a clean, abundant, and renewable source of energy with a strategic location in close proximity to global population centers, ocean wave energy shows major promise. Although much wave energy converter development has focused on large-scale power generation, there is also increasing interest in small-scale applications for powering the blue economy. There are many situations where large-scale wave energy converter (WEC) devices are not necessary or practical, but easily-portable, small-sized WECs are suitable, including navigation signs, illumination, sensors, survival kits, electronics charging, and portable desalination. In this thesis, the objective was to optimize the performance of small-sized, oscillating body wave energy converters. Oscillating body WECs function by converting a device's wave-driven oscillating motion into useful power. Two types of oscillating body WECs were studied: bottom hinged and two-body attenuator. For the bottom-hinged device, the goal was to show the feasibility of a WEC and desalination system using numerical modeling to estimate the system performance. Based on the model results, the system will produce desirable amounts of fresh water with suitably low concentration and be effective at discharging brine. The objective for the two-body attenuator was to develop a method of power maximization through resonance tuning and numerical simulation. Based on the two- and three-degree-of-freedom model results with approximate drag coefficients, the elliptical cross section had the largest power absorption out of three different geometries of body cross sections. A mooring stiffness study with the three-degree-of-freedom model showed that mooring stiffness can be increased to increase power absorption.

Acknowledgements

I would like to express my gratitude to my adviser, Prof. Lei Zuo, for his guidance throughout my Masters studies and research. I would like to thank my committee members, Prof. Rui Qiao and Prof. Shihong Lin, for their support.

I would like to thank the US Department of Energy (DOE) for partial financial support from the Waves to Water competition prizes and the US Environmental Protection Agency (EPA) for partial financial support under Grant No. EPA 83991001-0.

I would like to thank all my lab colleagues at the Center for Energy Harvesting Materials and Systems for creating an atmosphere of collaboration. A special thanks to Dr. Qiaofeng Li and Jia Mi for their help towards my research and analytical work.

I would also like to thank my parents and siblings for their love and support throughout my education.

I would like to express my condolences to all those who have lost friends and family during the COVID-19 pandemic.

Table of Contents

1. Introduction	1
1.1 Seawater Desalination.....	1
1.2 Ocean Wave Energy	2
1.3 Methods for Ocean Wave Energy Conversion	3
1.4 Motivation and Objectives.....	8
1.5 Organization.....	8
2. Theoretical Background	9
2.1 Desalination	9
2.1.1 Overview of Desalination Technologies.....	9
2.1.2 Reverse Osmosis for Wave-Powered Desalination	13
2.2 Ocean Waves	15
2.2.1 Standard Coordinate System.....	15
2.2.2 Regular Waves.....	16
2.2.3 Irregular Waves.....	18
2.2.4 Hydrodynamics	19
2.2.5 Wave Body Interaction	22
2.3 BEM Solvers.....	24
2.4 WEC Sim	25
3. Analysis of an Oscillating Surge Wave Energy Converter and Desalination System.....	27
3.1 Design Overall Concept and Working Principle	27
3.2 Mechanical Design.....	28
3.3 System Dynamics and RO Supporting Equations	32
3.4.1 Methodology	34
3.4.2 Results and Discussion	38
3.5 Preliminary Experiment Validation	46
3.6 Summary	46
4. Analysis of a Portable Two-Body Attenuator Wave Energy Converter	48
4.1 Design Overall Concept and Working Principle	48
4.2 System Governing Equations.....	49
4.3 Frequency Domain Natural Frequency Tuning	50
4.4 Time Domain Power Absorption Simulation	52
4.5 Results and Discussion	55
4.6 Summary	61

5. Conclusions and Future Work.....	63
References.....	65
Appendices.....	71
Appendix A: W3 Optimization Study Results.....	71
Appendix B: Combined System Pressure and Permeate Flow Rate Plots, Irregular Wave	73
Appendix C: Full Simulation Results, Irregular Wave (w/ ACC and PRV)	77

List of Figures

Figure 1.1 Global Physical and Economic Water Scarcity [3]	1
Figure 1.2 Desalination Plant Use by Region [4]	1
Figure 1.3 Wave Energy Potential in the US [10]	2
Figure 1.4 Wave Energy Technology classified according to working principle [18].....	4
Figure 1.5 Generic scheme of a bottom-fixed Oscillating Water Column (OWC) energy converter [20].....	5
Figure 1.6 OWC breakwater at Sakata Port in Japan [21].....	5
Figure 1.7 Heaving (point absorber) devices [18]	6
Figure 1.8 Pitching Devices.....	7
Figure 1.9 Overtopping Devices [30]	8
Figure 2.1: Osmosis vs. reverse osmosis [42].....	9
Figure 2.2: RO desalination basic layout [43]	10
Figure 2.3: Spiral-wound membrane illustration [45]	10
Figure 2.4 (a) Single-stage RO; (b) Two-stage RO; (c) Two-stage RO with concentrate recycling [47].....	11
Figure 2.5. Schematic diagram of electrodialysis (ED) where A is the anion exchange membrane and C is the cation exchange membrane [49]	12
Figure 2.6. Schematic of CDI during (a) adsorption and (b) desorption [48]	12
Figure 2.7. Schematic of multi-stage flash (MSF) [53]	13
Figure 2.8. Schematic of multi-effect distillation (MED) with 3 effects [53]	13
Figure 2.9. Single effect mechanical vapor compression process (MVC) with spray evaporation [52]	13
Figure 2.10. Comparison of desalination technologies across a variety of desalination performance metrics [54].....	14
Figure 2.11. (a) SEC_w vs. Δg_w and (b) TEE vs. Δg_w for the major desalination processes [37] ..	15
Figure 2.12. Standard coordinate system for a floating body [57]	16
Figure 2.13. Regular wave model diagram [59]	16
Figure 2.14. WEC-Sim Workflow Diagram [57]	26
Figure 3.1 Overall System Diagram	27
Figure 3.2. Double-acting piston pump working principle.....	28
Figure 3.3. Bladder-type accumulator working principle [69]	28
Figure 3.4. Foldable flap design	29
Figure 3.5. Bottom frame design layout	30
Figure 3.6. Prototype for future wave tank testing	30

Figure 3.7. Flap-pump connection critical components.....	31
Figure 3.8. FEA analysis for critical components.....	32
Figure 3.9. Motion diagram for oscillating surge WEC	32
Figure 3.10. RO membrane flow schematic [46].....	34
Figure 3.11. Brine osmotic pressure as a function of recovery [46].....	34
Figure 3.12. Ansys AQWA Model	35
Figure 3.13(a). Wave energy converter Simulink model.....	35
Figure 3.13(b). Piston & RO Simulink block	36
Figure 3.13(c). Piston pump Simulink block	36
Figure 3.13(d). RO membrane Simulink block	36
Figure 3.14. Recovery vs. Needle Valve (NV) Opening Height for different membrane areas (MA)	40
Figure 3.15. Average Permeate Concentration vs. Needle Valve (NV) Opening Height for different membrane areas (MA).....	40
Figure 3.16. 5-Day Permeate Volume vs. Needle Valve (NV) Opening Height for different membrane areas (MA)	40
Figure 3.17(a). System Pressure vs. Time Combined Plots, W6 irregular wave.....	43
Figure 3.17(b). Permeate Flow Rate vs. Time Combined Plots, W6 irregular wave	43
Figure 3.18. Wave profile, system pressure, permeate flow rate, and permeate concentration for the six sea states	45
Figure 3.19. Preliminary integrated test.....	46
Figure 4.1. Concept diagram for the two-body attenuator.....	48
Figure 4.2. System assembly for deployment.....	48
Figure 4.3. Motion schematic of the attenuator WEC: (a) 2DOF (b) 3DOF	49
Figure 4.4. Desired main body overall dimension constraints.....	51
Figure 4.5. Two-body attenuator with thin tuning plate	52
Figure 4.6. Body cross sections used for analysis	52
Figure 4.7. Simulink model of the 2DOF system	53
Figure 4.8. Simulink model of the 3DOF system	54
Figure 4.9. 2DOF power results, rectangular cross section	56
Figure 4.10. 2DOF power results, elliptical cross section	56
Figure 4.11. 2DOF power results, quadrilateral cross section.....	57
Figure 4.12. Rotational velocity, rectangular cross section, 80 Nsm/rad damping, 0.5 Cd, regular wave	57
Figure 4.13. Rotational velocity, rectangular cross section 1000 Nsm/rad damping, 0.5 Cd, regular wave.....	57

Figure 4.14. 2DOF power results comparison with approximate drag coefficients	58
Figure 4.15. 3DOF drag study power results, rectangular cross section	59
Figure 4.16. 3DOF drag study power results, elliptical cross section	59
Figure 4.17. 3DOF drag study power results, quadrilateral cross section	60
Figure 4.18. 3DOF drag study results comparison with approximate drag coefficients	60
Figure 4.19. 3DOF mooring stiffness study results	61
Figure B1(a). System Pressure vs. Time Combined Plots, W1 irregular wave	73
Figure B1(b) Permeate Flow Rate vs. Time Combined Plots, W1 irregular wave.....	73
Figure B2(a). System Pressure vs. Time Combined Plots, W2 irregular wave	73
Figure B2(b) Permeate Flow Rate vs. Time Combined Plots, W2 irregular wave.....	73
Figure B3(a). System Pressure vs. Time Combined Plots, W3 irregular wave	74
Figure B3(b) Permeate Flow Rate vs. Time Combined Plots, W3 irregular wave.....	74
Figure B4(a). System Pressure vs. Time Combined Plots, W4 irregular wave	74
Figure B4(b) Permeate Flow Rate vs. Time Combined Plots, W4 irregular wave.....	75
Figure B5(a). System Pressure vs. Time Combined Plots, W5 irregular wave	75
Figure B5(b) Permeate Flow Rate vs. Time Combined Plots, W5 irregular wave.....	75
Figure B6(a). System Pressure vs. Time Combined Plots, W6 irregular wave	76
Figure B6(b) Permeate Flow Rate vs. Time Combined Plots, W6 irregular wave.....	76
Figure C1. Full Simulation Results, W1 Irregular Wave (w/ ACC and PRV)	77
Figure C2. Full Simulation Results, W2 Irregular Wave (w/ ACC and PRV)	77
Figure C3. Full Simulation Results, W3 Irregular Wave (w/ ACC and PRV)	78
Figure C4. Full Simulation Results, W4 Irregular Wave (w/ ACC and PRV)	78
Figure C5. Full Simulation Results, W5 Irregular Wave (w/ ACC and PRV)	79
Figure C6. Full Simulation Results, W6 Irregular Wave (w/ ACC and PRV)	79

List of Tables

Table 1.1 Wave Energy Converters Installations (kW) around the World (2016) [14]	3
Table 2.1. Wavelengths and Disturbing Forces of the Main Ocean Wave Types [55]	15
Table 2.2. Available BEM Solvers and their Characteristics [64].....	24
Table 3.1. Critical Component FEA Results	31
Table 3.2. Wave Conditions (5-Day Test Period) [34][73]	37
Table 3.3. DOW FILMTECTM SW30-2521 Membrane Properties.....	37
Table 3.4. Performance Estimation Simulations.....	38
Table 3.5. W3 Optimization Study: Average Recovery	39
Table 3.6. W3 Optimization Study: Average Permeate Concentration (ppm)	39
Table 3.7. W3 Optimization Study: 5-Day Permeate Volume (L)	39
Table 3.8. Tuned NV Opening Heights	41
Table 3.9. Performance Estimation: Regular Wave (w/ ACC and PRV)	41
Table 3.10: Performance Estimation: Irregular Wave (No ACC or PRV)	42
Table 3.11. Performance Estimation: Irregular Wave (w/ ACC Only)	42
Table 3.12. Performance Estimation: Irregular Wave (w/ PRV Only).....	42
Table 3.13. Performance Estimation: Irregular Wave (w/ ACC and PRV).....	42
Table 3.14. Permeate and Brine Production Results (Irregular wave w/ ACC and PRV).....	44
Table 4.1. Sample of Geometry Variation Parameters and Natural Frequency Results, Baseline Shape.....	51
Table 4.2. Tuned Natural Frequency for Each Shape.....	52
Table 4.3. 2DOF Regular Wave Power Results Summary	55
Table 4.4. 2DOF Irregular Wave Power Results Summary.....	56
Table 4.5. 3DOF Drag Study Regular Wave Power Results Summary (k _m =k _h).....	58
Table 4.6. 3DOF Drag Study Irregular Wave Power Results Summary (k _m =k _h)	59
Table 4.7. 3DOF Mooring Stiffness Study Results (Regular Wave).....	61
Table A1: W3 Optimization Study Average System Pressure (Pa).....	71
Table A2. W3 Optimization Study: Average Permeate Flow Rate (m ³ /s).....	71
Table A3. W3 Optimization Study: Average Permeate Concentration (ppm)	71
Table A4. W3 Optimization Study: Average Recovery	71
Table A5. W3 Optimization Study: 5-Day Permeate Volume (L)	72

1. Introduction

1.1 Seawater Desalination

Freshwater scarcity is on the rise. In the past century, global water use has been growing at over twice the rate of population increase, causing over 2 billion people today to live in countries experiencing high water stress. By 2030, about 700 million people worldwide could be displaced by intense water scarcity [1]. Even though water covers 70% of the earth's surface, only 3% of the world's water is freshwater. Of that 3%, two thirds are frozen in glaciers or very difficult to access, leaving only 1% of the world's total water as freshwater that is readily available for human use [2]. Figure 1.1 shows water scarcity's impact around the world.

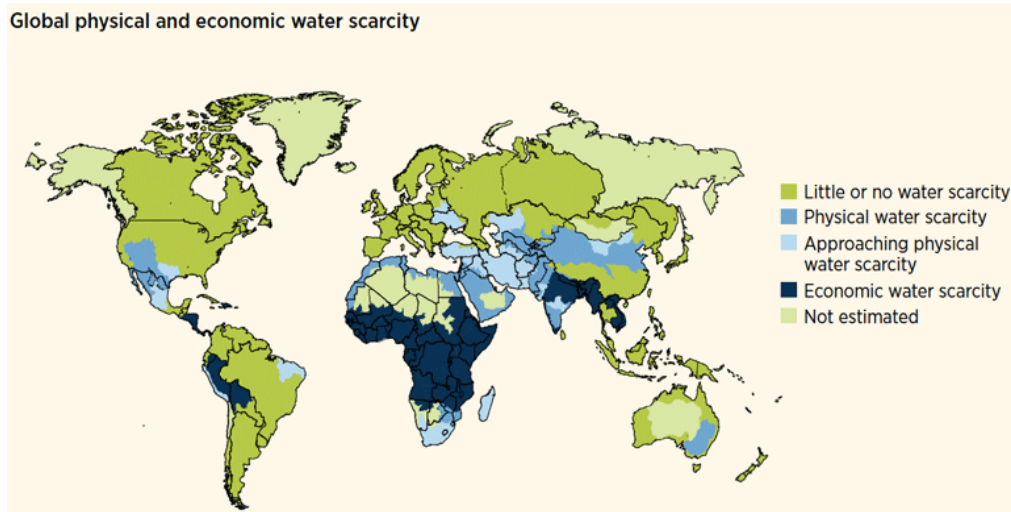


Figure 1.1 Global Physical and Economic Water Scarcity [3]

With growing freshwater scarcity, saltwater desalination plants are increasingly popular as an alternative method for freshwater production. Today, there are over 21,000 desalination plants being operated in more than 120 countries throughout the world, producing over 3.5 billion gallons of potable water per day [4]. Figure 1.2 compares desalination plant use by regions of the world. The largest seawater desalination plant in the Americas is located in Carlsbad, CA and can produce 50 million gallons of freshwater each day [4].

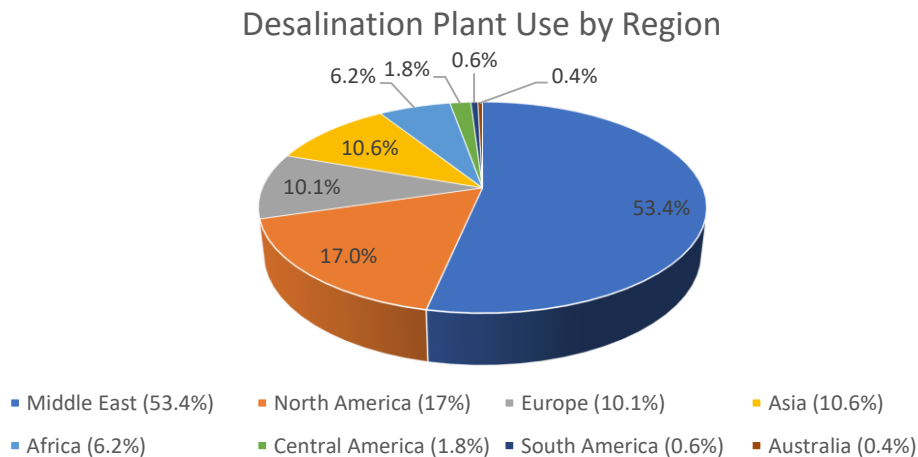


Figure 1.2 Desalination Plant Use by Region [4]

One major challenge associated with desalination plants is providing electricity to power the plants. To desalinate seawater with typical average salt concentration, the theoretical minimum amount of energy required for osmosis is about 1 kWh/m³ of seawater (3.8 kWh/kgal) [5]. In reality, with current desalination technology capabilities, the energy required is 2.5-3.5 kWh/m³ (10-13 kWh/kgal) [5]. At this level of energy consumption, the Carlsbad, CA plant would require 500-650 Mwh of energy to produce 50 million gallons of freshwater in one day. A standard coal-fired power plant produces 500 Mw of electricity, or 12,000 Mwh each day, and can power 118,000 homes [6]. Therefore, the Carlsbad plant alone could consume over half of a standard power plant's electricity output.

Typically, desalination plants use electricity from a commercial power plant in populated areas or diesel/thermal power generation in remote areas [7]. Both approaches have major downsides, such as difficulty installing cables to reach the desalination plant, challenges transporting fuel to remote locations, and using non-renewable fossil fuels as the energy source, which can lead to pollution and climate change. In addition, deployment of the methods is time-consuming, not suitable for emergency situations where there may be an immediate need for desalinated water. Keeping in mind the limitations of existing power sources, renewable energy is being explored as an alternative.

1.2 Ocean Wave Energy

As a clean, abundant, and steady way to power desalination, ocean wave energy shows major promise. About 60% of the world's population lives in coastal regions [12], with 40% living within 20 km of the coast [13], and that number is expected to increase as city populations grow. Consequently, construction of additional desalination plants to provide water to coastal areas is expected. Ocean wave energy is a logical choice to power the plants because of the plants' close proximity to the ocean. In addition, ocean wave energy has a high average energy intensity: 4-6 kW/m² as opposed to 0.1-0.2 kW/m² for solar and 0.4-0.6 kW/m² for wind [8]. Worldwide, the usable wave energy resource has been estimated at over 2 TW, with high-potential locations including the western seaboard of Europe, the northern coast of the UK, and the Pacific coastlines of North and South America [9]. In the United States alone, the available wave energy resource is 2,640 TWh/yr, which could provide almost two thirds of the 4,000 TWh of electricity used in the US each year [11]. Figure 1.3 shows the wave energy potential in the US.

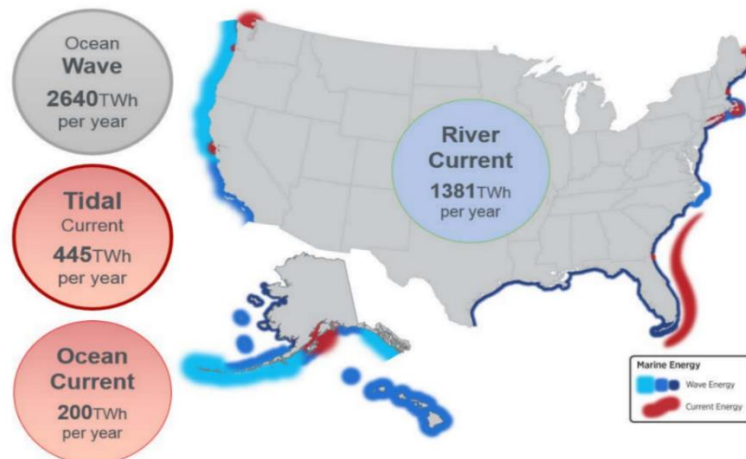


Figure 1.3 Wave Energy Potential in the US [10]

There are a number of challenges associated with wave energy conversion that have caused the technology to lag behind other renewables like wind and solar. In particular, it is difficult to integrate power from wave energy converters (WECs) into the electricity grid because of high variability in wave properties such as height, period, and direction. To make things even harder, wave resources are typically located where there are minimal grid facilities to begin with. The varying wave properties, extreme weather events, and corrosive seawater environment make it challenging to design devices that can handle such punishing conditions [14].

Nevertheless, in spite of the difficulties, wave energy converters continue to be developed around the world as governments and companies see a continuous, clean, and plentiful way to power countries and economies. By 2025, the wave energy market is expected to reach 107 million USD, with a compound annual growth rate (CAGR) of 19.3% from 2020 to 2025. Europe has the largest and fastest-growing wave-energy market, with North America and the Asia Pacific at second and third [15]. In recent years, Europe has been the leader in operational WEC projects: 296 kW in Spain, 400 kW in Portugal, and 3200 kW in Sweden as of 2016 [14]. Table 1.1 compares the power produced by WEC installations worldwide. In the past two decades, one noteworthy accomplishment in WEC installation is the Pelamis design, a full-scale prototype that generated electricity for the UK national grid in 2004 and operated at the first pre-commercial array from 2008 to 2009. Besides the Pelamis, in 2014 several offshore WECs including the Aquamarine Power Oyster and Wave Dragon were deployed at test centers and in the past few years there were several small-scale (<100 kW) WEC sea trials in the US [16].

Table 1.1 Wave Energy Converters Installations (kW) around the World (2016) [14]

Country	Planned	Installed	Operational	Total
Canada	0	0	11	11
New Zealand	0	20	0	20
Denmark	39	12	1	52
Italy	0	150	0	150
Mexico	200	0	0	200
Ghana	0	0	450	450
Spain	0	230	296	526
Korea	0	0	665	665
China	0	400	300	700
Portugal	350	0	400	750
United States	1335	500	30	1865
Sweden	0	0	3200	3200
Ireland	5000	0	0	5000

1.3 Methods for Ocean Wave Energy Conversion

Ocean wave energy converters have been under development for centuries, with the first patent for an ocean wave energy converter filed by a Frenchman named Pierre-Simon Girard in 1799. In Japan, Yoshio Masuda began studying wave energy conversion in the 1940s and developed a navigation buoy powered by wave energy. Masuda is often considered the father of modern WEC technology [17]. Today, there is tremendous diversity in the different types of WEC's, with no convergence on a widely used design as in the case of wind energy. The three

main categories are oscillating water column, oscillating bodies, and overtopping devices, as shown in Figure 1.4 [18].

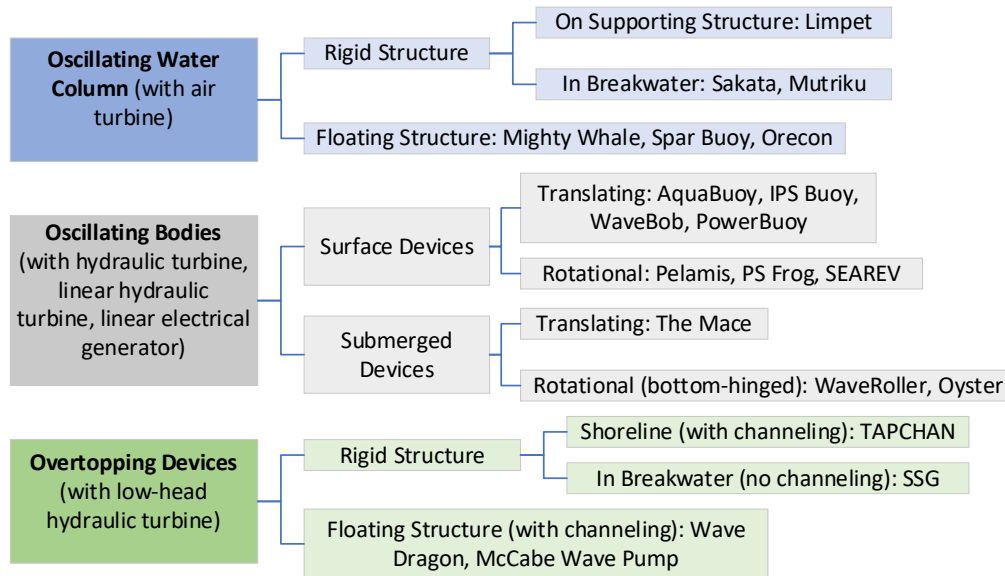


Figure 1.4 Wave Energy Technology classified according to working principle [18]

In oscillating water column devices (OWCs), a fixed or oscillating hollow structure is open to the sea below the water surface and traps air above the inner free surface. The trapped air is alternately compressed and decompressed by the wave action, forcing the air to flow through a turbine coupled to a generator to produce electricity [19]. Figure 1.5 shows a general diagram of the oscillating water column concept. Because of the reciprocation of the air flow, OWCs typically require a self-rectifying turbine or a complex system of non-return valves to rectify the flow so it can pass through a conventional turbine. OWCs are one of the oldest and most collectively developed classes of wave energy converters, both as floating offshore systems for powering devices such as navigation buoys and as shore-mounted power plants for providing electricity to the grid. There have been several real-scale OWC systems constructed and tested over the years, including the 500 kW Toftestallen plant in Norway, the 100 kW Sakata Caisson Breakwater in Japan, the 400 kW Pico plant in Portugal, and the 500 kW LIMPET device in Scotland [20]. Figure 1.6 shows the Sakata Breakwater, which began power generation in the winter of 1989 [22].

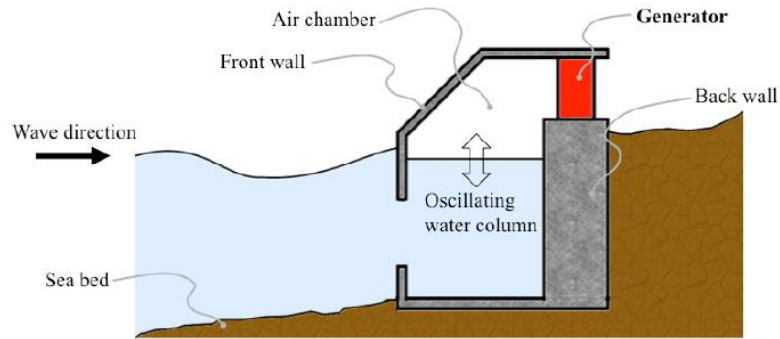


Figure 1.5 Generic scheme of a bottom-fixed Oscillating Water Column (OWC) energy converter [20]

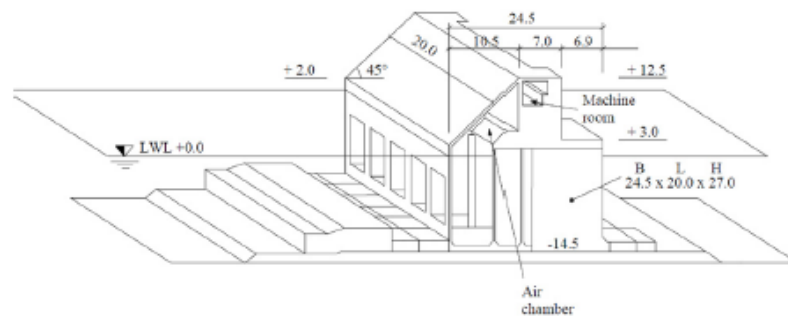


Figure 1.6 OWC breakwater at Sakata Port in Japan [21]

Oscillating body WECs use a power takeoff (PTO) system to convert a device's oscillating motion into useful power. Typically, the PTO is either a hydraulic system or electric generator [23]. There are many different styles of oscillating body WECs under development, generally falling into two classes: heaving or pitching. Heaving devices, also known as point absorbers, contain bodies that float on the surface of the waves. The PTO is activated as the ocean waves cause movement perpendicular to the sea bed [18]. More specifically, point absorbers can usually be classified as single-body or two-body systems. Figure 1.7 illustrates the difference between single-body and two-body point absorbers. A single-body point absorber consists of a floating buoy attached to a fixed reference that is typically attached to the seafloor. A PTO is placed between the buoy and the fixed reference. As the buoy oscillates, it drives the PTO to generate power. For a two-body point absorber, a submerged body is added beneath the floating buoy and the PTO is usually placed between the two bodies. This eliminates the long PTO connection distance between the seabed and water surface as in the case of the single-body

point absorber. Other benefits of the two-body point absorber include increased captured power due to the larger relative motion with two bodies and improved stability from increased radiation and viscous damping caused by the submerged body [25]. Recent examples of point absorber WECs include the 150 kW PB150 PowerBuoy by Ocean Power Technologies and a one-half scale 600 kW device by Wavestar, in addition to the examples shown in Figure 1.7 [26].

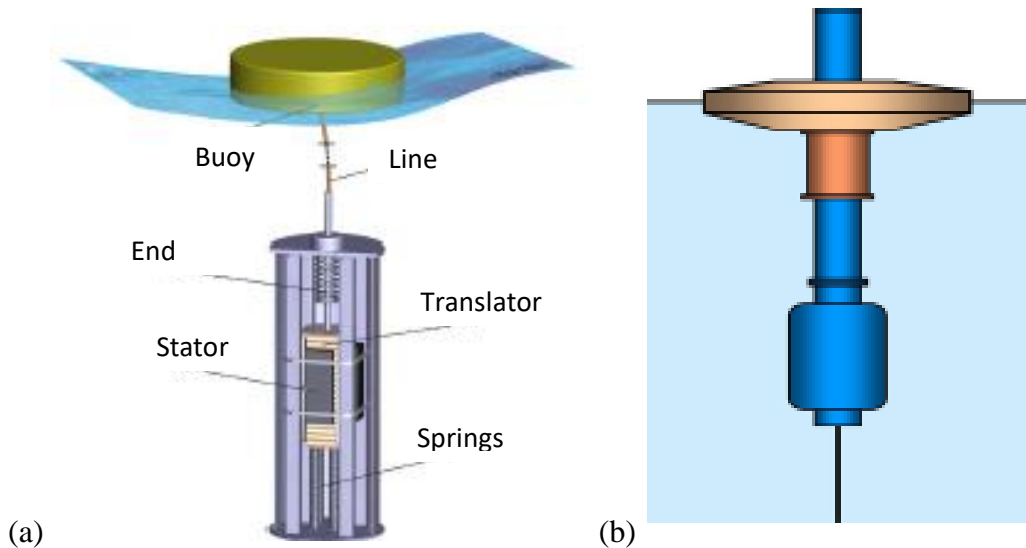


Figure 1.7 Heaving (point absorber) devices [18]

- (a) Single-body heaving buoy: Swedish heaving buoy with linear generator
- (b) Two-body heaving buoy: deep draught-spar device

Unlike the translational motion of heaving devices, pitching devices use the relative rotation between two or more bodies to produce power [18]. Pitching devices are typically classified as either floating—also known as attenuators—or bottom-hinged. Figure 1.8 shows the difference between attenuators and bottom-hinged pitching devices. Attenuators consist of a series of sections linked by flexible hinged joints that allow the sections to rotate relative to each other. The device is placed in parallel with the wave direction and oscillates with the amplitude of the wave while being moored to the seafloor [27]. Typically, attenuators use a hydraulic PTO attached between the sections that is driven linearly as the joints rotate [18]. Examples of attenuators include the McCabe Wave Pump, 750-1000 kW Pelamis, 500-6000 kW Wave Star, 375 kW Salter Duck, and 1000 kW Anaconda [28]. With bottom-hinged WECs, a device resembling a plate is pivoted on a rotation axis attached to the seafloor. Bottom-hinged WECs are deployed in near shore water with depths up to 20 m and can be fully submerged or surface-piercing. There are a variety of PTO styles under development for bottom-hinged WECs including hydraulic pistons and electrical generators [29]. Some examples of bottom-hinged WECs include the 100 kW WaveRoller and the 250-1000 kW BioWave [28][29].

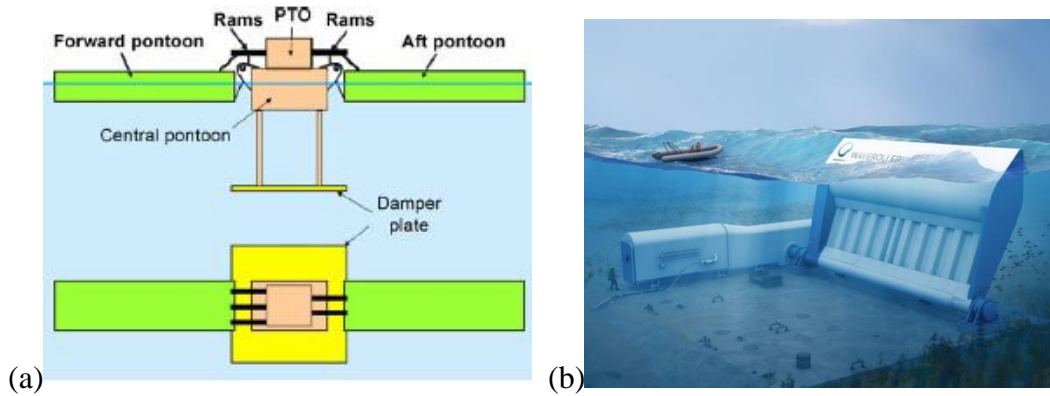
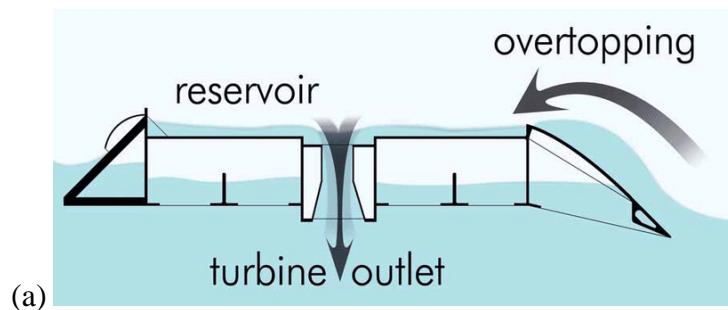


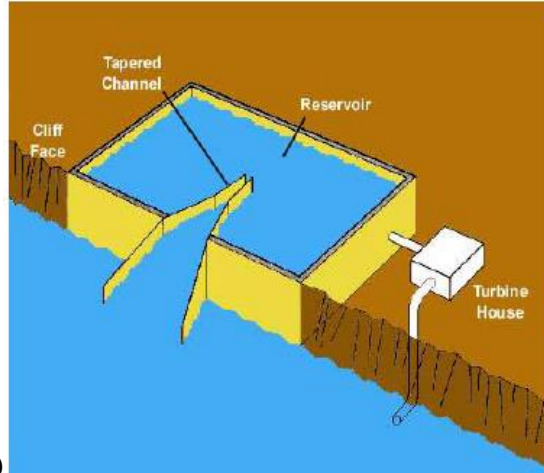
Figure 1.8 Pitching Devices

(a) Floating (attenuator): McCabe Wave Pump [18]

(b) Bottom-hinged: WaveRoller [24]

Overtopping devices generate power by capturing sea water from incident waves above sea level and releasing the water back to the ocean through turbines. They can be classified as either floating devices that are moored offshore or coastal devices that are permanent structures attached to the shore, as shown in Figure 1.9. Because overtopping devices are not dependent on correctly tuning the device to resonate with the waves, the device can be constructed to be very large [30]. Another advantage is that very unstable wave energy can be converted to relatively stable static energy. Also, overtopping devices typically convert the water flow to electricity using low head axial turbines, which is a mature technique in hydroelectric engineering, making power generation design easier [31]. However, there are still challenges with overtopping devices, especially with floating and stabilizing offshore structures to optimize power output [30]. Overtopping device examples include the 350 kW TAPCHAN, 40 kW Wave Dragon, and 150 kW Sea-wave Slot-cone Generator (SSG) [28].





(b)

Figure 1.9 Overtopping Devices [30]

(a) Offshore floating: Wave Dragon flow schematic

(b) Coastal: TAPCHAN schematic

1.4 Motivation and Objectives

While much of the wave energy converter development has focused on large-scale power generation, there is also increasing interest in small-scale applications. Many types of low-energy marine devices could potentially be powered by ocean wave energy, including navigation signs, illumination, sensors, survival kits, and electronics charging [32][33]. The Powering the Blue Economy report by the US Department of Energy (DOE) highlights the importance of small-scale ocean wave energy [33]. Through design competitions, the DOE has actively sponsored the development of small-sized wave energy devices. The Waves to Water competition, for instance, focuses on wave-powered desalination and the Ocean Observing competition focuses on wave-powered devices for ocean condition monitoring [34][35].

The objective of this thesis is to examine and optimize the performance of small-sized, oscillating body wave energy converters. Two main types of oscillating body WECs were investigated: bottom-hinged and attenuator. For the bottom-hinged device, the goal was to demonstrate the feasibility of an oscillating surge wave energy converter and desalination system by using numerical modeling to estimate the system performance. The system was designed to address needs outlined in the US DOE Waves to Water competition, which seeks to grow the development of wave-powered desalination systems that are small and modular and can provide potable drinking water in disaster response situations and to remote coastal locations [34]. For the attenuator, the goal was to use resonance tuning and numerical simulation to develop a method of power maximization. The attenuator dimensional constraints were selected with small size and portability in mind.

1.5 Organization

Chapter 2 presents some theoretical background on desalination, ocean wave energy, and software used for numerical modeling of wave energy converters. Chapter 3 describes the methodology and results for the performance estimation of the oscillating surge wave energy converter and desalination system through numerical modeling. Chapter 4 presents the methodology and results from the power maximization study for the two-body attenuator. Chapter 5 gives the conclusions and some ideas for future work.

2. Theoretical Background

2.1 Desalination

2.1.1 Overview of Desalination Technologies

Desalination can be defined as “the thermodynamic process of separating fresh water from water that contains dissolved salts” [36]. No matter how desalination is accomplished, there is always a minimum amount of chemical energy required to accomplish the separation. In addition to separation energy, the desalination system as a whole introduces additional energy consumption with every added inefficiency present in the system [36]. Generally, present-day desalination technologies fall into three main categories: pressure-driven, electric field-driven, and thermally driven [37].

In the case of pressure-driven desalination, pressure exerted on one side of a semipermeable membrane separates the solution into permeate and retentate (also called brine or concentrate). The permeate is the purified water while the brine is a concentrated solution that must be disposed of or treated [38]. Separation efficiency for pressure-driven desalination processes is expressed as the rejection of a given compound, as shown in Equation 2-1, where c_p is the permeate concentration and c_f is the feed concentration. The rejection ranges from 0 for complete permeation to 1 (100%) for complete rejection. For industrial applications, rejection ranges from 10-50%, but is typically around 20% [38].

$$\text{Rejection} = 1 - c_p/c_f \quad (2-1)$$

Osmosis is a natural process in which a lower concentration saline solution tends to flow through a membrane to a higher concentration saline solution. The flow occurs until the system reaches equilibrium [39]. The osmotic pressure is the amount of pressure that must be applied to the high concentration solution side to stop fluid movement during osmosis [40]. Osmotic pressure depends on the solution concentration. Typically, seawater osmotic pressure is 30-40 bar (435-580 psi) [39]. Reverse osmosis (RO) uses an applied pressure to force water from a higher concentration solution through a membrane to a lower concentration saline solution, removing salt and other particles [39]. Figure 2.1 illustrates the difference between osmosis and reverse osmosis. Reverse osmosis is a common pressure-driven desalination process and uses a membrane with a pore size typically from 0.001-0.0001 microns [41].

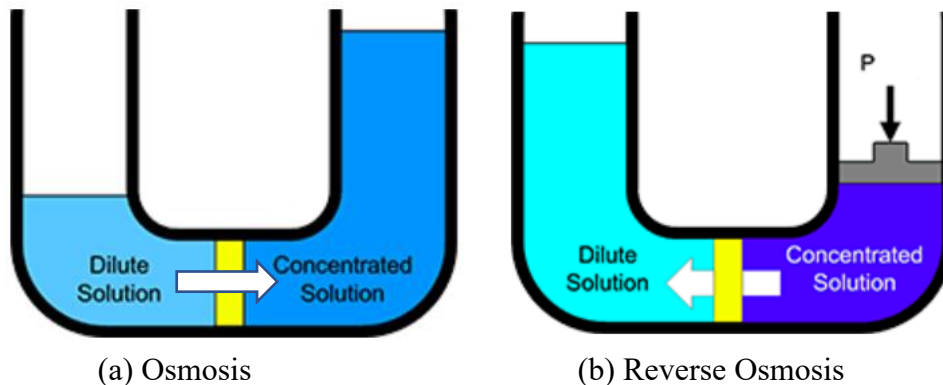


Figure 2.1: Osmosis vs. reverse osmosis [42]

Figure 2.2 shows the basic layout for a reverse osmosis desalination process. Incoming feed water typically undergoes pretreatment to remove suspended solids. A high-pressure pump is used to reach the pressure necessary to achieve reverse osmosis and produce permeate [43].

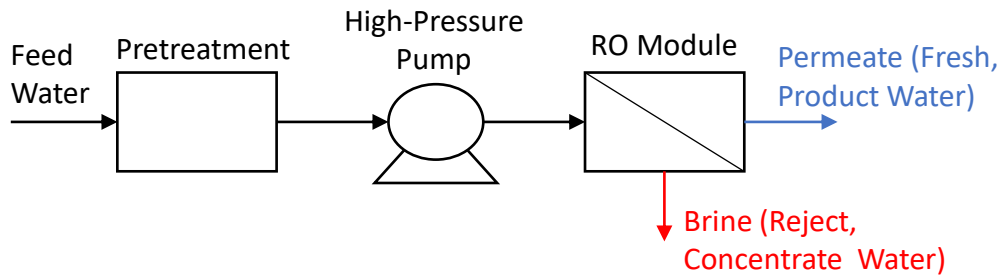


Figure 2.2: RO desalination basic layout [43]

A typical reverse osmosis module is spiral-wound, containing sheets of membrane and mesh spacer wrapped around a center permeate tube, as shown in Figure 2.3. The spacers create flow channels for the incoming feed water while the permeate tube collects the desalinated water generated from the membrane layer [44].

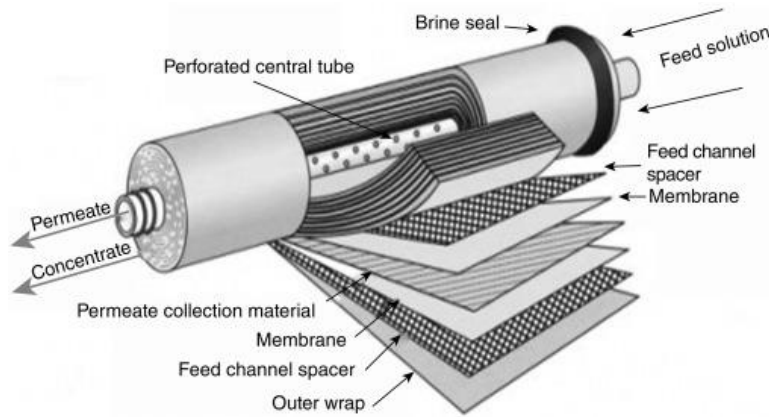
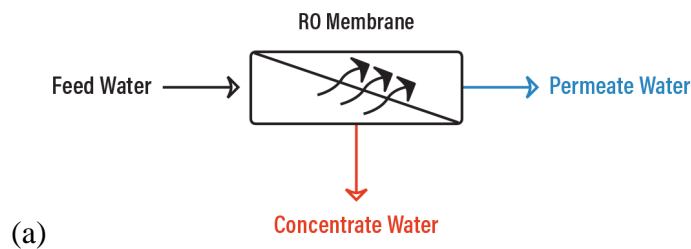


Figure 2.3: Spiral-wound membrane illustration [45]

Multiple RO modules can be connected in various configurations to boost permeate production. Figure 2.4 illustrates how multiple stages can be added to an RO system, with the concentrate from one stage feeding into the RO module of the next stage. Concentrate can also be fed back into the initial feedwater stream to further increase the efficiency [46].



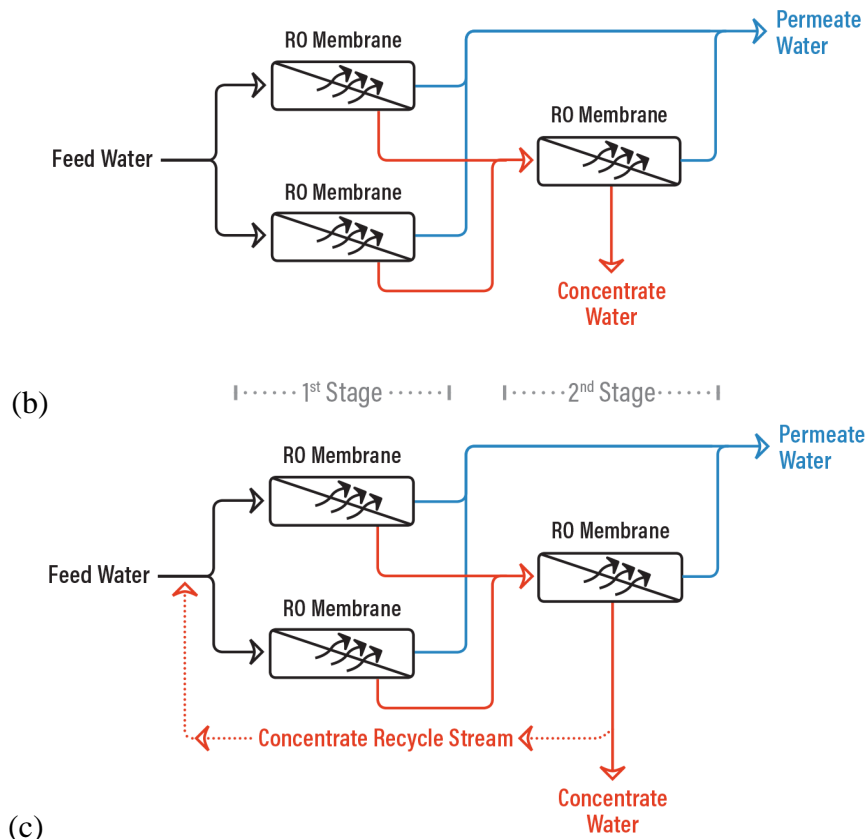


Figure 2.4 (a) Single-stage RO; (b) Two-stage RO; (c) Two-stage RO with concentrate recycling [47]

In electric field-driven desalination, a voltage is applied to the system to temporarily create an electric field that drives the desalination process. The two main types of electric field-driven desalination are electrodialysis (ED) and capacitive deionization (CDI), as shown in Figures 2.5 and 2.6. For ED, electric potential is the driving force to extract charged compound from a saline solution. As ions migrate through anion and cation-exchange membranes, concentrate is generated in one compartment as ions are retained in opposite membranes and fresh water is generated in a different compartment as like ions migrate through the appropriate membranes. In CDI, a feed solution is passed through oppositely charged electrodes polarized by voltage, creating an electric field in the medium. Consequently, an interface is created between the electrodes and an electrolyte in which solvated ions are adsorbed. During the adsorption phase, fresh water exits the system as the salt ions are removed. During the desorption phase, to release the adsorbed ions and discharge brine, the electric field is cut off at zero voltage [48].

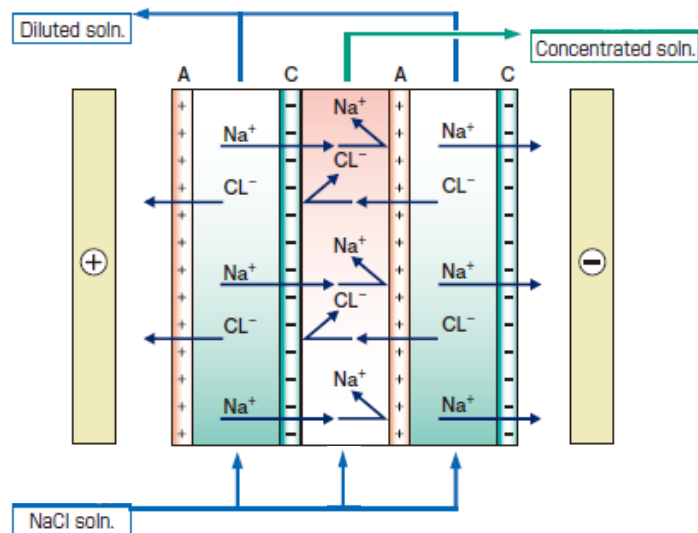


Figure 2.5. Schematic diagram of electrodialysis (ED) where A is the anion exchange membrane and C is the cation exchange membrane [49]

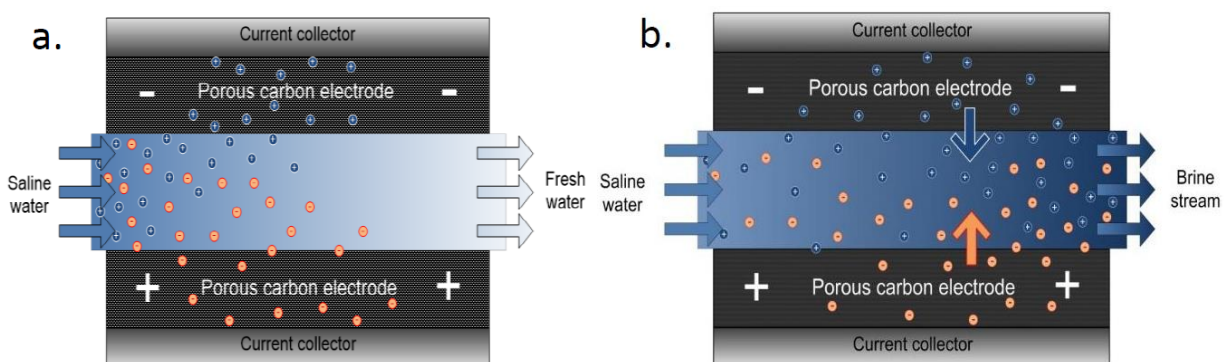


Figure 2.6. Schematic of CDI during (a) adsorption and (b) desorption [48]

Thermal desalination involves changing liquid saltwater into vapor. The vapor, which is generally free from the salt and other contaminants that were in the saltwater, is condensed to form high-purity distilled water [50]. The main types of thermal desalination include multi-stage flash (MSF), multi-effect distillation (MED), and mechanical vapor compression (MVC). In the case of MSF, fluid is heated at a certain pressure and flashed at a lower pressure to form vapor. The vapor is collected and condensed through several stages to create purified water, as shown in Figure 2.7. In MED, inlet saltwater is boiled in a series of evaporation effects. First, heat from a source such as waste heat or a solar collector is used to vaporize the saltwater. The vapor then passes to the next effect, where it loses latent heat to evaporate liquid saltwater that is fed into the next effect, and so on, as shown in Figure 2.8. MVC uses a compressor to pressurize and heat water vapor and then condenses the vapor into distillate using a heat exchanger with the incoming saltwater. The saltwater is preheated as it enters the system by the exiting pure water and brine streams. Figure 2.9 shows an outline of the MVC process [52].

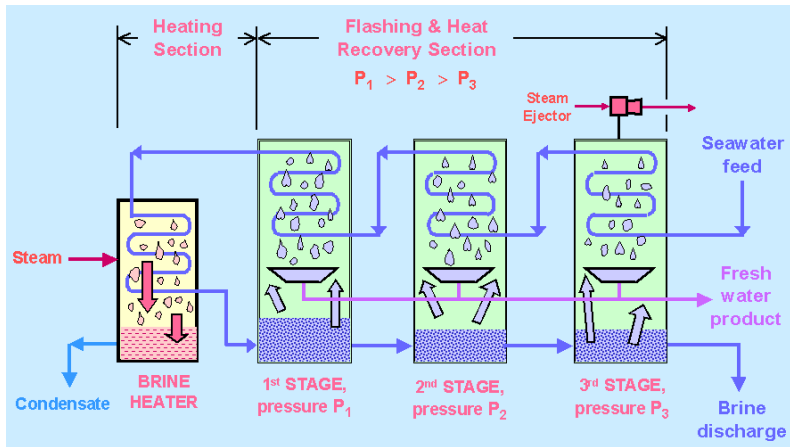


Figure 2.7. Schematic of multi-stage flash (MSF) [53]

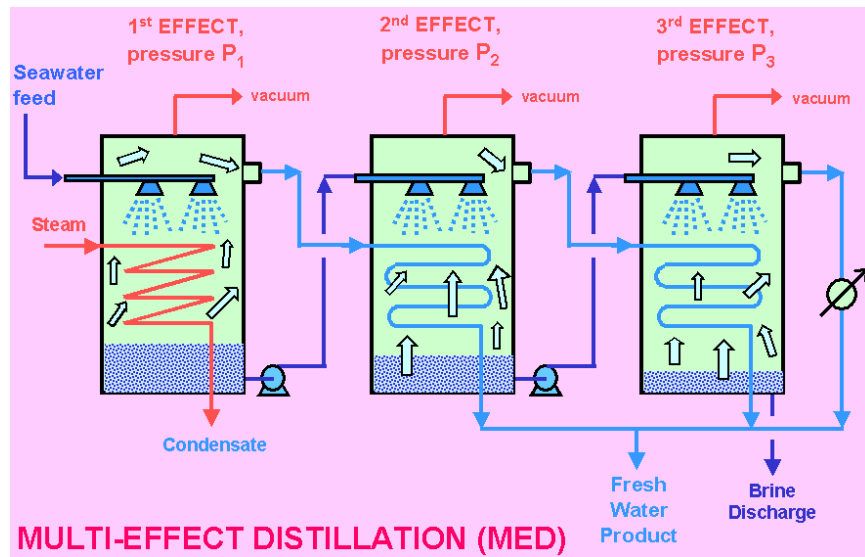


Figure 2.8. Schematic of multi-effect distillation (MED) with 3 effects [53]

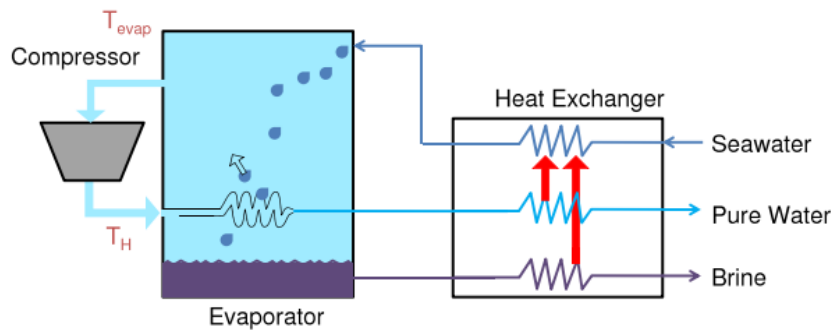


Figure 2.9. Single effect mechanical vapor compression process (MVC) with spray evaporation [52]

2.1.2 Reverse Osmosis for Wave-Powered Desalination

Looking at the various types of desalination technology presented in section 2.1.1, reverse osmosis (RO) is one of the top types of desalination technology for use with wave energy

converters. It can achieve over 99.4% rejection, able to reduce the approximately 35000 mg/L total dissolved solids (TDS) in seawater down to 100-400 mg/L TDS. In comparison with other technologies such as multiple-effect distillation (MED), multi-stage flash distillation (MSF), and mechanical vapor compression (MVC), RO is a high-scoring option, as shown in Figure 2.10 [54]. Reverse osmosis also has high thermodynamic energy efficiency when compared to other processes, as shown in Figure 2.11 [37]. Because it performs particularly well in small-scale operation and has a high thermodynamic efficiency, RO is well-suited for wave-powered desalination. The high energy density of ocean wave energy makes it a good match for overcoming the osmotic pressure to drive reverse osmosis. RO was selected as the desalination process for the design presented in this thesis.






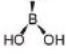


Metric		MD	RO	MED	MSF	MVC
Energy Efficiency		☆☆☆	★★★★	★★★☆☆	★★★☆☆	★★★☆☆
High-Salinity Feedwaters		★★★★	★★☆☆	★★★★	★★★★	★★★★
Small-Scale Operation		★★★★	★★★★	★★★☆☆	★★★☆☆	★★★☆☆
Utilizing Low-Grade Energy		★★★★	★★☆☆	★★★★	★★★☆☆	★★☆☆
Fouling Resistance		☆☆☆☆	☆☆☆☆	☆☆☆☆	★★★★	★★★★
Rejection of Non-Volatile Neutral Solutes		★★★★	★★☆☆	★★★★	★★★★	★★★★
Low Pretreatment		☆☆☆☆	☆☆☆☆	★★★★	★★★★	★★★★
Low Lifetime Costs		☆☆☆☆	★★★★	★★★★	★★★☆☆	★★☆☆

Figure 2.10. Comparison of desalination technologies across a variety of desalination performance metrics [54]

The thermodynamic energy efficiency, TEE , can be used to quantify the energy efficiency of any desalination process. Figure 2.11 compares the TEE for different desalination processes, showing that RO has very high TEE . Also known as second-law efficiency or exergy efficiency, TEE is quantitatively defined as the ratio of Gibbs free energy Δg to specific energy consumption SEC . The SEC can be calculated as the water-specific energy consumption SEC_w , the energy consumed to generate a unit volume of deionized water. The water-specific Gibbs free energy Δg_w is the ideal separation energy required per volume of product water. The TEE can be calculated according to Equation 2-2 [37].

$$TEE = \frac{\Delta g_w}{SEC_w} \tag{2-2}$$

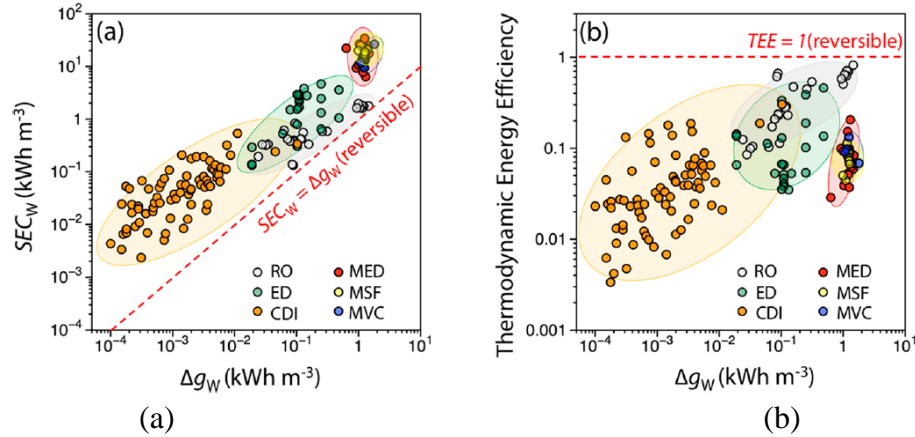


Figure 2.11. (a) SEC_w vs. Δg_w and (b) TEE vs. Δg_w for the major desalination processes [37]

2.2 Ocean Waves

Ocean waves are usually classified into four main types: wind waves, seiches, seismic sea waves (tsunamis), and tides. Table 2.1 lists the four main wave types, the typical wavelength, and the disturbing force that causes each type of wave [55]. In wave energy conversion, wind waves are the main wave type of interest, and that is the wave type that will be explored in this thesis.

Table 2.1. Wavelengths and Disturbing Forces of the Main Ocean Wave Types [55]

Wave Type	Typical Wavelength	Disturbing Force
Wind Wave	60-150 m (200-500 ft)	Wind over ocean
Seiche	Large, variable; a function of basin size	Change in atmospheric pressure, storm surge, tsunami
Seismic sea wave (tsunami)	200 km (125 mi)	Faulting of seafloor, volcanic eruption, landslide
Tide	$\frac{1}{2}$ circumference of Earth	Gravitational attraction, rotation of Earth

2.2.1 Standard Coordinate System

Typically, for a body floating in water, there are six standard degrees of freedom (DOFs). The translational DOFs are (1) surge (x), (2) sway (y), (3) heave (z) and the rotational DOF's are (4) roll (RX), (5) pitch (RY), and (6) yaw (RZ). The positive x-axis defines a wave angle heading of zero and the positive z-axis is in the vertical upwards direction. Figure 2.12 illustrates the standard coordinate system for a floating body [56][57].

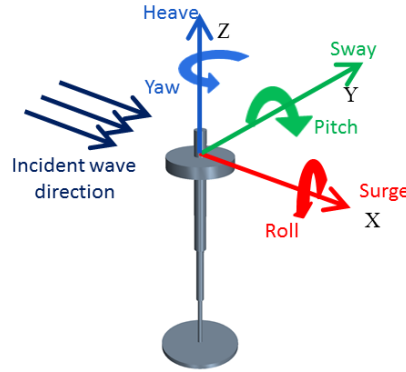


Figure 2.12. Standard coordinate system for a floating body [57]

2.2.2 Regular Waves

In reality, wind ocean waves are a composition of numerous waves with different frequencies and directions. Interaction between the many component waves causes irregular variation in wave height, period, and other properties, making mathematical modeling challenging. A regular wave is a simplified, sinusoidal approximation of ocean waves used for modeling purposes [58]. Figure 2.13 shows a standard layout of a regular wave model.

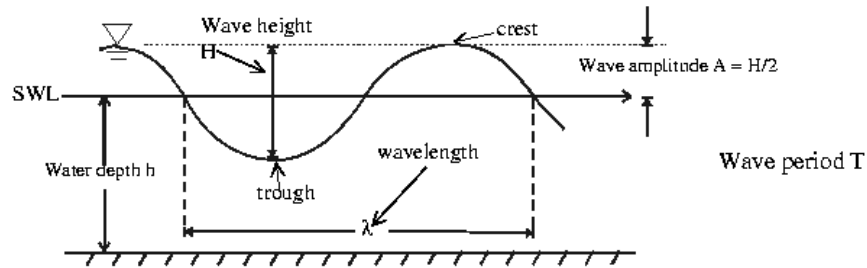


Figure 2.13. Regular wave model diagram [59]

The linear wave, or Airy wave, is a regular wave model considered to be the simplest model of an ocean wave. It assumes homogenous, incompressible, inviscid fluid, and irrotational flow. In addition, it assumes that wave amplitude is small compared to wavelength and water depth, allowing the linear free surface condition to be used. For fixed reference axes, water surface elevation at position X and Y can be expressed in complex form by Equation 2-3 where a_w is the wave amplitude, ω is the wave frequency in rad/s, k is the wave number, χ is the wave propagation direction, and α is the wave phase [58].

$$\zeta = a_w e^{i[-\omega t + k(X \cos \chi + Y \sin \chi) + \alpha]} \quad (2-3)$$

For finite water depth, the velocity potential at location $\vec{X} = (X, Y, Z)$ is given by Equation 2-4 where d is the water depth and g is the gravitation acceleration [58].

$$\phi_I(\vec{X}, t) = \phi_I(\vec{X})e^{-i\omega t} = -\frac{iga_w \cosh[k(Z + d)]}{\omega \cosh(kd)} e^{i[-\omega t + k(X \cos \chi + Y \sin \chi) + \alpha]} \quad (2-4)$$

Using the linear free surface condition, the linear dispersion relationship—the relationship between wave frequency and wave number—is given by Equation 2-5 [58].

$$v = \frac{\omega^2}{g} = k \tanh(kd) \quad (2-5)$$

Wavelength and period are given by Equations 2-6 and 2-7 respectively [58].

$$\lambda = \frac{2\pi}{k} \quad (2-6)$$

$$T = \frac{2\pi}{\omega} \quad (2-7)$$

By using the Bernoulli equation and only considering the linear term, the fluid pressure can be rewritten as Equation 2-8 where ρ is the water density [58].

$$p(\vec{X}, t) = -\frac{\rho g a_w \cosh[k(Z + d)]}{\cosh(kd)} e^{i[-\omega t + k(X \cos \chi + Y \sin \chi) + \alpha]} - \rho g Z \quad (2-8)$$

Wave celerity is the velocity of wave propagation and can be written as the ratio of wavelength to period according to Equation 2-9 [58].

$$C = \frac{\lambda}{T} = \frac{gT}{2\pi} \tanh\left(\frac{2\pi d}{\lambda}\right) \quad (2-9)$$

The fluid particle velocity can be found by taking the partial derivative of the velocity potential, as shown in Equation 2-10.

$$\vec{v} = (u, v, w) = \frac{a_w \omega \cosh[k(Z + d)]}{\sinh(kd)} e^{i[-\omega t + k(X \cos \chi + Y \sin \chi) + \alpha]} (\cos \chi, \sin \chi, -i \tanh\{k[Z + d]\}) \quad (2-10)$$

The wave will become unstable and begin to break when the wave particle velocity equals the wave celerity. For any water depth, the limiting condition for wave breaking can be given by equation 2-11. For a deep-water wave, the wave breaks when the wave height $H = 2a_w$ is 1/7 of the wavelength, or in other words when $H = (1/7)\lambda$ [58].

$$\left(\frac{2a_w}{\lambda}\right)_{max} = \frac{1}{7} \tanh(kd) \quad (2-11)$$

2.2.3 Irregular Waves

In order to better approximate the non-sinusoidal properties of ocean waves, an irregular wave model uses a limited number of the dominant harmonics found in ocean waves [60]. Linear wave theory can be used to represent multi-directional sea waves (short crested waves) as the sum of a large number of wave components, as shown in Equation 2-12, where N_d and N_m are the number of wave directions and wave components along each wave direction, $\chi_m (m = 1, N_d)$, a_{jm} is the wave amplitude, ω_{jm} is the wave frequency, k_{jm} is the wave number, and α_{jm} is the random phase angle of a wave component $j_m (j = 1, N_m)$ [58].

$$\zeta(X, Y, t) = \sum_{m=1}^{N_d} \sum_{j=1}^{N_m} a_{jm} e^{i(k_{jm}X \cos \chi_m + k_{jm}Y \sin \chi_m - \omega_{jm}t + \alpha_{jm})} \quad (2-12)$$

Although the wave spectrum spreads from zero to infinite frequencies from a mathematical standpoint, in reality, wave energy is often concentrated in a relatively narrow band that determines the wave pattern. Consequently, specific starting and finishing frequencies can be selected for Equation 2-12. The starting and finishing frequencies should be selected so that the range covers at least 99% of all wave energy. For a wave spectrum $S_m(\omega)$ introduced for the m -th sub-directional waves, the wave amplitude a_{jm} can be expressed by Equation 2-13. Unidirectional (long-crested) waves only propagate along one specified direction ($N_d = 1$) [58].

$$a_{jm} = \sqrt{2S_m(\omega_j)\Delta\omega_j} \quad (2-13)$$

Other important spectral parameters include the significant wave height (Equation 2-15), mean wave period (Equation 2-16), mean zero crossing period (Equation 2-17), and peak period (Equation 2-18). The value for m_k is given by Equation 2-14 and ω_p is the peak frequency at which the maximum wave energy occurs in rad/s [58].

$$m_k = \int_0^{\infty} \omega^k S(\omega) d\omega \quad (2-14)$$

$$H_s = 4\sqrt{m_0} \quad (2-15)$$

$$T_1 = 2\pi m_0/m_1 \quad (2-16)$$

$$T_2 = 2\pi\sqrt{m_0/m_2} = T_z \quad (2-17)$$

$$T_0 = 2\pi/\omega_p \quad (2-18)$$

Irregular waves in the m -th sub-direction can be represented by wavelets with constant amplitude, as shown in Equation 2-19, where H_s^m is the significant wave height in this sub-direction and N_m is the number of wavelets [58].

$$a_{jm} = \frac{H_s^m}{\sqrt{8N_m}}, (j = 1, N_m) \quad (2-19)$$

The Pierson-Moskowitz (PM) spectrum is a commonly used type of irregular wave spectrum that assumes a fully developed, long-crested sea. It can be formulated using significant wave height and peak wave frequency. Equation 2-20 defines the spectral density for the surface elevation for the PM spectrum where f_p is the peak wave frequency and f is the wave frequency [57].

$$S_{PM}(f) = \frac{H_s^2}{4} (1.057 f_p)^4 f^{-5} \exp \left[-\frac{5}{4} \left(\frac{f_p}{f} \right)^4 \right] \quad (2-20)$$

2.2.4 Hydrodynamics

In contrast to actual ocean waves, most water wave theories assume periodic and uniform waves, with period T and height H . To develop a wave theory, approximations are used to solve a boundary value problem (BVP) containing a differential equation and boundary conditions. Two main assumptions in most water wave theories are incompressibility and continuity of flow. Incompressibility is equivalent to expressing conservation of volume, which can be stated in terms of the fluid velocities according to Equation 2-21 where u , v , and w are the three components of a fluid particle velocity in a rectangular Cartesian coordinate system [61].

$$\frac{\partial u}{\partial x} + \frac{\partial v}{\partial y} + \frac{\partial w}{\partial z} = 0 \quad (2-21)$$

In terms of the velocity vector (Equation 2-22) the continuity equation can be written as Equation 2-23. The gradient is defined by Equation 2-24. The incompressibility assumption causes the gradient of the volume to be equal to zero [61].

$$\mathbf{V} = u\mathbf{i} + v\mathbf{j} + w\mathbf{k} \quad (2-22)$$

$$\nabla \cdot \mathbf{V} = 0 \quad (2-23)$$

$$\nabla = \frac{\partial}{\partial x} \mathbf{i} + \frac{\partial}{\partial y} \mathbf{j} + \frac{\partial}{\partial z} \mathbf{k} \quad (2-24)$$

Water wave theories also assume irrotational flow. The rotation vector is given by Equation 2-25 and the three components of the rotation vector are given by Equations 2-26, 2-27, and 2-28 respectively. For irrotational flow, $\omega_1 = \omega_2 = \omega_3 = 0$ [61].

$$\boldsymbol{\omega} = \frac{1}{2} \nabla \times \mathbf{V} \quad (2-25)$$

$$\omega_1 = \frac{1}{2} \left(\frac{\partial u}{\partial z} - \frac{\partial w}{\partial x} \right) \quad (2-26)$$

$$\omega_2 = \frac{1}{2} \left(\frac{\partial v}{\partial x} - \frac{\partial u}{\partial y} \right) \quad (2-27)$$

$$\omega_3 = \frac{1}{2} \left(\frac{\partial w}{\partial y} - \frac{\partial v}{\partial z} \right) \quad (2-28)$$

Irrotational flow can be described by a velocity potential function Φ , which is related to the rectangular Cartesian velocity components by Equation 2-29 and Equation 2-30. Substitution into the continuity equation (Equation 2-21) yields the widely-used Laplace equation (Equation 2-31) [61].

$$u = \frac{\partial \Phi}{\partial x}, v = \frac{\partial \Phi}{\partial y}, w = \frac{\partial \Phi}{\partial z} \quad (2-29)$$

$$\mathbf{V} = -\nabla \Phi \quad (2-30)$$

$$\nabla^2 \Phi = \frac{\partial^2 \Phi}{\partial x^2} + \frac{\partial^2 \Phi}{\partial y^2} + \frac{\partial^2 \Phi}{\partial z^2} = 0 \quad (2-31)$$

Irrotational flow also leads to the unsteady form of the Bernoulli equation given by Equation 2-33, which is derived from the unsteady Navier Stokes equation given by Equation 2-32, where p is fluid pressure, μ is fluid viscosity, and V_f is the fluid velocity [61].

$$\rho \frac{\partial \mathbf{V}}{\partial t} + \rho (\nabla \times \mathbf{V}) \times \mathbf{V} - \mu \nabla^2 \mathbf{V} + \nabla \left(p + \rho g y + \rho \frac{V_f^2}{2} \right) = 0 \quad (2-32)$$

$$\rho \frac{\partial \Phi}{\partial t} + p + \rho g y + \frac{1}{2} \rho \left[\left(\frac{\partial \Phi}{\partial x} \right)^2 + \left(\frac{\partial \Phi}{\partial y} \right)^2 + \left(\frac{\partial \Phi}{\partial z} \right)^2 \right] = f(t) \quad (2-33)$$

For a two-dimensional case, the velocity potential differential equation can be simplified to Equation 2-34 [61].

$$\frac{\partial^2 \Phi}{\partial x^2} + \frac{\partial^2 \Phi}{\partial y^2} = 0 \quad (2-34)$$

The bottom boundary condition is given by Equation 2-35 by assuming that the ocean floor is flat and the vertical velocity component will be zero [61].

$$\frac{\partial \Phi}{\partial y} = 0 \text{ at } y = -d \quad (2-35)$$

The free surface kinematic condition is given by Equation 2-36 by assuming that a particle lying on the free surface will continue to remain on the free surface for a given instant of time [61].

$$\frac{\partial \eta}{\partial t} + \frac{\partial \Phi}{\partial x} \frac{\partial \eta}{\partial x} - \frac{\partial \Phi}{\partial y} = 0 \text{ at } y = \eta \quad (2-36)$$

The free surface dynamic condition is given by Equation 2-37 by assuming that the atmospheric pressure outside the fluid is constant [61].

$$\frac{\partial \Phi}{\partial t} + \frac{1}{2} \left[\left(\frac{\partial \Phi}{\partial x} \right)^2 + \left(\frac{\partial \Phi}{\partial y} \right)^2 \right] + g\eta = 0 \text{ at } y = \eta \quad (2-37)$$

Linear Airy Wave Theory—also known as Airy theory or sinusoidal wave theory—is one of the simplest and most useful wave theories available. It uses the small amplitude wave theory, which assumes that wave height is small compared to wavelength or water depth. This allows linearization of the free surface boundary conditions by dropping wave height terms beyond the first order and allows the free surface conditions to be satisfied at the mean water level instead of the oscillating free surface. The first-order velocity potential is given by Equation 2-38 where $k = 2\pi/\lambda$, $s = y + d$, and $\theta = k(x - ct)$. The wave profile is given by Equation 2-39 [61].

$$\Phi = \frac{gH \cosh(ks)}{2\omega \cosh(kd)} \sin\theta \quad (2-38)$$

$$\eta = \frac{H}{2} \cos\theta \quad (2-39)$$

Wave energy flux is defined as the mean power per unit crest length. For regular waves, energy flux can be found by time averaging the product of wave pressure and fluid particle velocity in the direction of wave propagation, as shown in Equation 2-40 [62].

$$J = \frac{1}{T} \int_0^T \int_{-h}^{\eta} p \frac{\partial \Phi}{\partial x} dz dt = \frac{1}{2} \rho g A^2 c_g \quad (2-40)$$

The group velocity c_g is given by Equation 2-41. The depth function $D(kh)$ is given by Equation 2-42 and can be approximated as 1 for deep water ($kh \rightarrow \infty$) and as $2kh$ for shallow water ($kh \rightarrow 0$) [62].

$$c_g = \frac{1}{2} \frac{\omega}{k} \left(1 + \frac{2kh}{\sinh(2kh)} \right) = \frac{g}{2\omega} D(kh) \quad (2-41)$$

$$D(kh) = \left[1 + \frac{2kh}{\sinh(2kh)} \right] \tanh(kh) \quad (2-42)$$

The energy flux can be rewritten as Equation 2-43 by substituting Equation 2-41 into Equation 2-40 [62].

$$J = \frac{\rho g^2 A^2 D(kh)}{4\omega} \quad (2-43)$$

Capture width CW is defined as the wave crest width completely captured and absorbed by the wave energy converter. It is the ratio of absorbed wave power P to wave energy flux J , as shown in Equation 2-44 [63].

$$CW = P/J \quad (2-44)$$

The capture width ratio CWR is a way to quantify the device hydrodynamic efficiency, dividing the capture width by a characteristic dimension L of the WEC, as given in Equation 2-45. The characteristic dimension is often the device width [63].

$$CWR = CW/L \quad (2-45)$$

2.2.5 Wave Body Interaction

For a diffracting body in regular harmonic waves, Equation 2-46 defines the velocity potential for the fluid flow field surrounding a floating body [58].

$$\phi(\vec{X}, t) = a_w \varphi(\vec{X}) e^{-i\omega t} \quad (2-46)$$

The unit amplitude of the three translational and rotational motions of the body's center of gravity are given by Equation 2-47 and 2-48 respectively. This allows the isolated space dependent term $\varphi(\vec{X})$ to be written as Equation 2-49, where φ_I is the incident wave potential, φ_d is the diffraction wave potential, and φ_{rj} is the radiation wave potential due to j -th motion with unit motion amplitude [58].

$$x_j = u_j, (j = 1, 3) \quad (2-47)$$

$$x_j = \theta_{j-3}, (j = 4, 6) \quad (2-48)$$

$$\varphi(\vec{X})e^{-i\omega t} = \left[(\varphi_1 + \varphi_d) + \sum_6^{j=1} \varphi_{rj}x_j \right] e^{-i\omega t} \quad (2-49)$$

The first order hydrodynamic pressure distribution can be calculated using the linearized Bernoulli's equation when the wave velocity potentials are known, as given by Equation 2-50 [58].

$$p^{(1)} = -\rho \frac{\partial \Phi(\vec{X}, t)}{\partial t} = i\omega\rho\varphi(\vec{X})e^{-i\omega t} \quad (2-50)$$

The unit normal vector of a hull surface can be written according to the six basic rigid body motions, as given by Equations 2-51 and 2-52. The position vector of a point on the hull surface with respect to the center of gravity in the fixed reference axes (FRA) is given by Equation 2-53 [58].

$$(n_1, n_2, n_3) = \vec{n} \quad (2-51)$$

$$(n_4, n_5, n_6) = \vec{r} \times \vec{n} \quad (2-52)$$

$$\vec{r} = \vec{X} - \vec{X}_g \quad (2-53)$$

The fluid forces can be calculated by integrating the pressure over the wetted surface of the body. Equation 2-54 gives the first order hydrodynamic force and moment components where S_0 is the mean wetted body surface. The j -th Froude Krylov force due to the incident wave is given by Equation 2-55. The j -th diffraction force due to the diffraction wave is given by Equation 2-56. The j -th radiation force due to the radiation wave from the k -th unit amplitude rigid body motion is given by Equation 2-57 [58].

$$F_j e^{-i\omega t} = - \int_{S_0} p^{(1)} n_j dS = \left[-i\omega\rho \int_{S_0} \varphi(\vec{X}) n_j dS \right] e^{-i\omega t} \quad (2-54)$$

$$F_{1j} = -i\omega\rho \int_{S_0} \varphi_1(\vec{X}) n_j dS \quad (2-55)$$

$$F_{dj} = -i\omega\rho \int_{S_0} \varphi_d(\vec{X}) n_j dS \quad (2-56)$$

$$F_{rjk} = -i\omega\rho \int_{S_0} \varphi_{rk}(\vec{X}) n_j dS \quad (2-57)$$

The fluid forces can be broken into reactive and active components. The Froude-Krylov and diffraction force make up the active or wave exciting force. The radiation force caused by radiation waves induced by body motions is the reactive force. When there is wave loading on a fixed body, then only the active wave forces are important. If a body is floating, both active and reactive forces are of interest. The radiation wave potential φ_{rk} can be expressed in real and imaginary parts and substituted into Equation 2-57 to find the added mass and damping coefficients, as shown in Equation 2-58. The added mass A_{jk} and damping B_{jk} coefficients are given by Equations 2-59 and 2-60 respectively [58].

$$\begin{aligned}
F_{rjk} &= -i\omega\rho \int_{S_0} \{Re[\varphi_{rk}(\vec{X})] + iIm[\varphi_{rk}(\vec{X})]\}n_j dS \\
&= \omega\rho \int_{S_0} Im[\varphi_{rk}(\vec{X})]n_j dS - i\omega\rho \int_{S_0} Re[\varphi_{rk}(\vec{X})]n_j dS \\
&= \omega^2 A_{jk} + i\omega B_{jk}
\end{aligned}
\tag{2-58}$$

$$A_{jk} = \frac{\rho}{\omega} \int_{S_0} Im[\varphi_{rk}(\vec{X})]n_j dS
\tag{2-59}$$

$$B_{jk} = -\rho \int_{S_0} Re[\varphi_{rk}(\vec{X})]n_j dS
\tag{2-60}$$

2.3 BEM Solvers

The boundary element method (BEM) is a numerical method that formulates systems of differential equations into boundary integral form. Green's functions are used to transform a flow problem into a source distribution problem on the body's surface. In the hydrodynamic context, BEM solves for the scatter and radiated velocity potentials that are caused by the interaction between a wave field and the body located in the field. Exciting force is determined by solving the scattering potential when the body is held fixed. Added-mass and radiation damping terms are determined by solving the potential for a moving body in the absence of incident waves. Table 2.2 compares several commonly used hydrodynamic BEM solvers. WAMIT, NEMOH, AQWA, Aquaplug, and WADAM solve in the frequency domain while ACHIL3D solves in the time domain [64]. AQWA is one of the most widely used hydrodynamics BEM solvers and was used for the studies described in this thesis.

Table 2.2. Available BEM Solvers and their Characteristics [64]

BEM Solver	Frequency Domain	Time Domain	Open Source
WAMIT	✓	X	X
NEMOH	✓	X	✓
AQWA	✓	X	X
Aquaplug	✓	X	X
ACHIL3D	X	✓	X
WADAM	X	X	X

2.4 WEC Sim

Developed in collaboration between National Renewable Energy Laboratory (NREL) and Sandia National Laboratories (Sandia), WEC-Sim (Wave Energy Converter Simulator) simulates wave energy converters using an open-source code. MATLAB/SIMULINK was used to develop the code with Simscape Multibody. WEC-sim can model devices that contain rigid bodies, joints, power take-offs, and mooring systems by solving governing equations in six degrees of freedom in the time domain. WEC-Sim must be used in combination with a BEM solver such as AQWA. The non-dimensionalized hydrodynamic coefficients are imported into WEC-Sim from a *.h5 data structure generated from the BEM output. The hydrodynamic coefficients are scaled according to Equations 2-61, 2-62, 2-63, and 2-64 where F_{exc} is the wave excitation force/torque coefficient, A is the radiation added mass coefficient, B is the radiation wave damping coefficient, and K_{hs} is the linear hydrostatic restoring coefficient [57].

$$\overline{|F_{exc}(\omega)|} = \frac{|F_{exc}(\omega)|}{\rho g} \quad (2-61)$$

$$\overline{A(\omega)} = \frac{A(\omega)}{\rho} \quad (2-62)$$

$$\overline{B(\omega)} = \frac{B(\omega)}{\rho \omega} \quad (2-63)$$

$$\overline{K_{hs}} = \frac{K_{hs}}{\rho g} \quad (2-64)$$

After scaling the hydrodynamic coefficients, WEC-sim calculates the dynamic response of the system in the time domain by solving the WEC equations of motion. For example, Equation 2-65 lists the equation of motion for a floating body about its center of gravity, where M is the mass matrix, \ddot{X} is the (translational and rotational) acceleration vector of the device, $F_{exc}(t)$ is the wave excitation force and torque vector, $F_{rad}(t)$ is the force and torque vector resulting from wave radiation, $F_{pto}(t)$ is the PTO force and torque vector, $F_v(t)$ is the damping force and torque vector, $F_{me}(t)$ is the Morison Element force and torque vector, $F_B(t)$ is the net buoyancy restoring force and torque vector, and $F_m(t)$ is the force and torque vector resulting from mooring connection. After calculating the dynamic response, the results can be post-processed using additional functions to obtain the desired results. Figure 2.14 illustrates the overall workflow for WEC-Sim [57].

$$M\ddot{X} = F_{exc}(t) + F_{rad}(t) + F_{pto}(t) + F_v(t) + F_{me}(t) + F_B(t) + F_m(t) \quad (2-65)$$

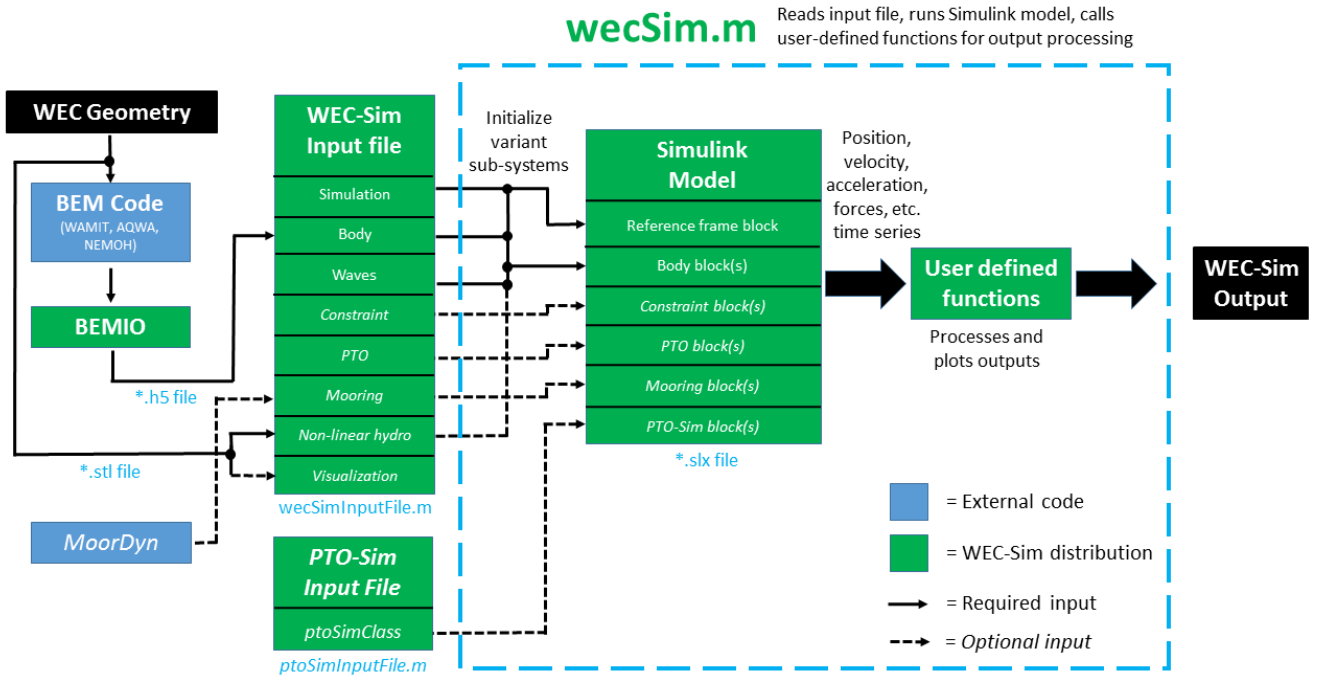


Figure 2.14. WEC-Sim Workflow Diagram [57]

3. Analysis of an Oscillating Surge Wave Energy Converter and Desalination System

3.1 Design Overall Concept and Working Principle

The objective of this chapter was to show the feasibility of an oscillating surge wave energy converter and desalination system using numerical modeling. Oscillating surge wave energy converters (OSWECs) have been studied in literature such as Ref. [29], [65], [66], and [67] and OSWECs with desalination systems have been studied in literature such as Ref. [68], but the literature has mainly focused on the large industrial scale. This study seeks to explore OSWEC desalination systems for small-scale, portable applications. The system was designed to meet requirements described in the US DOE Wave to Water competition, which was created to increase the development of small, modular, wave-powered desalination systems that can generate potable drinking water in disaster response situations and for remote coastal locations [34].

In order to capture motion from the waves, this design uses a surge-type wave energy converter with a bottom-hinged, rectangular, oscillating flap. Figure 3.1 shows the system's overall layout. The bi-directional oscillation of the flap drives a double-acting linear piston pump to force seawater to the shore where reverse osmosis is used to produce fresh water, also called permeate. The RO module reduces the concentration from saline water (35000 ppm) to fresh water. A gas-charged accumulator is used for pulsation dampening to prevent large pressure spikes, which can damage components and reduce freshwater production. A pressure relief valve is used as a safety mechanism to prevent the system pressure from reaching a level that is damaging to the RO module. A needle valve is used to control the outlet flow rate of the brine, which is high-salinity water produced as a byproduct during reverse osmosis. For stable deployment, the system can be anchored to the seafloor. Protection bumpers can be used to prevent undesirably large flap rotation and damage to the piston pump under large wave conditions.

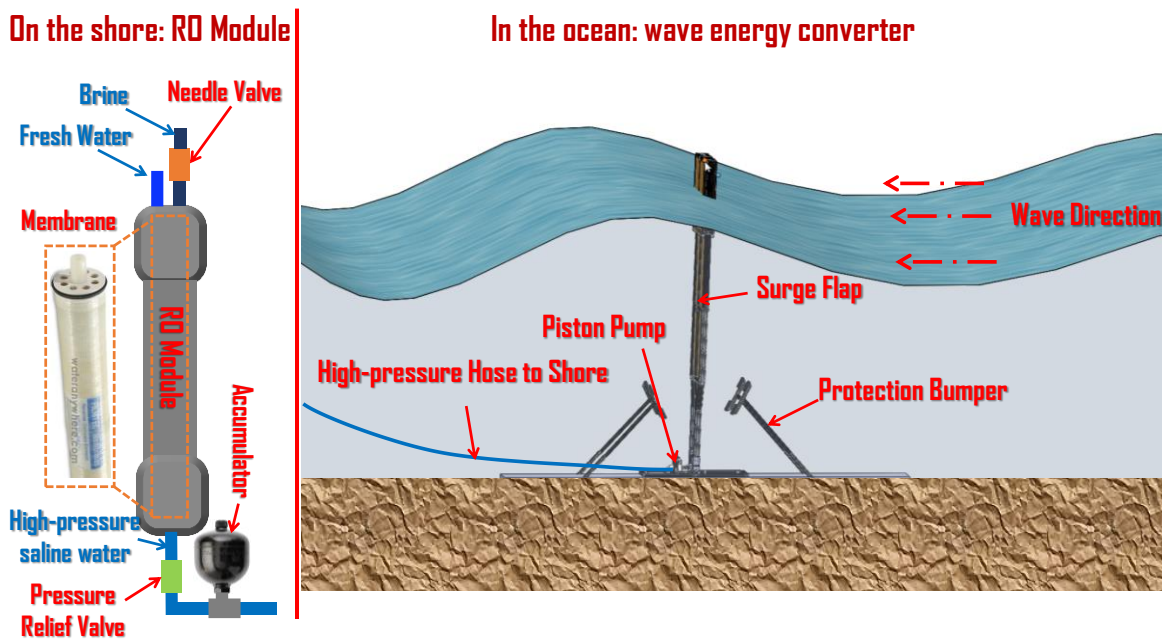


Figure 3.1 Overall System Diagram

Using a system of three check valves, seawater is pressurized by the piston pump in one direction regardless of the piston's direction of motion. Figure 3.2 shows the working principle of the linear piston pump. On the upstroke, the inlet valve and outlet valve are open while the intermediate valve is closed. Fluid is pulled in through the inlet valve while the fluid above the intermediate valve is pushed out. On the downstroke, the intermediate valve and outlet valve are open while the inlet valve is closed, forcing fluid to flow through the intermediate valve and then exit the chamber through the outlet valve.

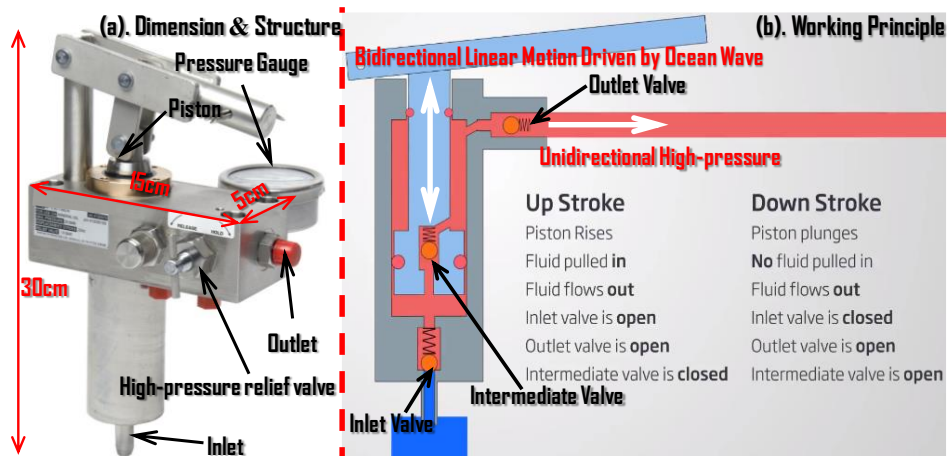


Figure 3.2. Double-acting piston pump working principle

The accumulator has a hollow chamber that houses a gas-filled bladder. During high pressure states, fluid enters the chamber and compresses the bladder, storing potential energy. When the overall system pressure drops, the bladder expands, pushing fluid out of the chamber to regulate the flow. Figure 3.3 shows a cross section of a gas-filled accumulator to illustrate the working principle.

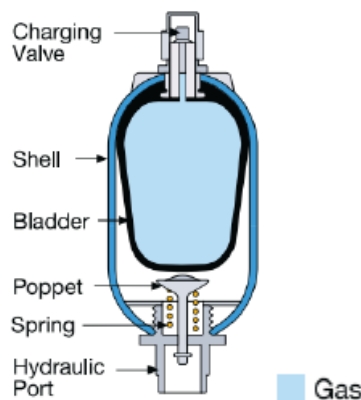


Figure 3.3. Bladder-type accumulator working principle [69]

3.2 Mechanical Design

The system was designed to fit into a standard shipping container for quick deployment in disaster relief situations. The highly portable wave energy converter incorporates a foldable flap design, as shown in Figure 3.4, which can be collapsed to 36x36x18 inches and extended to

72x144x6 inches for deployment. The flap support frame is made of extruded aluminum bar with foldable hinges and each section is filled with foam to achieve the desired buoyancy. Reinforcing brackets can be added after the system is unfolded to strengthen the connections between the flap sections.

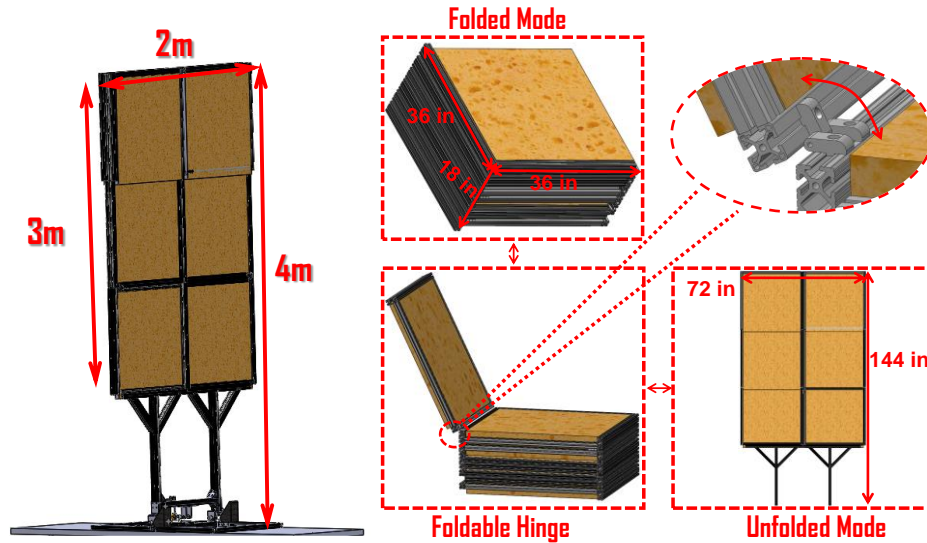


Figure 3.4. Foldable flap design

Like the flap, the bottom frame also uses extruded aluminum bar for rapid assembly and disassembly. Figure 3.5 shows the layout of the bottom frame design. The flap is attached to the base using two short shafts that ride inside plain bearings. Because of the corrosiveness of the seawater, bearings with moving metal components such as needle or ball bearings were not used. The pump is attached to the bottom frame using an adapter plate that has the pump mounting pattern and a mounting pattern to connect to the aluminum framing. Using linkages machined from aluminum plate and bar, the pump piston shaft is connected to the flap so that the flap and pump move together under the wave excitation. A cartridge intake filter can be attached to the pump inlet to prevent sand and biological sediment from entering the hydraulic system. A prototype of the wave energy converter was fabricated and assembled for future testing in a wave tank, as shown in Figure 3.6.

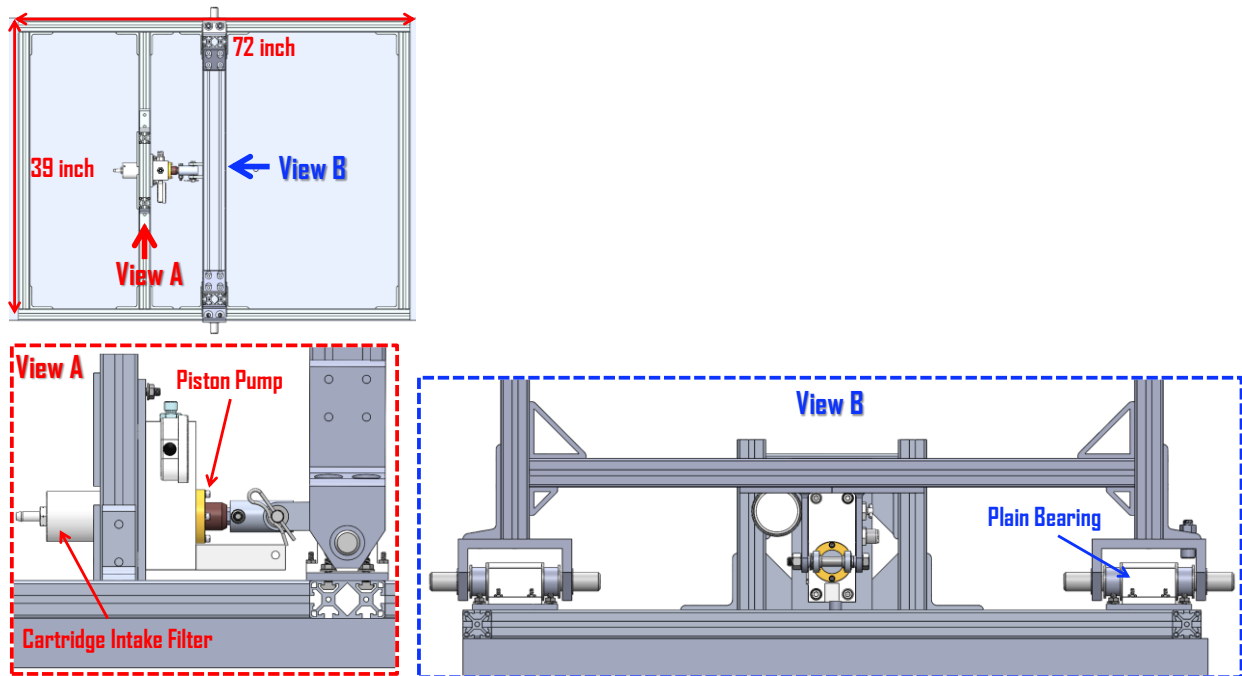


Figure 3.5. Bottom frame design layout



Figure 3.6. Prototype for future wave tank testing

Looking at stress in the design, one area of concern is the component group connecting the piston pump and oscillating flap. When pressure increases in the piston chamber, a large force will be exerted on the connecting components, as shown in Figure 3.7. This force can be approximated as a force that is equal and opposite to the force exerted by the fluid pressure on the piston. The maximum expected fluid pressure in the chamber is 65 bar (943 psi), giving a

maximum piston force of 896 lbf based on the piston area. An FEA stress analysis was performed in SolidWorks Simulation using the maximum piston force in order to correctly select materials and dimensions. Table 3.1 summarizes the results. Based on the IEC Standard for wave energy converters, the factor of safety in yield should be about 1.5-2 under different scenarios [70]. The FEA analysis results demonstrated that the Von Mises stress was below the material yield strength for each component with acceptable factors of safety. Figure 3.8 shows the FEA results for each component.

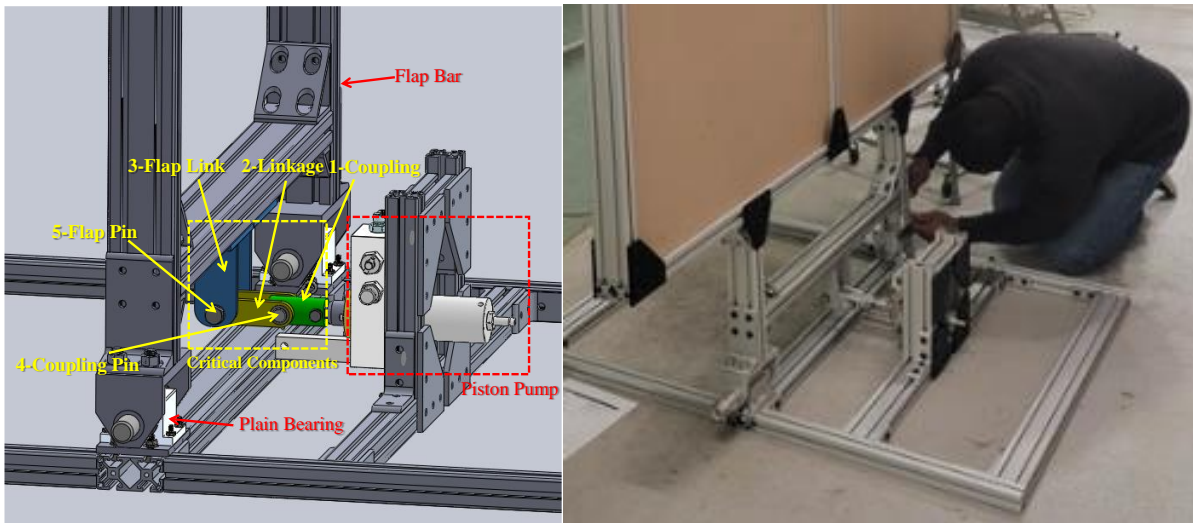


Figure 3.7. Flap-pump connection critical components

Table 3.1. Critical Component FEA Results

No.	Component Name	Material	Yield Strength (ksi)	Max Von Mises Stress (ksi)	Factor of Safety
1	Coupling	6061-T6 Aluminum	35	4.99	7
2	Linkage	6061-T6 Aluminum	35	6.83	5.1
3	Flap Link	6061-T6 Aluminum	35	14.67	2.4
4	Coupling Rotation Pin	316 Stainless Steel	40	13.13	3
5	Flap Rotation Pin	316 Stainless Steel	40	15.22	2.6

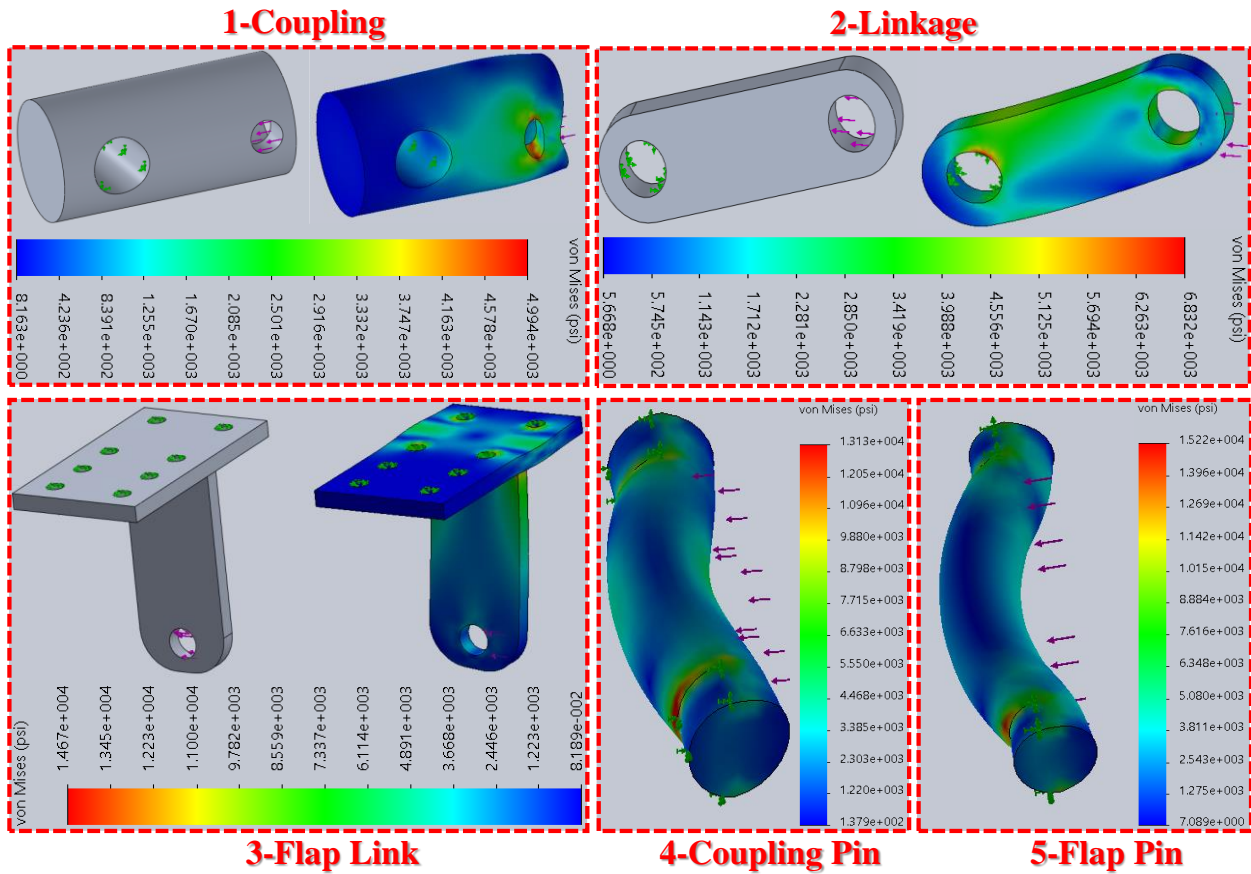


Figure 3.8. FEA analysis for critical components

3.3 System Dynamics and RO Supporting Equations

For the overall system, the equation of motion can be written as Equation 3-1 by taking the sum of the torques around the hinge point, where I is the moment of inertia of the flap, T_{ext} is the excitation torque, T_{rad} is the radiation torque, T_{pto} is PTO torque, T_{vis} is the viscous torque, T_b is the buoyant torque, θ is the angular displacement, $\dot{\theta}$ is the angular velocity, and $\ddot{\theta}$ is the angular acceleration. Figure 3.9 shows the device motion. Looking at the five terms of torque, T_{ext} and T_{rad} are frequency-independent. T_{PTO} is exerted by the PTO mechanism, which is the linear piston pump in the case of this design. T_{vis} and T_b are determined by the buoy geometry and fluid characteristics.

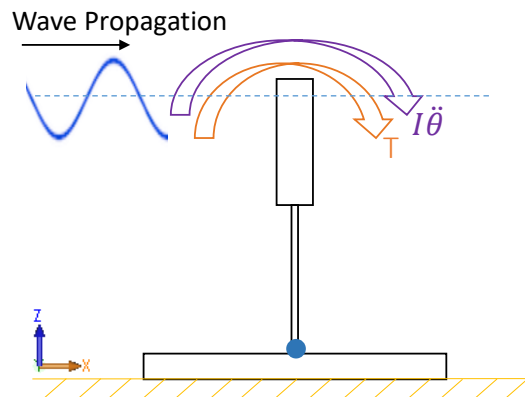


Figure 3.9. Motion diagram for oscillating surge WEC

$$I\ddot{\theta} = T_{ext} + T_{rad} + T_{PTO} + T_{vis} + T_b \quad (3-1)$$

For simplification of the numerical modeling work in the desalination portion of the WEC-Sim Simulink model, permeate production was modeled using the simplified solution-diffusion model given by Equations 3-2 and 3-3. In those equations, Q_p is the permeate flow rate, A_w is the water permeability, S is the effective area, ΔP is the incoming feed pressure, $\Delta\pi$ is the osmotic pressure difference, C_p is the permeate concentration, C_0 is the feed concentration, and B_s is the salt permeability. Typical values of $\Delta\pi$ and C_0 for seawater were used as constants for the analysis: 30 bar and 35000 ppm respectively [68].

$$Q_p = A_w S (\Delta P - \Delta\pi) \quad (3-2)$$

$$C_p = \frac{c_0}{\frac{A_w}{B_s} (\Delta P - \Delta\pi) + 1} \quad (3-3)$$

In the solution-diffusion model, the effect of concentration variation and concentration polarization are not considered. Concentration variation accounts for the salinity accumulation as clean water recovers along the membrane module and concentration polarization accounts for the salinity difference between the membrane surface and bulk stream [71]. The solution-diffusion model assumes that permeate flow Q_p is primarily dictated by the net driving pressure, which is the incoming feed pressure ΔP minus the osmotic pressure difference $\Delta\pi$ [68]. The recovery ratio, the ratio of permeate flow rate Q_p to inlet flow rate Q_0 , is given by Equation 3-4 [46].

$$R = \frac{Q_p}{Q_0} \quad (3-4)$$

When using the solution-diffusion model, it is important that the recovery is a reasonable value because solution-diffusion does not consider concentration increase along the module. Solution-diffusion assumes that the brine is always the same salinity as the seawater, but in reality, brine salinity quickly increases as recovery increases [46][72]. Consequently, solution-diffusion tends to inaccurately estimate permeate production for high recovery values, but is a reasonable model for lower recovery values. Figure 3.10 shows the flow schematic for the membrane. Taking the salt balance in the brine stream gives Equation 3-5, where C_0 is the feed salinity. The salt balance can in turn be used to derive the brine osmotic pressure as a function of recovery, as shown in Equation 3-6 [46][72]. Figure 3.11 shows the curve for brine osmotic pressure as a function of recovery. Figure 3.11 demonstrates that the brine salinity and osmotic pressure become very large for high recovery values, so the solution-diffusion model is therefore inaccurate for high recovery values. In order to avoid the inaccuracy, a target recovery value of 25% was used for the numerical model, as performed in Ref. [68].

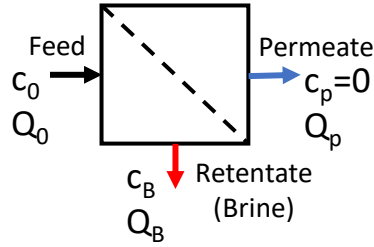


Figure 3.10. RO membrane flow schematic [46]

$$c = \frac{c_0}{1-\gamma} \quad (3-5)$$

$$\pi(\gamma) = \frac{\pi_0}{1-\gamma} \quad (3-6)$$

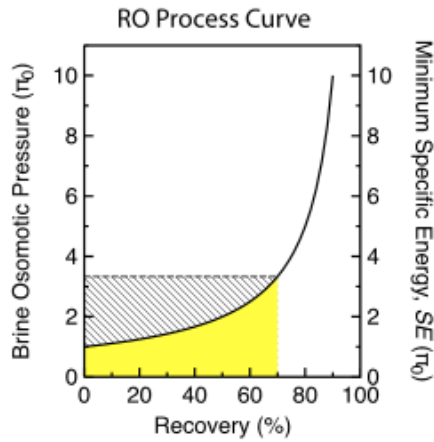


Figure 3.11. Brine osmotic pressure as a function of recovery [46]

3.4 Numerical Investigation

3.4.1 Methodology

A WEC-Sim numerical model was used to solve the WEC system dynamics together with the desalination solution-diffusion model to estimate the system's performance and freshwater production. The WEC-Sim model was developed based on desalination modeling work performed by the National Renewable Energy Lab (NREL) [68]. The BEM solver Ansys AQWA was first used in the frequency domain as shown in Figure 3.12 to obtain important hydrodynamic parameters such as the added mass, wave excitation, impulse response function, and restoring stiffness before performing the time domain solution in WEC-Sim.

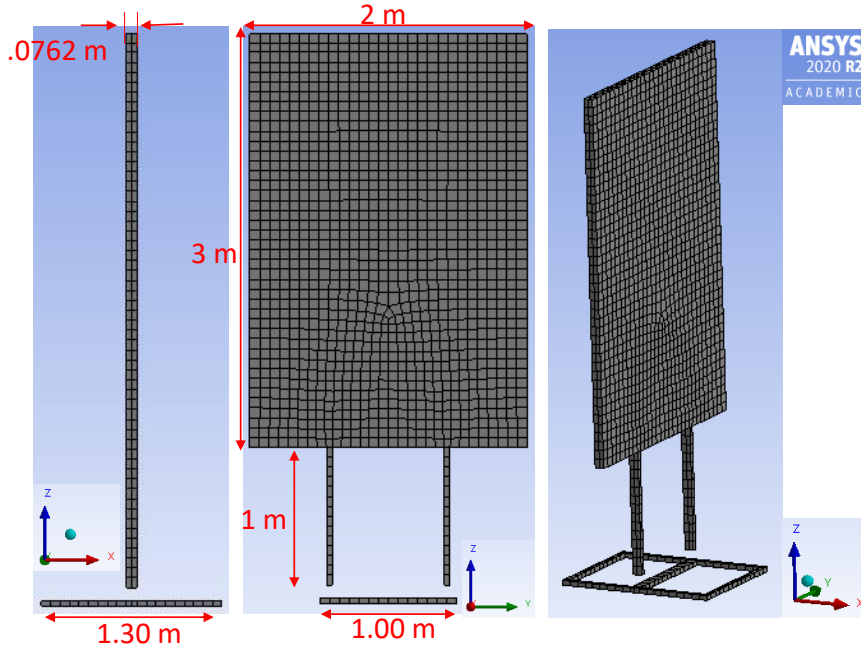


Figure 3.12. Ansys AQWA Model

In the WEC-Sim Simulink model, as shown in Figure 3.13(a), rigid body blocks were used to model the base support frame and oscillating flap while a customized translational PTO and Piston & RO block were used to model the hydraulic system, including the piston pump and RO system. A rotational joint was used to connect the flap and base support frame. The Piston & RO block shown in Figure 3.13(b) contains the RO hydraulic system, including important components such as the piston pump, gas-charged accumulator, pressure relief valve, RO membrane, and needle valve. Inside the piston pump block shown in Figure 3.13(c), a double-acting hydraulic cylinder and check valves model the unidirectional flow of water. The RO membrane block shown in Figure 3.13(d) contains a pressure relief valve to model the osmotic pressure and a linear hydraulic resistance to model the membrane's impedance to the flow.

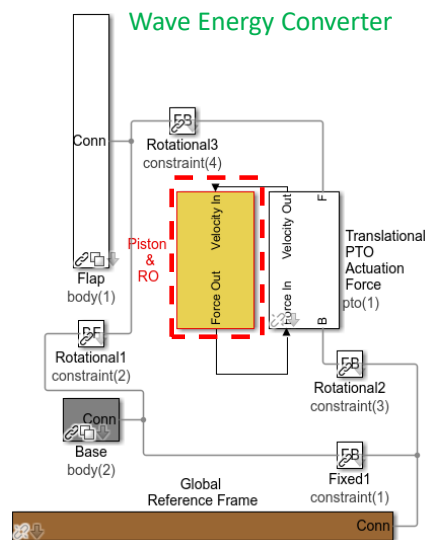


Figure 3.13(a). Wave energy converter Simulink model

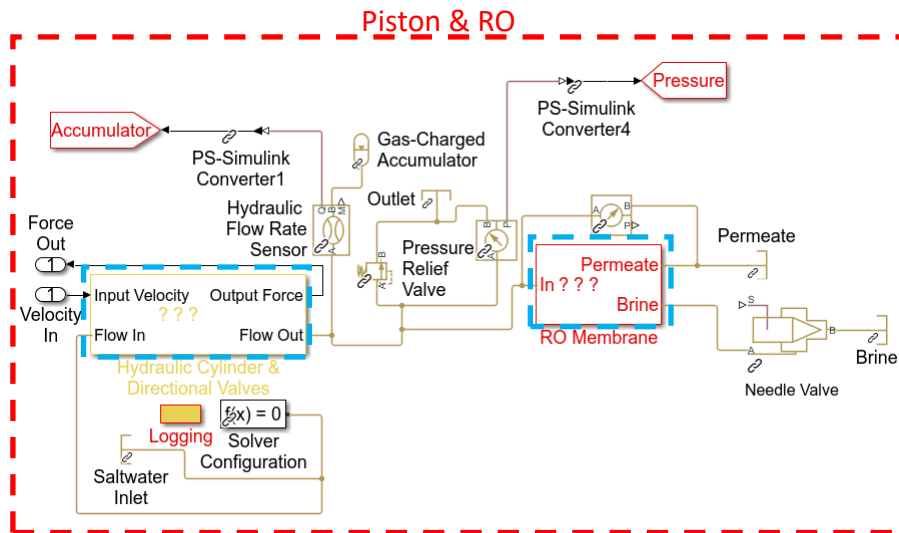


Figure 3.13(b). Piston & RO Simulink block

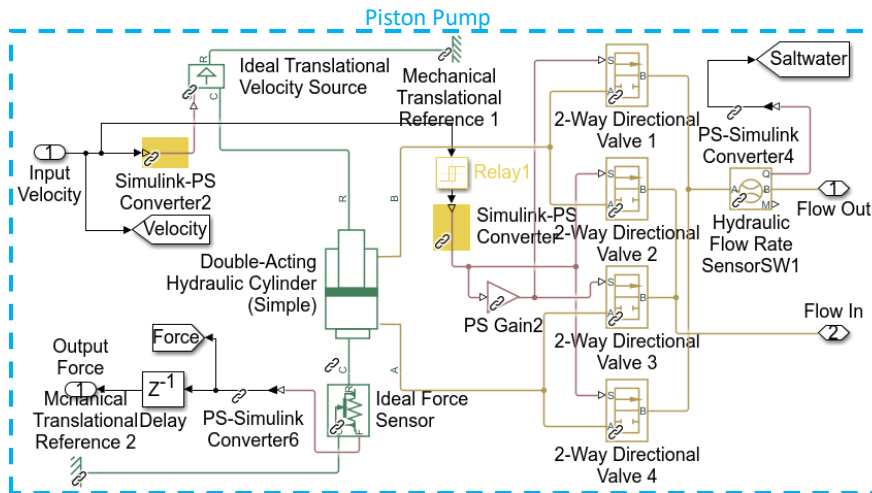


Figure 3.13(c). Piston pump Simulink block

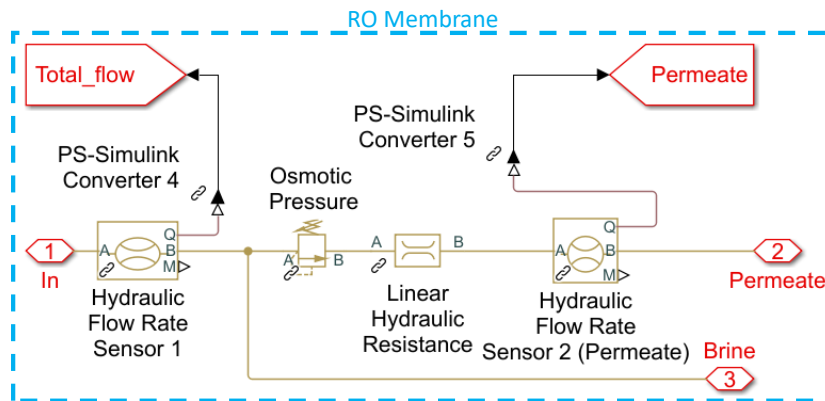


Figure 3.13(d). RO membrane Simulink block

To minimize pressure fluctuation and prevent the system pressure from dropping below the osmotic pressure, a gas-charged accumulator block was used with parameters based on a commercial product from Parker, with a fluid volume of 0.25 L and pre-charge pressure of 23.8 bar. A pressure relief valve (PRV) was included at the membrane inlet to prevent large pressure spikes and over-pressurization of the membrane. The PRV opening pressure was set at 66 bar, slightly below the membrane’s design pressure limit of 70 bar. A needle valve controlled the brine flow rate exiting the membrane. The needle valve opening height could be tuned to optimize the system performance. Using the physical piston pump commercial product, key parameters for the piston pump block were chosen, including a piston area of 0.95 in² and a stroke of 1.76 in. In the RO membrane block, the osmotic pressure was set as 30 bar based on the approximate osmotic pressure for seawater with 35000 ppm total dissolved solids (TDS). The linear hydraulic resistance was dependent on the membrane properties and was calculated according to Equation 3-7.

$$\text{Linear Hydraulic Resistance} = \frac{1}{A_w * S} \tag{3-7}$$

Each simulation was run using a 3000 s duration, 0.01 s time step, and 250 s ramp time. Average values were calculated after the simulation reached steady state. Six sea states with different wave heights and periods were used for the analysis based on real-world ocean conditions from a potential testing site at Jennette’s Pier, North Carolina, as shown in Table 3.2, for a 5-day testing period [34][73]. Irregular wave simulations were performed using a Pierson-Moskowitz spectrum.

Table 3.2. Wave Conditions (5-Day Test Period) [34][73]

Sea State	Significant Wave Height [m]	Energy Period [s]	Time for Each Wave Condition [hrs][%]
W1	0.5	6	26.4 (22%)
W2	0.5	10	6 (5%)
W3	1.0	6	33.6 (28%)
W4	1.5	7	26.4 (22%)
W5	2.0	7	26.4 (22%)
W6	3.0	7	1.2 (1%)

Baseline membrane properties were taken from a commercial RO membrane, a DOW FILMTEC™ SW30-2521, which was selected as an option for the physical system based on the system pressure and flow rate requirements. Table 3.3 lists the commercial product’s membrane properties.

Table 3.3. DOW FILMTECTM SW30-2521 Membrane Properties

Parameters	Values
$A_w (m^3/m^2/Pa/s)$	4×10^{-12}
$B_s (m/s)$	6.4×10^{-8}
$S (m^2)$	1.2

An optimization study was performed to determine the effect of adjusting the membrane area along with the needle valve opening height. The baseline membrane area was used as a starting point for the study. Initially, the membrane area and needle valve opening height were tuned under W3, the dominant sea state, with irregular wave conditions. The target maximum permeate concentration was less than 1000 ppm and the target minimum 5-day permeate volume was 400 L [34].

For sea states W1, W2, W4, W5, and W6, the needle valve opening height was tuned for each sea state using the optimized membrane area from W3 under irregular wave conditions. The reasoning was that in the physical system, the membrane area depends on the RO module selection, which is not adjustable like the needle valve opening height. Therefore, it would not be possible to adjust the membrane area for each sea state, so the best option would be to optimize the membrane area based on the dominant sea state, W3.

Using the tuned membrane area and needle valve opening height, the numerical model was run to estimate the overall system performance. The model was run using both regular and irregular waves for the six sea states. For the irregular wave simulations, the effect of the accumulator (ACC) and pressure relief valve (PRV) was explored by including and removing those components from the model. Table 3.4 summarizes the different simulations that were performed.

Table 3.4. Performance Estimation Simulations

	No ACC or PRV	w/ ACC Only	w/ PRV Only	w/ ACC and PRV
Regular Wave	None	None	None	W1, W2, W3, W4, W5, W6
Irregular Wave	W1, W2, W3, W4, W5, W6	W1, W2, W3, W4, W5, W6	W1, W2, W3, W4, W5, W6	W1, W2, W3, W4, W5, W6

3.4.2 Results and Discussion

Based on the W3 optimization study, the ideal membrane area and needle valve opening height were 0.2 m^2 and $6.0\text{e-}6 \text{ m}$ respectively. For W3, this resulted in average values of $9.81\text{e-}7 \text{ m}^3/\text{s}$ permeate flow rate, 581.62 ppm concentration, and 29% recovery. The 5-day permeate volume was 423.79 L. Tables 3.5, 3.6, and 3.7 show a section of the data for average recovery, permeate concentration, and 5-day permeate volume. Figures 3.14, 3.15, and 3.16 show a section of the curves for recovery, permeate concentration, and 5-day permeate volume. Appendix A contains the complete set of data tables from the study. Because the target recovery was 25%, only the cases with recovery in the 20-30% range were considered as possibilities for the optimal case. Although the case with $(0.1 \text{ m}^2, 5.5\text{e-}6 \text{ m})$ had lower concentration for similar recovery, the 5-day permeate volume was 389.66 L, which is less than the target minimum 5-day permeate volume of 400 L. Some larger membrane areas could achieve similar recovery values, but tended to have excessively high permeate concentration, making the case with $(0.2 \text{ m}^2, 6.0\text{e-}6 \text{ m})$ the best option. The needle valve opening heights for W1, W2, W4, W5, and W6 were tuned using the W3 optimized membrane area of 0.2 m^2 . The tuned needle valve opening heights for each sea state are shown in Table 3.8.

Table 3.5. W3 Optimization Study: Average Recovery

		NV Opening Height (m)				
		5.0E-06	5.5E-06	6.0E-06	6.5E-06	7.0E-06
Membrane Area (m ²)	0.1	0.31	0.27	0.23	0.19	0.16
	0.2	0.38	0.33	0.29	0.24	0.20
	0.3	0.41	0.36	0.31	0.27	0.22
	0.4	0.42	0.38	0.33	0.28	0.24
	0.5	0.44	0.39	0.34	0.29	0.24
	0.6	0.44	0.39	0.34	0.30	0.25

20-25% Recovery

26-30% Recovery

Table 3.6. W3 Optimization Study: Average Permeate Concentration (ppm)

		NV Opening Height (m)				
		5.0E-06	5.5E-06	6.0E-06	6.5E-06	7.0E-06
Membrane Area (m ²)	0.1	267.54	309.95	367.36	446.80	563.74
	0.2	428.28	494.58	581.62	702.14	884.86
	0.3	589.77	678.29	796.38	965.78	1249.35
	0.4	749.08	861.70	1016.22	1255.19	1617.85
	0.5	907.21	1046.93	1248.57	1690.29	2093.92
	0.6	1064.94	1236.74	1516.26	2538.39	9377.29

Table 3.7. W3 Optimization Study: 5-Day Permeate Volume (L)

		NV Opening Height (m)				
		5.0E-06	5.5E-06	6.0E-06	6.5E-06	7.0E-06
Membrane Area (m ²)	0.1	444.96	389.66	335.23	282.53	232.42
	0.2	557.28	488.16	423.79	362.02	303.26
	0.3	604.80	531.36	466.56	401.33	338.69
	0.4	630.72	561.60	492.48	425.09	360.29
	0.5	648.00	578.88	509.76	440.64	374.98
	0.6	660.96	587.52	518.40	453.60	385.78

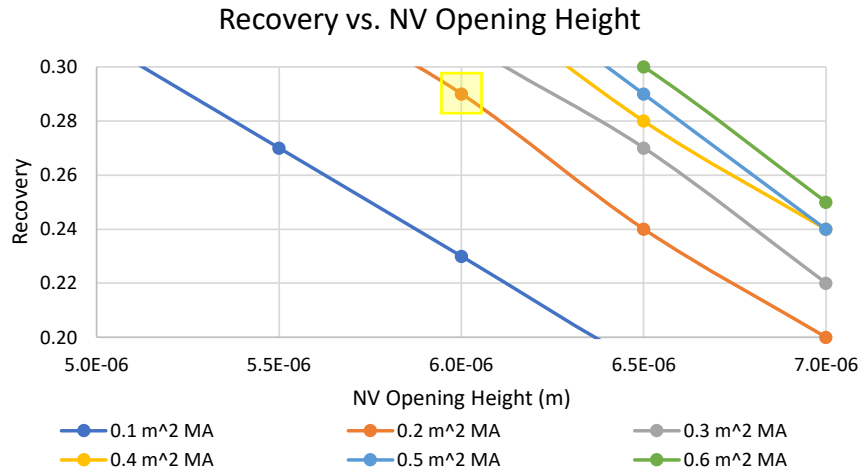


Figure 3.14. Recovery vs. Needle Valve (NV) Opening Height for different membrane areas (MA)

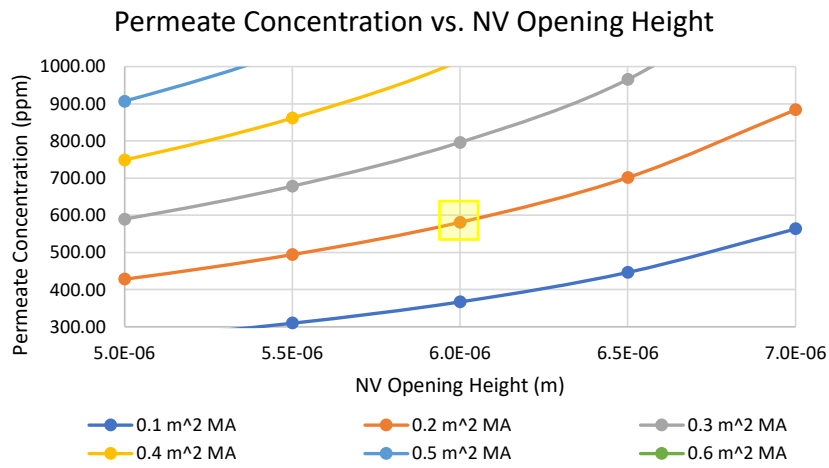


Figure 3.15. Average Permeate Concentration vs. Needle Valve (NV) Opening Height for different membrane areas (MA)

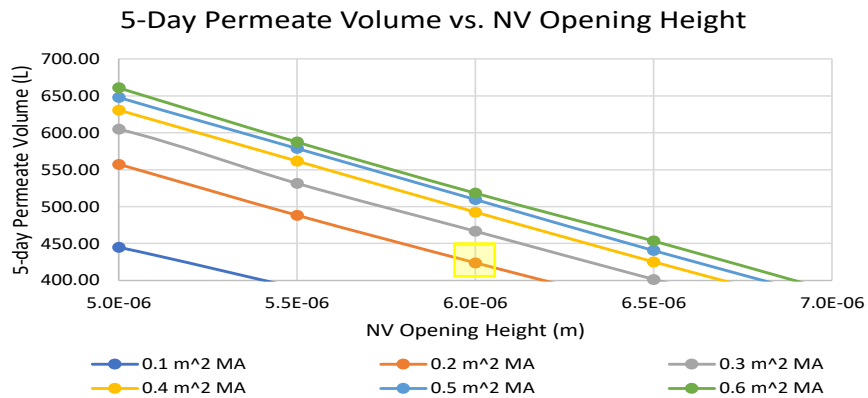


Figure 3.16. 5-Day Permeate Volume vs. Needle Valve (NV) Opening Height for different membrane areas (MA)

Table 3.8. Tuned NV Opening Heights

Sea State	NV Opening Height (m)
W1	3.0E-06
W2	4.0E-06
W3	6.0E-06
W4	1.1E-05
W5	1.3E-05
W6	1.4E-05

Using the optimized membrane area and needle valve opening heights, the overall system performance was estimated for the six sea states. Tables 3.9, 3.10, 3.11, 3.12, and 3.13 list the average values for system pressure, permeate flow rate, permeate concentration, and recovery for each sea state for the different regular and irregular wave model setups. The regular wave results do not provide a very realistic estimation because the regular wave conditions do not accurately approximate the real ocean conditions. Nevertheless, the regular wave simulation is useful as a demonstration that the numerical model works properly and generates reasonable results for pressure, permeate flow rate, and permeate concentration under different wave conditions.

Table 3.9. Performance Estimation: Regular Wave (w/ ACC and PRV)

Sea State	P_system (bar)	Qp (mL/s)	Qp (L/min)	Cp (ppm)	Recovery	Total 5-Day Permeate Production (L)	Total 5-Day Cp (ppm)
W1	52.40	1.79	0.1074	287.34	0.58		
W2	62.80	2.62	0.1572	196.46	0.58		
W3	65.10	2.81	0.1686	183.74	0.49	1054.99	217.63
W4	61.70	2.54	0.1524	204.48	0.33		
W5	61.20	2.50	0.1500	207.98	0.30		
W6	57.20	2.17	0.1302	240.29	0.25		

Looking at the irregular wave results in Tables 3.10, 3.11, 3.12, and 3.13, the advantages of using the accumulator and pressure relief valve are not evident simply by looking at the tables. The four tables have similar overall results for permeate production and concentration. However, a closer examination of the irregular wave results clearly shows the need for using the accumulator and pressure relief valve. Figures 3.17(a) and 3.17(b) show plots of system pressure and permeate flow rate vs. time for W6 irregular wave conditions. Looking at the pressure plot, the curve without ACC or PRV has pressure spikes in some cases over 200 bar. Such large pressure spikes can damage system components and ultimately hinder the system performance. Adding the accumulator greatly reduces pressure fluctuation, but the system pressure can still reach over the membrane design pressure of 70 bar, as the plot shows, potentially damaging the RO membrane. Therefore, it is also important to include the pressure relief valve as a safety mechanism. Including both the accumulator and pressure relief valve minimizes fluctuation in pressure and permeate flow rate, giving the best system performance. Appendix B contains system pressure and permeate flow rate plots for all six sea states. For all six sea states, it is clear that the accumulator is effective at reducing fluctuation in pressure and permeate production. The

pressure relief valve does not engage as frequently at the lower sea states when wave excitation is smaller, but engages often at the higher sea states.

Table 3.10: Performance Estimation: Irregular Wave (No ACC or PRV)

Sea State	P_system (bar)	Qp (mL/s)	Qp (L/min)	Cp (ppm)	Recovery	Total 5-Day Permeate Production (L)	Total 5-Day Cp (ppm)
W1	35.80	0.48	0.0286	2263.28	0.26		
W2	35.90	0.53	0.0319	475.57	0.21		
W3	40.10	0.84	0.0505	971.09	0.23		
W4	53.60	1.91	0.1146	387.64	0.23	570.15	1174.25
W5	58.60	2.30	0.1380	1325.14	0.25		
W6	63.40	2.68	0.1608	383.21	0.24		

Table 3.11. Performance Estimation: Irregular Wave (w/ ACC Only)

Sea State	P_system (bar)	Qp (mL/s)	Qp (L/min)	Cp (ppm)	Recovery	Total 5-Day Permeate Production (L)	Total 5-Day Cp (ppm)
W1	35.90	0.47	0.0281	1224.10	0.29		
W2	36.40	0.51	0.0307	1174.71	0.24		
W3	40.20	0.82	0.0491	751.35	0.25		
W4	53.50	1.88	0.1128	370.53	0.27	556.55	678.73
W5	57.90	2.23	0.1338	257.38	0.27		
W6	62.50	2.60	0.1560	216.95	0.27		

Table 3.12. Performance Estimation: Irregular Wave (w/ PRV Only)

Sea State	P_system (bar)	Qp (mL/s)	Qp (L/min)	Cp (ppm)	Recovery	Total 5-Day Permeate Production (L)	Total 5-Day Cp (ppm)
W1	35.80	0.48	0.0286	1128.61	0.26		
W2	35.90	0.53	0.0317	1058.92	0.21		
W3	40.10	0.83	0.0500	1163.64	0.23		
W4	45.60	1.28	0.0768	560.28	0.19	424.54	846.98
W5	48.10	1.46	0.0876	422.25	0.20		
W6	49.00	1.53	0.0918	376.81	0.19		

Table 3.13. Performance Estimation: Irregular Wave (w/ ACC and PRV)

Sea State	P_system (bar)	Qp (mL/s)	Qp (L/min)	Cp (ppm)	Recovery	Total 5-Day Permeate Production (L)	Total 5-Day Cp (ppm)
W1	35.90	0.47	0.0282	1218.63	0.29		
W2	36.40	0.51	0.0308	1304.00	0.24		
W3	40.20	0.82	0.0491	751.41	0.25		
W4	52.20	1.78	0.1068	389.11	0.26	516.98	710.92
W5	54.10	1.93	0.1158	359.89	0.24		
W6	57.70	2.21	0.1326	244.59	0.25		

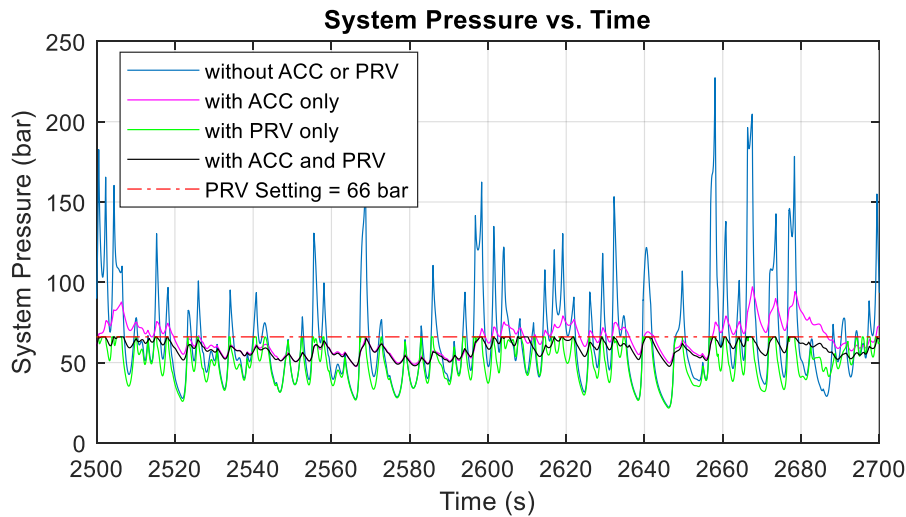


Figure 3.17(a). System Pressure vs. Time Combined Plots, W6 irregular wave

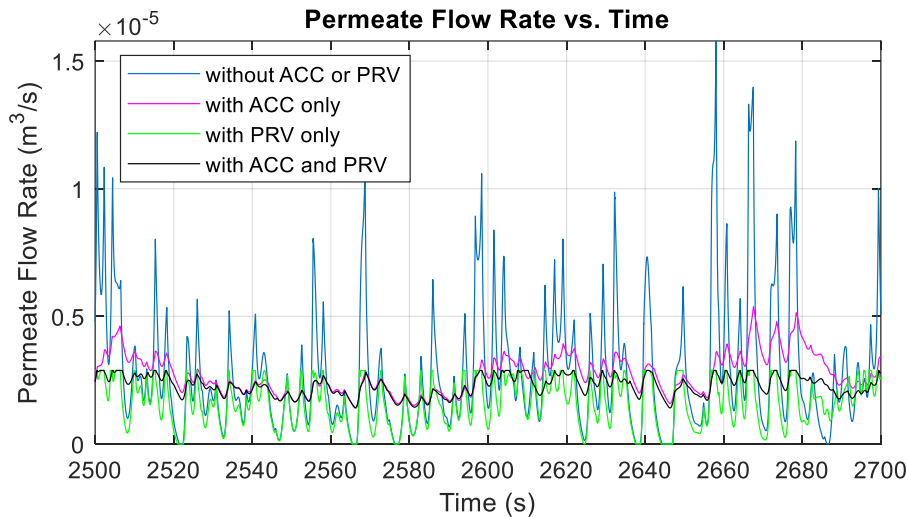


Figure 3.17(b). Permeate Flow Rate vs. Time Combined Plots, W6 irregular wave

With the accumulator and PRV included, Table 3.14 lists the permeate production results along with the brine production results to further quantify the system performance under irregular wave conditions. Over a 5-day testing period, the system can produce 517 L of permeate with a permeate concentration of 711 ppm, which meets the target values of 400 L minimum permeate and less than 1000 ppm permeate concentration. Although sea states W1 and W2 had permeate concentrations over 1000 ppm, the overall permeate salinity was still less than 1000 ppm. The brine salinity and discharge rates were reasonable based on the membrane properties. Figure 3.18 shows plots of the wave profile, system pressure, permeate flow rate, and permeate concentration for the six sea states for 500 s of simulation time. Appendix C contains the full plots for system pressure, permeate flow rate, permeate concentration, and recovery throughout the entire simulation duration. The permeate and brine production results demonstrate that for the six sea states, the system will produce desirable amounts of permeate with sufficiently low concentration and that the brine will be discharged effectively by the system.

Table 3.14. Permeate and Brine Production Results (Irregular wave w/ ACC and PRV)

Sea State	Avg Intake Rates [L/min]	Avg Desalinated Water Production [L/min]	Avg Desalinated Water Salinity [ppm]	Avg Brine Discharge Rates [L/min]	Avg Brine Discharge Salinity [ppm]	Total 5-Day Permeate Production [L]	Total 5-Day Salinity of Desalinated Water [ppm]
W1	0.0936	0.0282	1218.63	0.0654	49516.00	516.98	710.92
W2	0.1188	0.0308	1304.00	0.0876	46686.58		
W3	0.1878	0.0491	751.41	0.1380	46998.63		
W4	0.4050	0.1068	389.11	0.2880	47544.88		
W5	0.4782	0.1158	359.89	0.3468	46418.87		
W6	0.5646	0.1326	244.59	0.3858	46865.52		

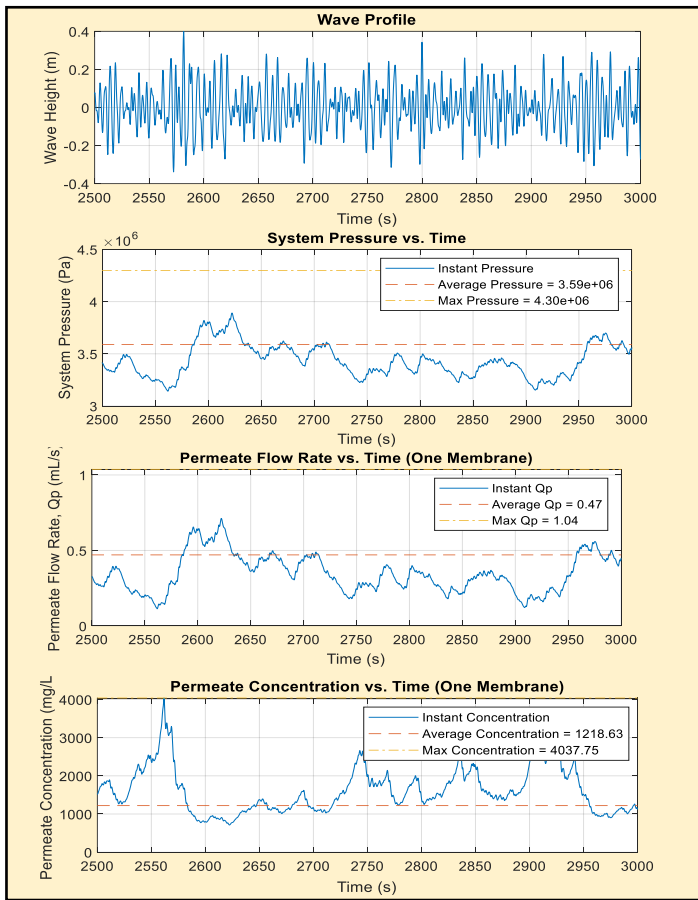


Figure 3.18(a) W1 Irr. Wave (w/ PRV and ACC)

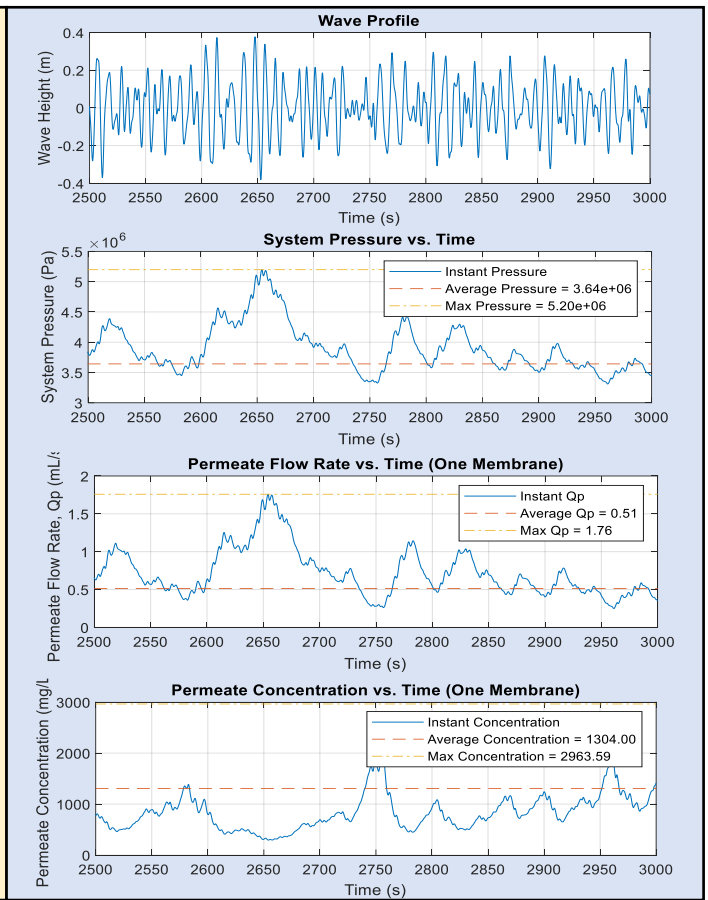


Figure 3.18(b) W2 Irr. Wave (w/ PRV and ACC)

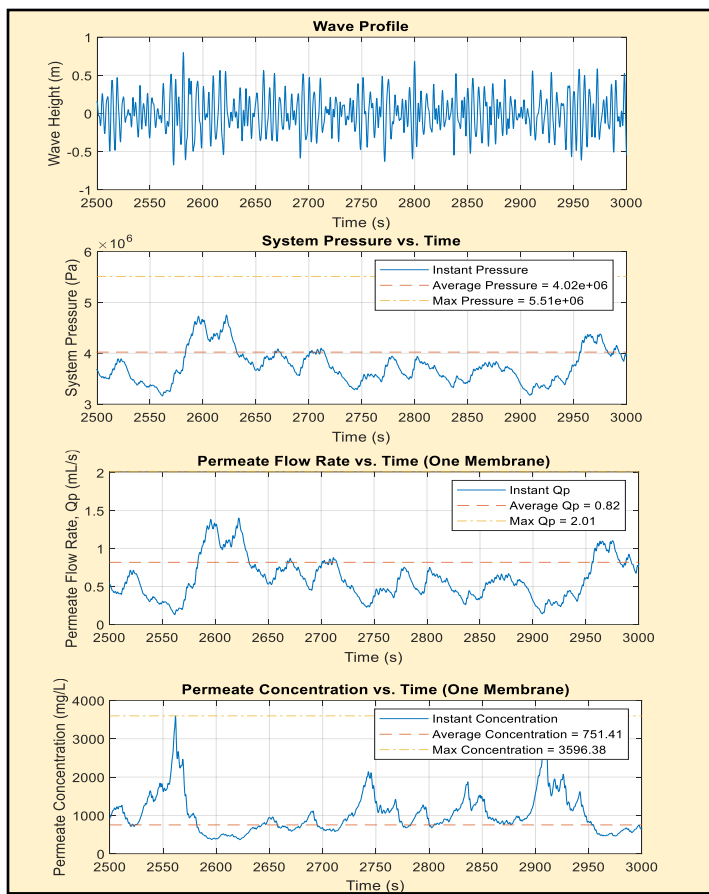


Figure 3.18(c) W3 Irr. Wave (w/ PRV and ACC)

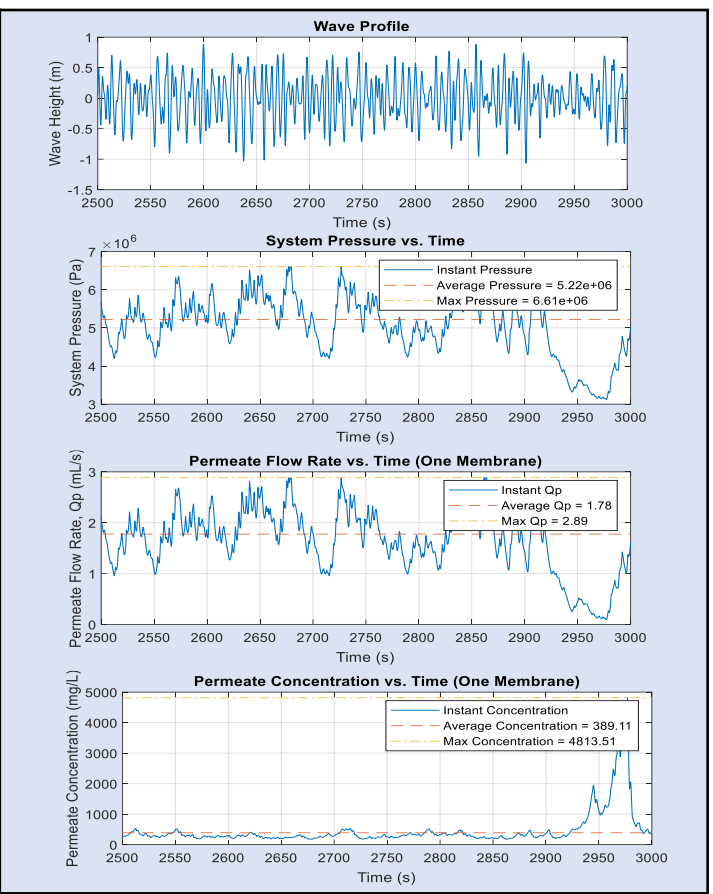


Figure 3.18(d) W4 Irr. Wave (w/ PRV and ACC)

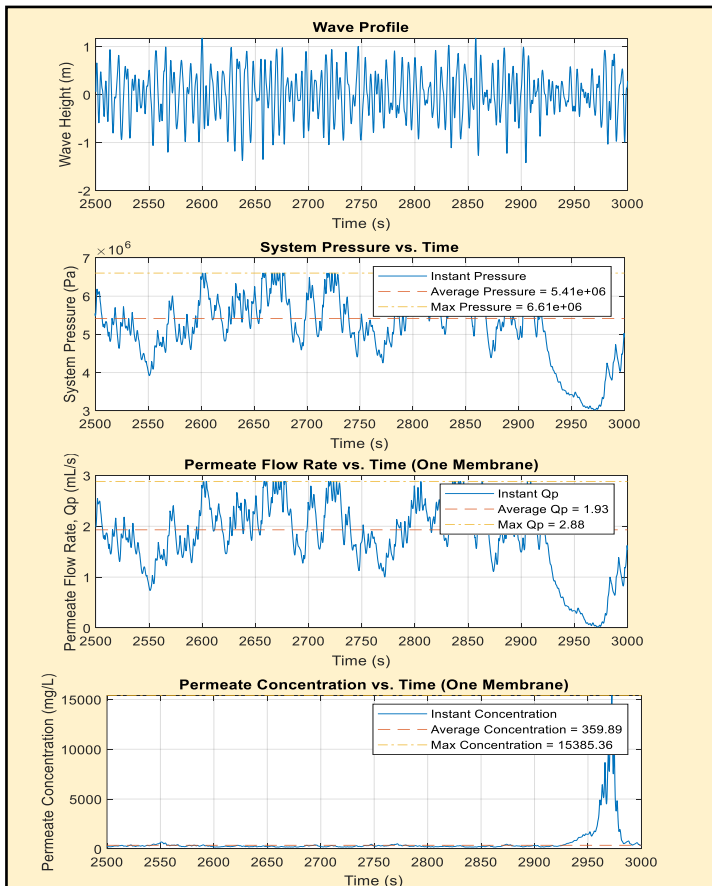


Figure 3.18(e) W5 Irr. Wave (w/ PRV and ACC)

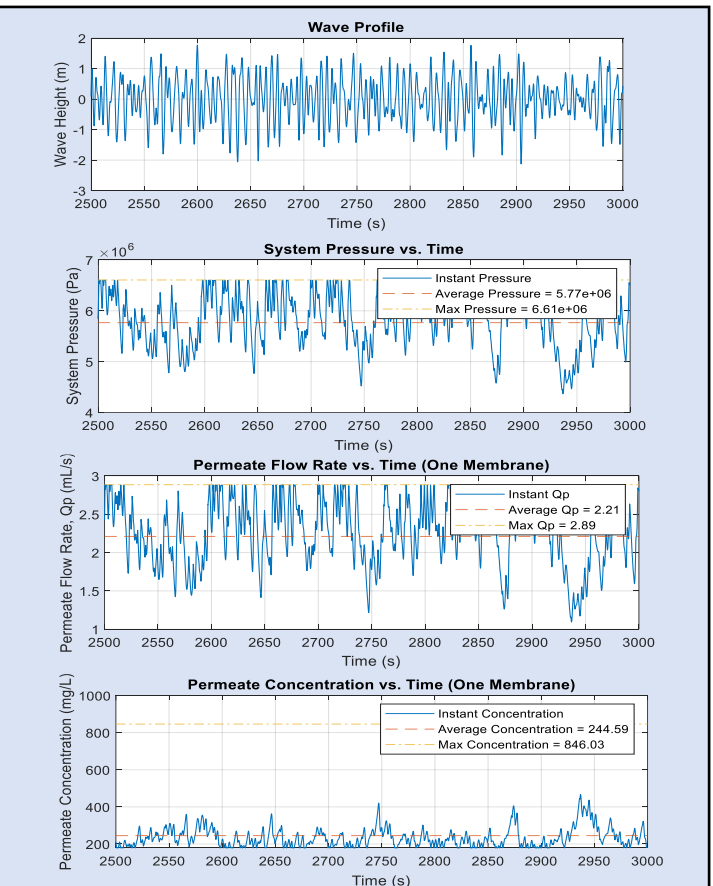


Figure 3.18(f) W6 Irr. Wave (w/ PRV and ACC)

Figure 3.18. Wave profile, system pressure, permeate flow rate, and permeate concentration for the six sea states

3.5 Preliminary Experiment Validation

Preliminary integrated tests were performed using a commercial piston pump and RO module, as shown in Figure 3.19. The piston pump used was a Sarum Hydraulics MP-3-50-4-N-W-R-G-R-20, which has 50 cc per double stroke and can withstand pressures up to 102 bar. A DOW FILMTEC™ SW30-2521 was used for the RO module. The saline water was pressurized by driving the piston pump by hand. As shown in Figure 3.18, the membrane successfully reduced the concentration from 35000 ppm to less than 1000 ppm. The permeate salinity was 859 ppm and the brine salinity was 48900 ppm, which matches well with the numerical modelling results for the permeate and brine salinity shown in Table 3.14. The preliminary experiment demonstrated that the overall system will be able to produce permeate with desirable salinity levels.

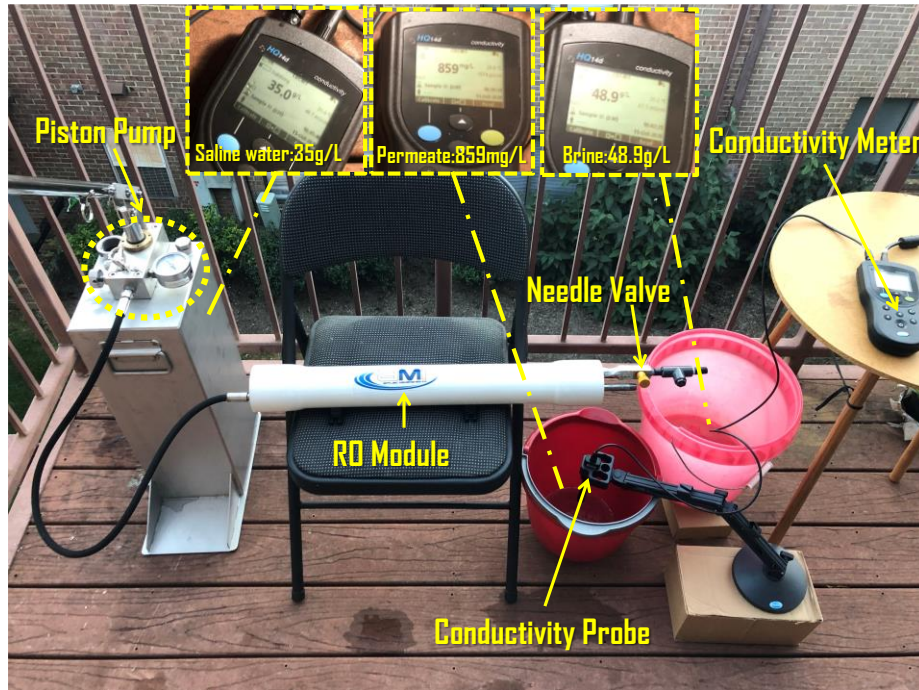


Figure 3.19. Preliminary integrated test

3.6 Summary

This chapter aimed to demonstrate the viability of an oscillating surge wave energy converter and desalination system through numerical modeling. The numerical model was developed in WEC-Sim to simultaneously solve the WEC system dynamics and desalination solution-diffusion model to estimate performance and freshwater production of the system. Six sea states with different wave conditions were used for the study based on ocean data from a potential testing site. By performing an optimization study under the dominant sea state, W3, the optimal membrane area and needle valve opening height were determined to be 0.2 m^2 and $6.0\text{e-}6 \text{ m}$ respectively. Using the optimized membrane area of 0.2 m^2 , the tuned needle valve opening heights for the six sea states were found to be $3.0\text{e-}6 \text{ m}$, $4.0\text{e-}6 \text{ m}$, $6.0\text{e-}6 \text{ m}$, $1.1\text{e-}6 \text{ m}$, $1.3\text{e-}5 \text{ m}$, and $1.4\text{e-}5 \text{ m}$.

After tuning was completed for the membrane area and needle valve opening height, regular wave simulations were performed to demonstrate that the numerical model was working correctly and generated reasonable results. Irregular wave simulations were then executed to

estimate the system performance. The irregular wave simulations showed the importance of including the accumulator and pressure relief valve in the system to reduce pressure fluctuation and prevent over-pressurization of important components like the membrane. Based on the irregular wave results, the system will produce desirable amounts of permeate with sufficiently low concentration and discharge brine effectively. Over a 5-day test period, the numerical model estimated that the system will produce 517 L of permeate with 711 ppm concentration under irregular waves, meeting the minimum target requirements of over 400 L of permeate with concentration less than 1000 ppm. Preliminary experimental results with one membrane yielded a permeate salinity of 859 ppm, agreeing well with the numerical model.

4. Analysis of a Portable Two-Body Attenuator Wave Energy Converter

4.1 Design Overall Concept and Working Principle

The objective of this chapter was to use resonance tuning and numerical simulation to develop a method of power maximization for a small-sized, two-body attenuator wave energy converter. Although analysis work has been performed in literature for two-body attenuators, much of the focus has been on large-scale power generation, as in the cases of Ref. [74], [75], [76], [77], [78], and [79]. However, there is also increasing interest in wave energy conversion at the small scale. For small-sized systems, power maximization through natural frequency tuning is more challenging than for large-sized systems. Based on real ocean conditions, many WECs target a wave period of 5-12 seconds [74], [76], [78], [79], but for small-sized devices it is difficult to achieve a resonant period high enough to be in that range. For large-sized devices, large overall dimensions and physical or added mass can be used to adjust the natural frequency to increase the power [74], [76], [78], [79]. With small-sized attenuators, using such large dimensions and mass is not possible because of portability constraints. This study presents an innovative method for frequency tuning by using a thin tuning plate attached to each body.

The device under consideration in this study is a small-sized, easily portable, two-body attenuator with the power takeoff around the hinge connecting the two bodies, as shown in Figure 4.1. Because of its small size, the device could be easily transported in the back of a vehicle such as a car and carried by one or two people to the ocean for deployment. To ease transportation, the two main bodies could be disconnected and the thin plates folded, as shown in Figure 4.2. Without the tuning plate, each main body has a length of 0.5 m, resulting in a device overall length of about 1 m without the plates.

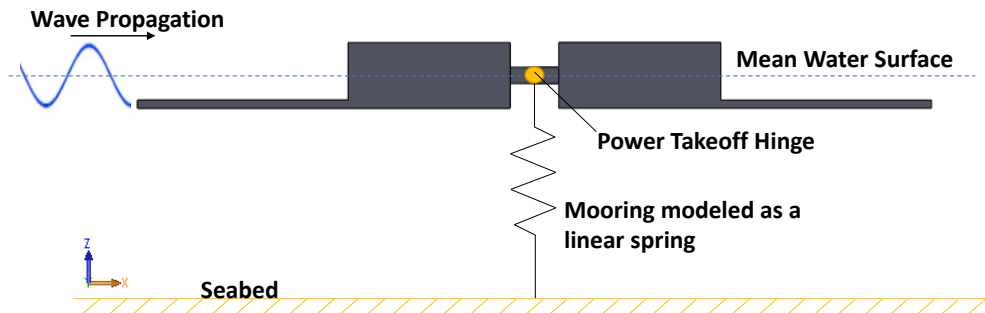


Figure 4.1. Concept diagram for the two-body attenuator

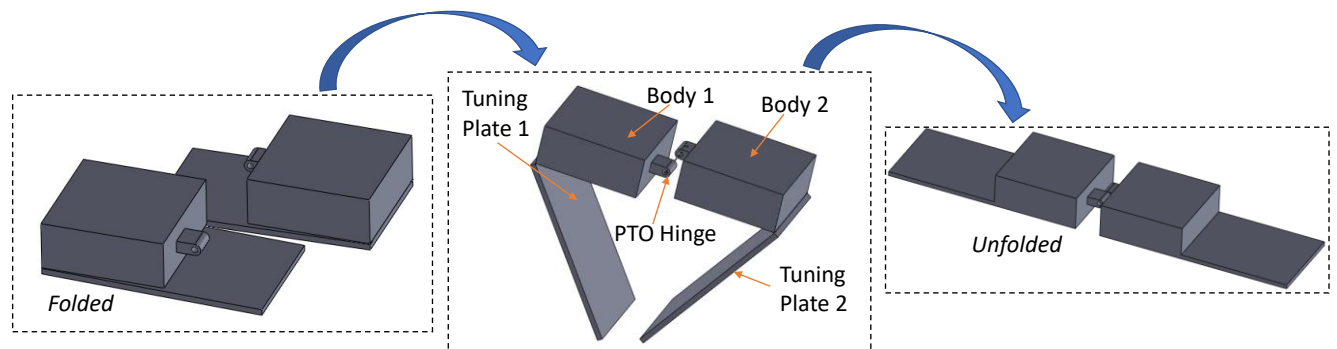


Figure 4.2. System assembly for deployment

4.2 System Governing Equations

Equations of motion were first derived in order to tune the two-body device by matching the device natural frequency to the wave frequency to achieve resonance. In this section (Section 4.2), the equations defined were used for dimensional optimization through natural frequency tuning while Section 4.4 describes the equations and models used to obtain the time domain results. For the two-degree-of-freedom (2DOF) system, the device is simplified so that each body has one DOF in rotation around the hinge point (fixed), as shown in Figure 4.3(a). For the 3DOF system, the hinge is enabled to move in the heave direction with a mooring stiffness, as shown in Figure 4.3(b).

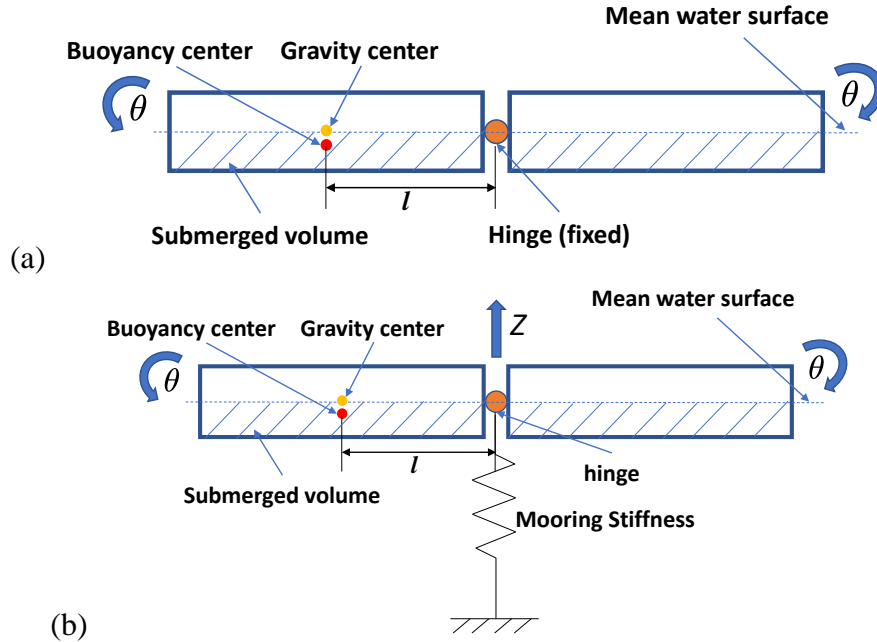


Figure 4.3. Motion schematic of the attenuator WEC: (a) 2DOF (b) 3DOF

The overall equation of motion for the system is given by Equation 4-1 by taking the sum of the moments around the hinge point, where J is the rotational inertia matrix with respect to the PTO hinge, $A(\omega)$ is the added rotational inertia with respect to the PTO at frequency ω , $C(\omega)$ is the PTO damping matrix, K is the hydrostatic stiffness matrix, M is the excitation moment vector, and θ , $\dot{\theta}$, and $\ddot{\theta}$ are the angular displacement, velocity, and acceleration respectively. Equation 4-2 shows the expanded matrices.

$$(J + A(\omega))\ddot{\theta} + C(\omega)\dot{\theta} + K\theta = M \quad (4-1)$$

$$J = \begin{bmatrix} J_1 & 0 \\ 0 & J_2 \end{bmatrix}, A(\omega) = \begin{bmatrix} A_1(\omega) & 0 \\ 0 & A_2(\omega) \end{bmatrix}, C(\omega) = \begin{bmatrix} c & -c \\ -c & c \end{bmatrix}, K = \begin{bmatrix} k & 0 \\ 0 & k \end{bmatrix} \quad (4-2)$$

The hydrostatic stiffness of the two bodies was determined using the following procedure. Equation 4-3 was derived by taking the vertical summation of the forces at hydrostatic equilibrium, where m is the body mass, g is acceleration due to gravity, ρ is the water density, and V_0 is the submerged volume with zero flap rotation.

$$mg = \rho g V_0 \quad (4-3)$$

By taking the sum of the moments for the individual body around the hinge point, Equation 4-4 was obtained, where R_m is the hydrostatic moment on one body with respect to the PTO hinge and V_θ is the submerged volume. Using a Taylor series, V_θ is expanded around $\theta = 0$ where k_1, k_2, \dots are the coefficients of the Taylor series.

$$\begin{aligned} R_m &= mgl\cos\theta - \rho g V_\theta l\cos\theta \\ &= mgl\cos\theta - \rho g(V_0 + k_1\theta + k_2\theta^2 + \dots)l\cos\theta \end{aligned} \quad (4-4)$$

The derivative of Equation 4-4 was taken with respect to θ to obtain Equation 4-5, i.e., the stiffness is equal to the rate of change of moment R_m at $\theta = 0$. Solving for the individual body stiffness by manipulating the expression, it was shown that the individual body stiffness is equal to the body's rate of change in volume with respect to θ , as shown in Equation 4-6. The rotational hydrostatic stiffness of two bodies of an arbitrary shape can be determined by calculating k_I numerically, such as with a computer-aided design software.

$$\begin{aligned} -k &= \left. \frac{\partial R_m}{\partial \theta} \right|_{\theta=0} \\ &= -mgl\sin\theta - \rho g(k_1 + 2k_2\theta + \dots)l\cos\theta + \rho g(V_0 + k_1\theta + k_2\theta^2 + \dots)l\sin\theta \Big|_{\theta=0} = -\rho g k_1 l \end{aligned} \quad (4-5)$$

$$k_1 = \left. \frac{\partial V_\theta}{\partial \theta} \right|_{\theta=0} \quad (4-6)$$

The undamped natural frequency for each body is given by Equation 4-7. Because it is a hydrodynamic system, the spring stiffness can be replaced by the body's hydrostatic stiffness and the mass becomes the sum of the inertia due to the body's dry material J_M and the inertia due to added mass when submerged J_A . Equation 4-8 can be used to calculate the natural period.

$$\omega_n = \sqrt{\frac{k}{J_M + J_A}} \quad (4-7)$$

$$T_n = \frac{2\pi}{\omega_n} \quad (4-8)$$

4.3 Frequency Domain Natural Frequency Tuning

The natural frequency of each body was tuned to match the wave frequency in order to maximize power absorption and achieve resonance. Based on common wave conditions on the US east coast, the target wave period was 6 seconds [34]. Using the CAD model, the dry material inertia J_M was obtained. A hydrodynamic diffraction solution was performed in the frequency domain using the BEM solver ANSYS AQWA to obtain J_A and k in order to use Equation 4-7 [58]. It was necessary to keep the overall main body dimensions approximately close to the target dimensions shown in Figure 4.4 because of the portability constraint.

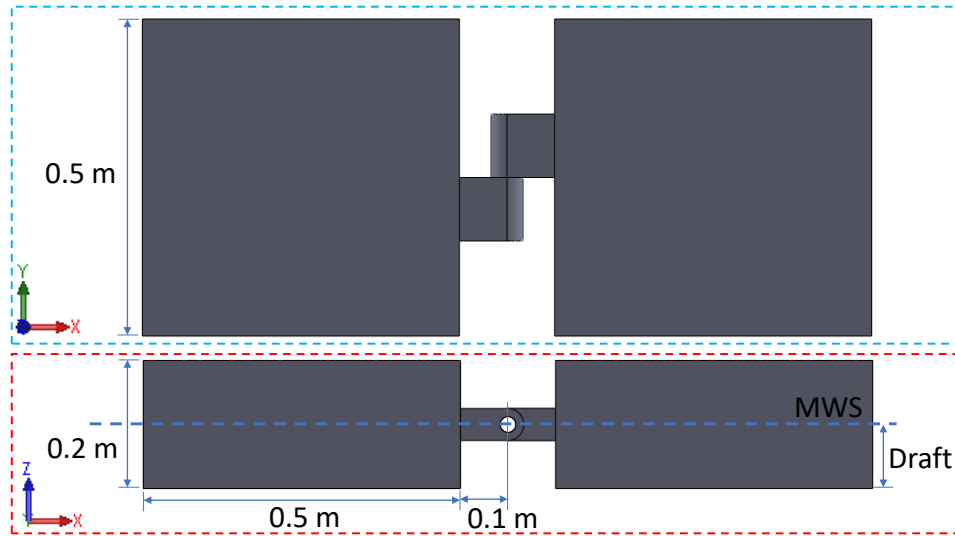


Figure 4.4. Desired main body overall dimension constraints

During the tuning process, it was difficult to achieve a natural period much larger than 1 second because the hydrostatic stiffness k remained large relative to J_M and J_A even when various body dimensions were changed. A sample of geometry parameters and results for the baseline shape, a rectangular flat plate, are shown in Table 4.1. Increasing the buoy length in order to achieve an increased added mass is an intuitive modification. However, as Case 7 in Table 4.1 illustrates, increasing the buoy length greatly increased J_M and J_A , but hydrostatic stiffness also increased significantly, preventing the natural frequency from matching the targeted wave frequency.

Table 4.1. Sample of Geometry Variation Parameters and Natural Frequency Results, Baseline Shape

Case #	Variable Parameters					Results				
	Draft (m)	Thickness (m)	Width (m)	Buoy Length (m)	Lever Length (m)	K (N-m/rad)	J_M (kg*m ²)	J_A (kg.m ² /rad)	ω_n (rad/s)	Tn (s)
1 (initial)	0.15	0.2	0.50	0.5	0.075	308.36	1.11	6.27	6.64	0.97
2	0.10	0.2	0.50	0.5	0.075	305.34	0.74	6.39	6.54	0.96
3	0.25	0.3	0.50	0.5	0.075	302.08	2.00	6.10	6.11	1.03
4	0.15	0.2	0.75	0.5	0.075	462.54	1.81	11.35	5.93	1.06
5	0.15	0.2	0.50	0.5	0.150	445.00	1.15	9.24	6.55	0.96
6	0.15	0.2	0.50	0.5	0.500	1456.47	6.61	32.11	6.13	1.02
7	0.15	0.2	0.50	1.0	0.075	2061.67	7.19	56.73	5.68	1.11
8	0.45	0.5	0.50	0.5	0.075	289.51	4.93	5.35	5.31	1.18

Parameter varied from initial

A new geometry feature was added to make tuning possible after tuning the device using traditional geometry proved inadequate. Using a thin, submerged flat plate added to the existing shape, it was possible to significantly increase the added mass without greatly increasing the

hydrostatic stiffness. To tune the body to the wave frequency, the main body dimensions could be kept at the target values while the plate length was varied, as shown in Figure 4.5. The natural periods for the three different body shapes were tuned to approximately 6 s, as shown in Table 4.2.

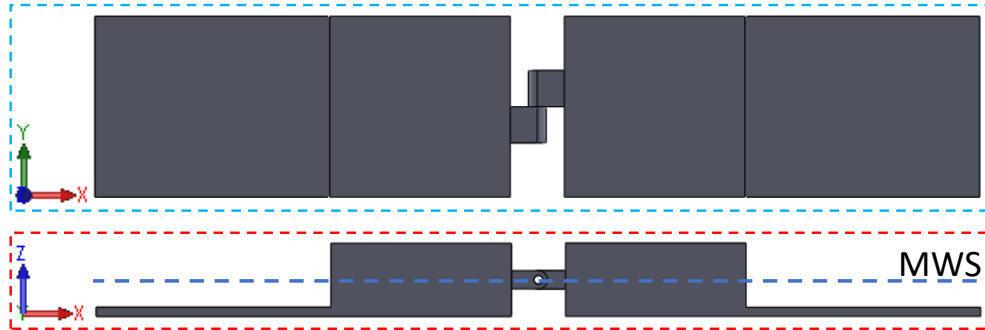


Figure 4.5. Two-body attenuator with thin tuning plate

Table 4.2. Tuned Natural Frequency for Each Shape

Shape	Thin Plate Length (m)	Body Density (kg/m ³)	K (N-m/rad)	J_M (kg*m ²)	J_A (kg.m ² /rad)	wn (rad/s)	Tn (s)
Rectangular	0.90	605.63	338.03	2.52	298.90	1.06	5.93
Elliptical	0.95	627.04	341.74	1.78	319.71	1.03	6.09
Quadrilateral	0.95	674.79	345.85	2.29	320.69	1.04	6.06

Figure 4.6 shows the three different body cross sections used for the analysis: rectangular, elliptical, and quadrilateral. Commonly studied cross sections found in literature such as Ref. [74] and [75] were used to select the shapes. For each body, a draft of 0.1 m was used, putting the mean water surface in the center of the cross section. Using a smaller draft would further increase portability by minimizing body weight because body weight is proportional to displaced volume, as shown in Equation 4-3. However, using a smaller draft would reduce the submerged body width for tapered shapes like the elliptical and quadrilateral. Reducing the submerged body width reduces the excitation force because less body width exposed to the incoming wave front means less energy transferred to the body, leading to a reduction in power absorption. Therefore, the study is a fairer comparison if the submerged widths are the same for all three geometries.

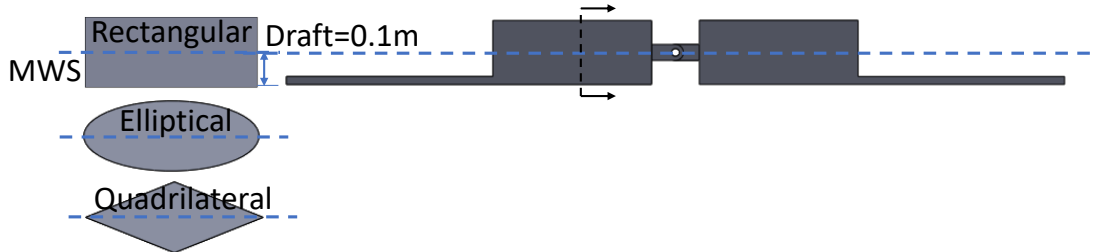


Figure 4.6. Body cross sections used for analysis

4.4 Time Domain Power Absorption Simulation

Power absorption modeling was performed using a time-domain numerical model created in WEC-Sim to solve the system dynamics. A simplified 2DOF model was first used followed by

a more realistic 3DOF model. In the WEC-Sim software, the dynamic response is calculated by solving the equation of motion for each body around its center of gravity using Equation 4-9, where M is the mass matrix, \ddot{X} is the (translational and rotational) acceleration vector of the body, $F_{exc}(t)$ is the wave excitation force and torque vector, $F_{rad}(t)$ is the force and torque vector resulting from wave radiation, $F_{pto}(t)$ is the PTO force and torque vector, $F_v(t)$ is the damping force and torque vector, $F_B(t)$ is the net buoyancy restoring force and torque vector, and $F_m(t)$ is the force and torque vector resulting from mooring connection [57]. The equations in Section 4.2 were only used for dimensional optimization while Equation 4-9 was used to determine the time-domain results.

$$M\ddot{X} = F_{exc}(t) + F_{rad}(t) + F_{pto}(t) + F_v(t) + F_B(t) + F_m(t) \quad (4-9)$$

Figure 4.7 shows the Simulink model for the 2-body attenuator with two degrees of freedom. In the 2DOF model, a rotational constraint is used to constrain the two rigid bodies to rotate around a fixed center point. The heaving motion is not considered for the 2DOF model. It is as if the center point is attached to a fixed structure. Based on the relative velocity between the two bodies, the rotational PTO captures power according to Equation 4-10 where c is the PTO rotational damping and $\dot{\theta}_{rel}$ is the relative rotational velocity. Equation 4-10 assumes constant PTO damping with respect to the relative rotational velocity between the two bodies.

$$P = c\dot{\theta}_{rel}^2 \quad (4-10)$$

For each simulation case, there was a ramp time of 150 s and time step of 0.05 s. The regular wave simulations used a duration of 500 s. The irregular wave simulations used a duration of 750 s to give additional simulation data for taking the average power because power fluctuates more under irregular waves due to the wave spectrum. After the simulation reached steady state, average power was calculated from the instantaneous PTO power. Each case used a wave period of $T=6$ s and wave height of $H=0.5$ m. A water depth of 5 m was used assuming that the two-body attenuator would be deployed close to shore. To study drag effects, four different drag coefficients were used: $C_d=0.5, 1, 1.5, 2$. Based on literature such as Ref. [80] and [81], these four drag coefficients were determined to be in the reasonable range.

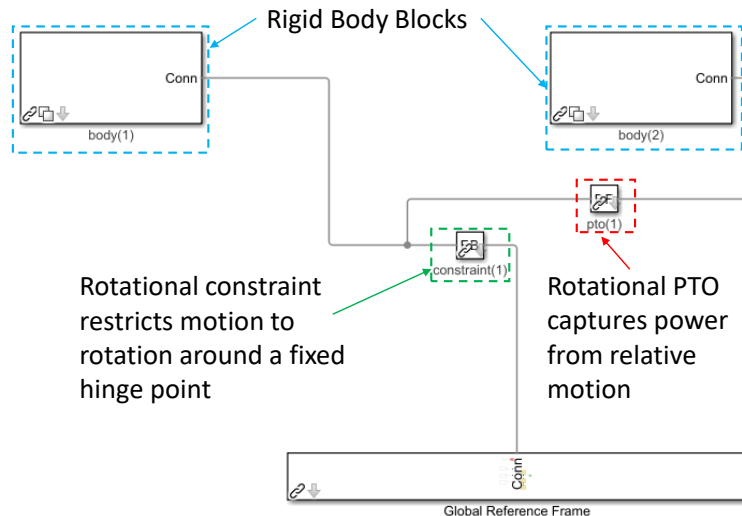


Figure 4.7. Simulink model of the 2DOF system

WEC-Sim’s multiple condition run (MCR) feature was used to run a series of cases with different rotational damping values in order to obtain the maximum power and optimal damping for each cross section and Cd. For every cross section, each Cd was used with rotational damping from 0-500 Nsm/rad with a step of 10 Nsm/rad, resulting in 50 cases for each Cd. The mean power per wave front width that is available in the wave is known as the wave energy flux, J . Equation 4-11 can be used to calculate J , where ρ is the water density, g is acceleration due to gravity, T is wave height, and H is wave period [82]. The amount of wave crest width that is completely captured and absorbed by the WEC is known as the capture width (CW). It can be calculated using Equation 4-12 by taking the ratio of absorbed wave power P and wave energy flux J . The capture width ratio (CWR) was calculated to quantify the hydrodynamic efficiency by dividing the capture width by the device characteristic dimension L , as shown in Equation 4-13 [63]. For the case of the two-body attenuator, the characteristic dimension is the submerged width of 0.5 m that is perpendicular to the incoming wave front.

$$J = \frac{\rho g^2 T H^2}{64\pi} \quad (4-11)$$

$$CW = P/J \quad (4-12)$$

$$CWR = CW/L \quad (4-13)$$

After performing the 2DOF simulation, a 3DOF model was used to account for the heave motion of the WEC, as shown in Figure 4.8. A non-hydro body was connected to the seabed using a translational constraint, allowing the device to heave up and down. The non-hydro body does not have any hydrodynamic interaction in the model and is only used to enable the heave motion. Two rotational PTOs connect the side bodies to the non-hydro body, allowing them to pitch around the non-hydro body. The two PTO damping values were set equal to each other. A mooring stiffness acting in the heave direction was added to the non-hydro body to simulate a single mooring line attached to the WEC rotational point. Power absorption was calculated according to Equation 4-10 based on the relative velocity of the two bodies.

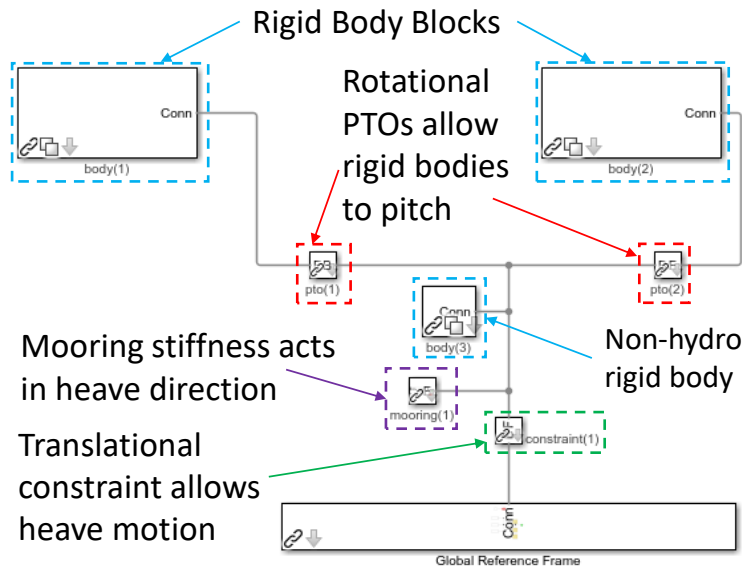


Figure 4.8. Simulink model of the 3DOF system

Two different studies were performed using the 3DOF model: a drag study and mooring stiffness study. The same wave period, height, and water depth were used as the 2DOF model. Also, the same ramp time and simulation duration were used as the 2DOF model. For the drag study, the same four drag coefficients were used as the 2DOF model. A baseline value for the mooring stiffness $k_{mooring}$ was used for the drag study by setting $k_{mooring}$ equal to the combined heave hydrostatic stiffness $k_{hydrostatic}$ of the two side bodies. The value for hydrostatic stiffness was obtained from the AQWA solution. The baseline mooring stiffness used was $k_{mooring}=k_{hydrostatic}=5277.2$ N/m, the same for all three cross section geometries. A smaller time step of 0.025 s was necessary because of the increased system stiffness due to the mooring. Like the 2DOF model, for every cross section, each Cd was used with rotational damping from 0-500 Nsm/rad with a step of 10 Nsm/rad, resulting in 50 cases for each Cd.

For the mooring stiffness study, a series of different mooring stiffness values were used: $k_{mooring}=k_{hydrostatic} * 0.1$, $k_{mooring}=k_{hydrostatic}$, $k_{mooring}=k_{hydrostatic} * 10$, $k_{mooring}=k_{hydrostatic} * 100$. As stiffness increased, the model required a smaller time step to run. The time steps used for the different mooring stiffnesses were 0.025 s, 0.025 s, 0.01 s, 0.0025 s. The mooring stiffness study was performed using regular waves. As with the drag study, the rotational damping was varied from 0-500 Nsm/rad with a step of 10 Nsm/rad.

4.5 Results and Discussion

Figures 4.9, 4.10, and 4.11 show the 2DOF regular and irregular wave power absorption results for the three shapes under different drag coefficients. The results for optimal damping, maximum power, and capture width ratio for the three shapes with different drag coefficients are summarized in Tables 4.3 and 4.4. Looking at all the shapes and drag coefficients, maximum power occurred when the rotational damping value was 80-160 Nsm/rad. The rectangular shape with Cd 0.5 had the highest max power among the different shapes and drag coefficients: 37.33 W with CWR of 10.15% for regular waves and 11.03 W with 3.00% CWR for irregular waves. For a given drag coefficient, there is not much difference in the power absorption between the shapes. The small difference is logical because the submerged body widths are the same for each shape, so the different shapes would be expected to have similar excitation forces and therefore similar power absorption for the same drag coefficient.

Table 4.3. 2DOF Regular Wave Power Results Summary

Cd	Rectangular			Elliptical			Quadrilateral		
	C_opt (Nsm/rad)	P_max (W)	CWR	C_opt (Nsm/rad)	P_max (W)	CWR	C_opt (Nsm/rad)	P_max (W)	CWR
0.5	80	37.33	10.15%	90	33.51	9.11%	90	32.50	8.83%
1.0	110	30.28	8.23%	120	27.09	7.36%	120	27.12	7.37%
1.5	130	26.07	7.09%	140	23.40	6.36%	140	23.71	6.44%
2.0	150	23.16	6.29%	160	20.82	5.66%	160	21.20	5.76%

Table 4.4. 2DOF Irregular Wave Power Results Summary

Cd	Rectangular			Elliptical			Quadrilateral		
	C_opt (Nsm/rad)	P_max (W)	CWR	C_opt (Nsm/rad)	P_max (W)	CWR	C_opt (Nsm/rad)	P_max (W)	CWR
0.5	80	11.03	3.00%	120	10.15	2.76%	120	10.22	2.78%
1.0	110	9.02	2.45%	150	8.32	2.26%	150	8.47	2.30%
1.5	130	7.89	2.15%	170	7.29	1.98%	170	7.45	2.02%
2.0	150	7.13	1.94%	190	6.60	1.79%	190	6.75	1.83%

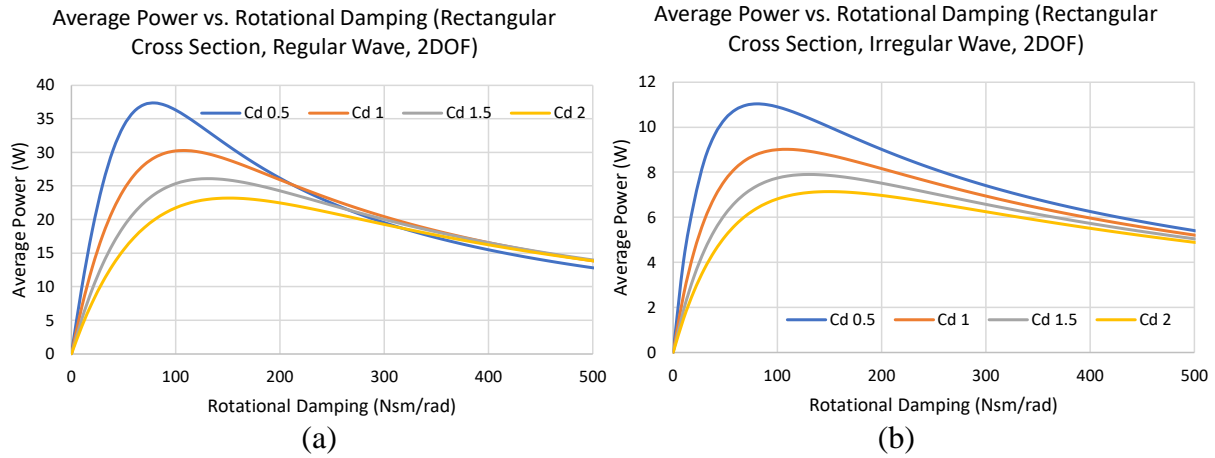


Figure 4.9. 2DOF power results, rectangular cross section

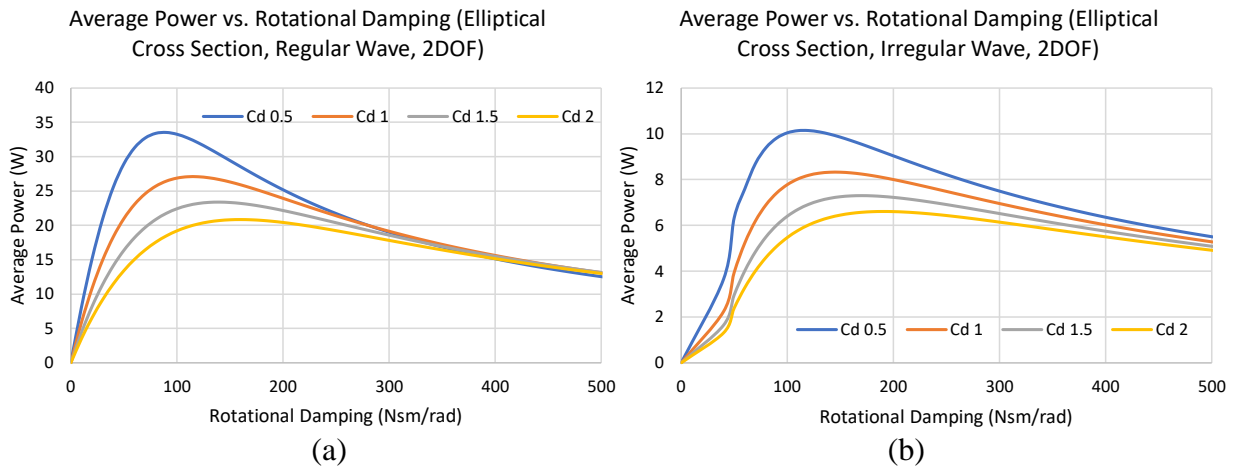


Figure 4.10. 2DOF power results, elliptical cross section

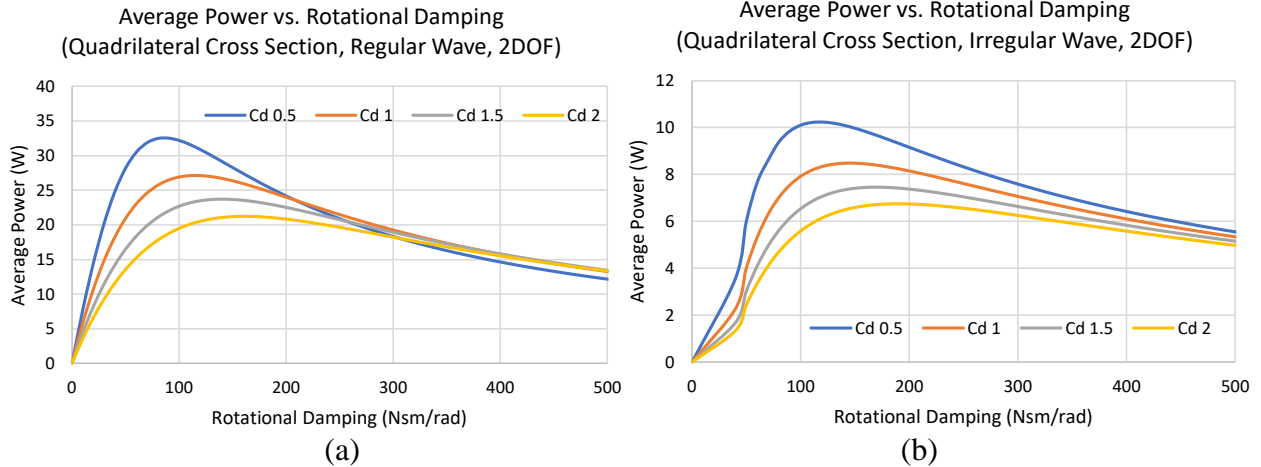


Figure 4.11. 2DOF power results, quadrilateral cross section

The two bodies tend to rotate together as one when rotational damping becomes large, causing small relative motion and therefore small power extracted by the PTO. This effect is illustrated in Figures 4.12 and 4.13. For the smaller damping values like 80 Nsm/rad, the rotational velocity of the two bodies is out of phase, leading to larger relative velocity between the bodies and therefore larger power. With large damping values such as 1000 Nsm/rad, the rotational velocity of the two bodies is nearly in phase, resulting in low relative velocity and consequently low power.

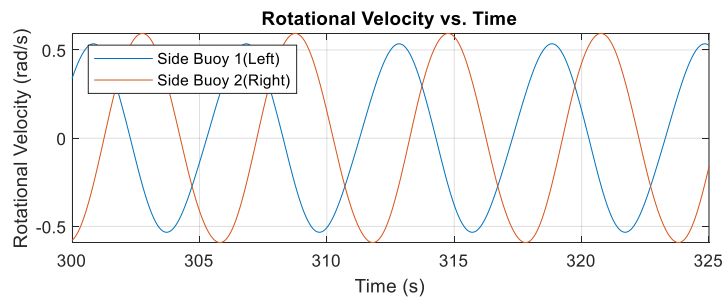


Figure 4.12. Rotational velocity, rectangular cross section, 80 Nsm/rad damping, 0.5 Cd, regular wave

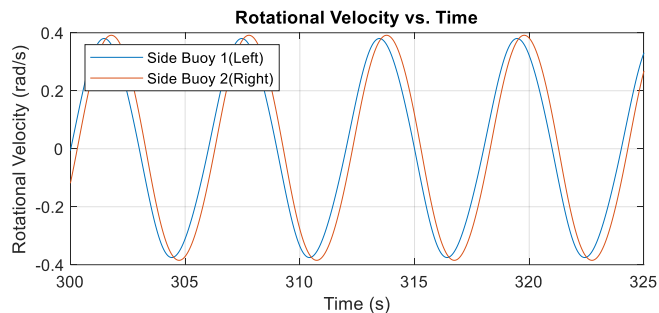


Figure 4.13. Rotational velocity, rectangular cross section 1000 Nsm/rad damping, 0.5 Cd, regular wave

In actuality, tapered cross section geometries such as the elliptical and quadrilateral shapes would have lower drag coefficients. A possible comparison is to compare the maximum power between the shapes using approximate drag coefficients, such as $C_d=1$ for the elliptical shape, $C_d=1.5$ for the quadrilateral, and $C_d=2$ for the rectangular, as shown in Figure 4.14 [81]. Using this comparison, for regular waves, the elliptical shape would have the highest maximum power of 27.09 W with 7.36% CWR at 120 Nsm/rad optimal damping. The quadrilateral shape would have the second highest power of 23.71 W with 6.44% CWR at 140 Nsm/rad optimal damping. The rectangular shape would have the lowest power of 23.16 W with 6.29% CWR at 150 Nsm/rad optimal damping. For irregular waves, the ranking would be the elliptical with 8.32 W with 2.26% CWR at 150 Nsm/rad optimal damping, the quadrilateral with 7.45 W with 2.02% CWR at 170 Nsm/rad optimal damping, and the rectangular with 7.13 W with 1.94% CWR at 150 Nsm/rad optimal damping.

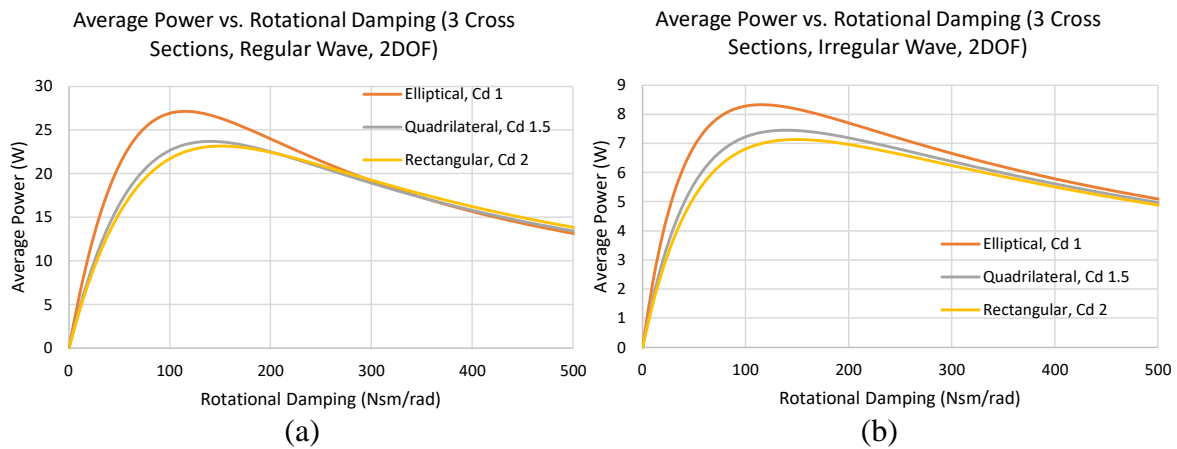


Figure 4.14. 2DOF power results comparison with approximate drag coefficients

Figures 4.15, 4.16, and 4.17 show the results of the 3DOF drag study. The drag study results for optimal damping, maximum power, and capture width ratio for the three shapes are summarized in Tables 4.5 and 4.6. Maximum power occurred with rotational damping from 160-380 Nsm/rad. As with the 2DOF study, the rectangular shape with $C_d 0.5$ had the highest max power out of all the shapes and drag coefficients: 33.04 W with 8.98% CWR for regular waves and 8.51 W with 2.31% CWR for irregular waves. Like the 2DOF study, the difference in power absorption is small between the shapes for the same drag coefficient, which is logical because the submerged body width is the same for all three shapes.

Table 4.5. 3DOF Drag Study Regular Wave Power Results Summary ($k_m=k_h$)

Cd	Rectangular			Elliptical			Quadrilateral		
	C_opt (Nsm/rad)	P_max (W)	CWR	C_opt (Nsm/rad)	P_max (W)	CWR	C_opt (Nsm/rad)	P_max (W)	CWR
0.5	160	33.04	8.98%	180	28.65	7.79%	180	28.59	7.77%
1.0	200	25.61	6.96%	210	22.52	6.12%	220	22.46	6.10%
1.5	230	21.48	5.84%	250	19.00	5.16%	260	18.94	5.15%
2.0	260	18.81	5.11%	280	16.68	4.53%	290	16.62	4.52%

Table 4.6. 3DOF Drag Study Irregular Wave Power Results Summary ($k_m=k_h$)

Cd	Rectangular			Elliptical			Quadrilateral		
	C_opt (Nsm/rad)	P_max (W)	CWR	C_opt (Nsm/rad)	P_max (W)	CWR	C_opt (Nsm/rad)	P_max (W)	CWR
0.5	130	8.51	2.31%	150	7.60	2.07%	150	7.59	2.06%
1.0	200	6.82	1.85%	230	6.18	1.68%	240	6.16	1.67%
1.5	260	6.00	1.63%	310	5.51	1.50%	310	5.48	1.49%
2.0	320	5.50	1.50%	390	5.10	1.39%	380	5.06	1.37%

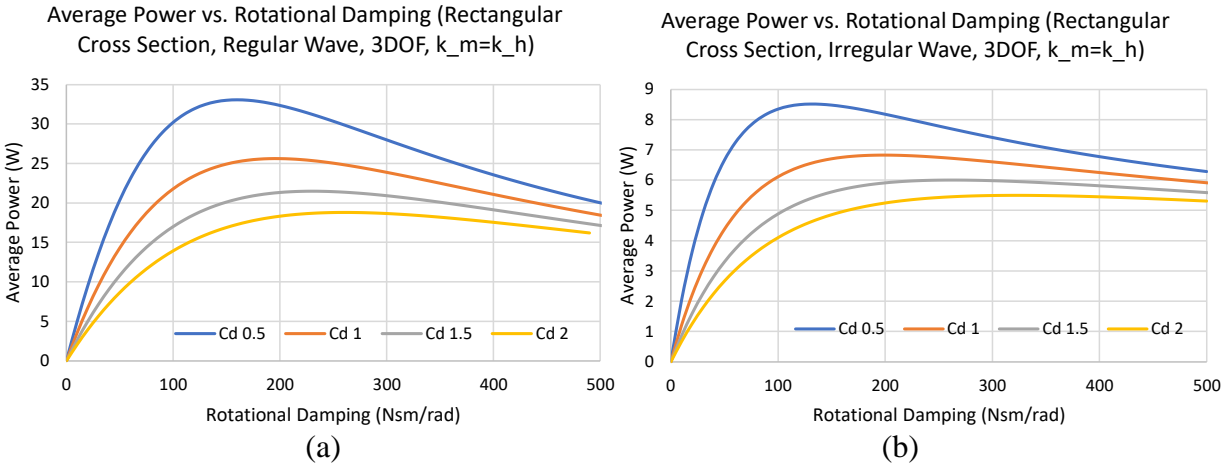


Figure 4.15. 3DOF drag study power results, rectangular cross section

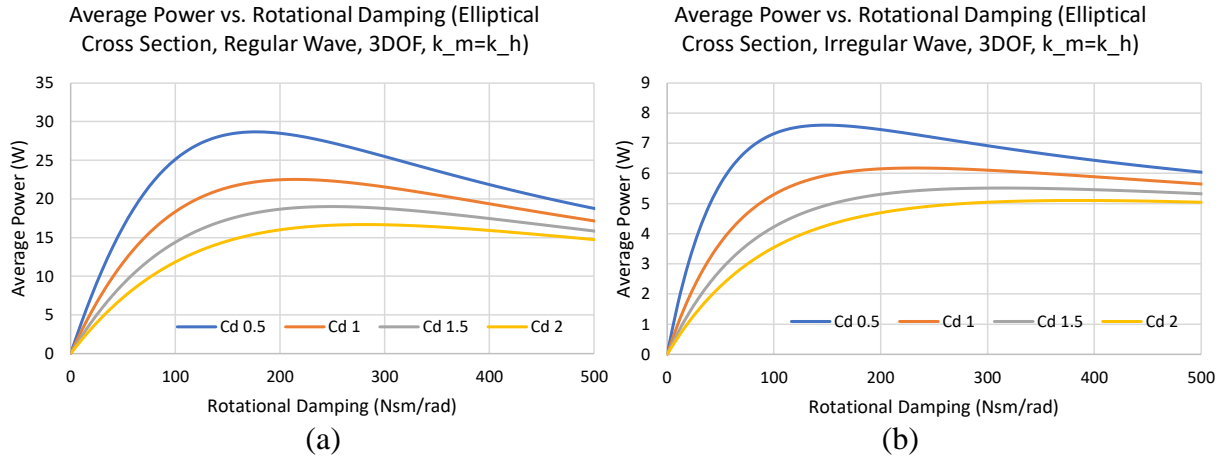


Figure 4.16. 3DOF drag study power results, elliptical cross section

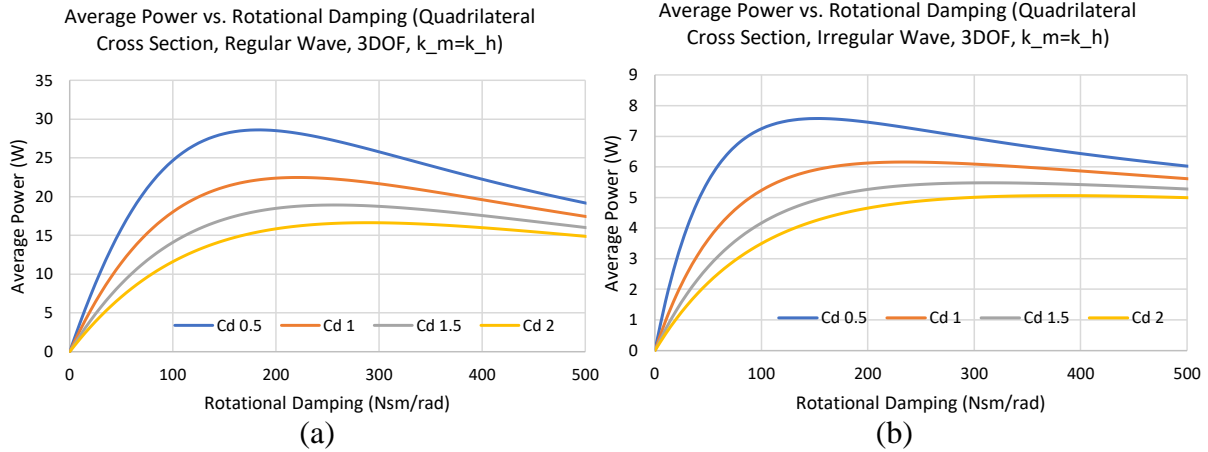


Figure 4.17. 3DOF drag study power results, quadrilateral cross section

As with the 2DOF study, it is possible to compare the 3DOF drag study results using an approximate drag coefficient for each shape, as shown in Figure 4.18. Using this comparison, for regular waves, the power absorption ranking would be elliptical with 22.52 W with 6.12% CWR at 210 Nsm/rad optimal damping, quadrilateral with 18.94 W with 5.15% CWR at 260 Nsm/rad optimal damping, and rectangular with 18.81 W with 5.11% CWR at 260 Nsm/rad optimal damping. For irregular waves, the ranking would be elliptical with 6.18 W with 1.68% CWR at 230 Nsm/rad optimal damping, rectangular with 5.50 W with 1.50% CWR at 320 Nsm/rad optimal damping, and quadrilateral with 5.48 W with 1.49% CWR at 310 Nsm/rad optimal damping. This comparison agrees with the 2DOF results, which also showed the elliptical shape to have the highest power when using approximate drag coefficients.

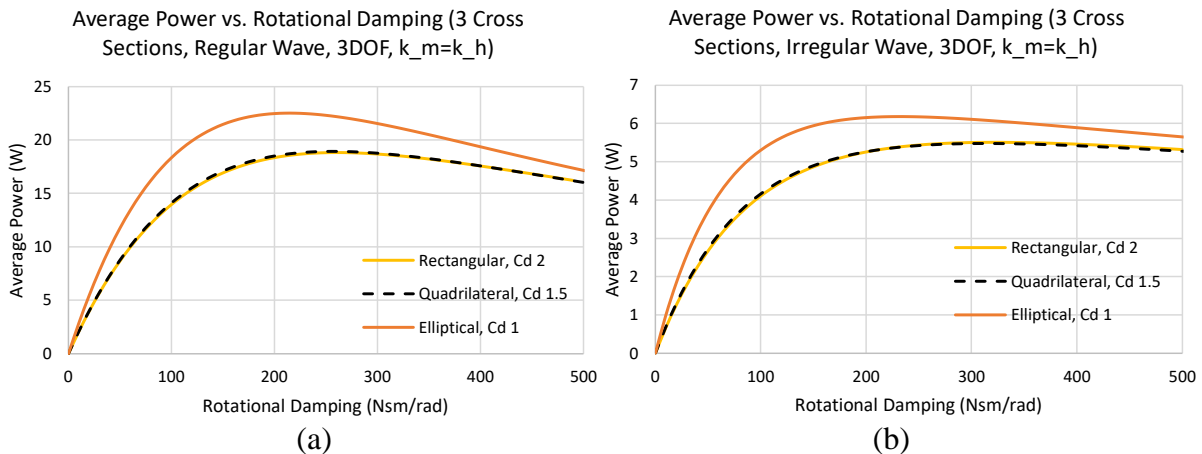


Figure 4.18. 3DOF drag study results comparison with approximate drag coefficients

Figure 4.19 shows the results from the 3DOF mooring stiffness study for the three different shapes. Table 4.7 summarizes the max power results at different mooring stiffnesses for each shape. At low mooring stiffnesses such as the $k_{mooring} = k_{hydrostatic} * 0.1$ case, there was not a significant difference in power absorption between the shapes. At higher mooring stiffnesses such as $k_{mooring} = k_{hydrostatic}$ and greater, the elliptical shape had the highest power absorption, which is logical because the lowest drag coefficient was used with the elliptical shape. The mooring stiffness study also showed that larger mooring stiffness can be used to increase relative

motion between the two bodies and consequently increase the power. The mooring stiffness study is applicable to other WEC types, geometries, and sizes.

Table 4.7. 3DOF Mooring Stiffness Study Results (Regular Wave)

k_m (N/m)	Rectangular (Cd 2)			Elliptical (Cd 1)			Quadrilateral (Cd 1.5)		
	C_{opt} (Nsm/rad)	P_{max} (W)	CWR	C_{opt} (Nsm/rad)	P_{max} (W)	CWR	C_{opt} (Nsm/rad)	P_{max} (W)	CWR
$k_m=k_h*0.1$	190	2.07	0.56%	180	1.97	0.54%	200	2.15	0.58%
$k_m=k_h$	260	18.81	5.11%	210	22.52	6.12%	260	18.94	5.15%
$k_m=k_h*10$	340	40.52	11.01%	270	49.07	13.34%	340	40.64	11.05%
$k_m=k_h*100$	360	44.72	12.15%	280	54.22	14.74%	350	44.82	12.18%

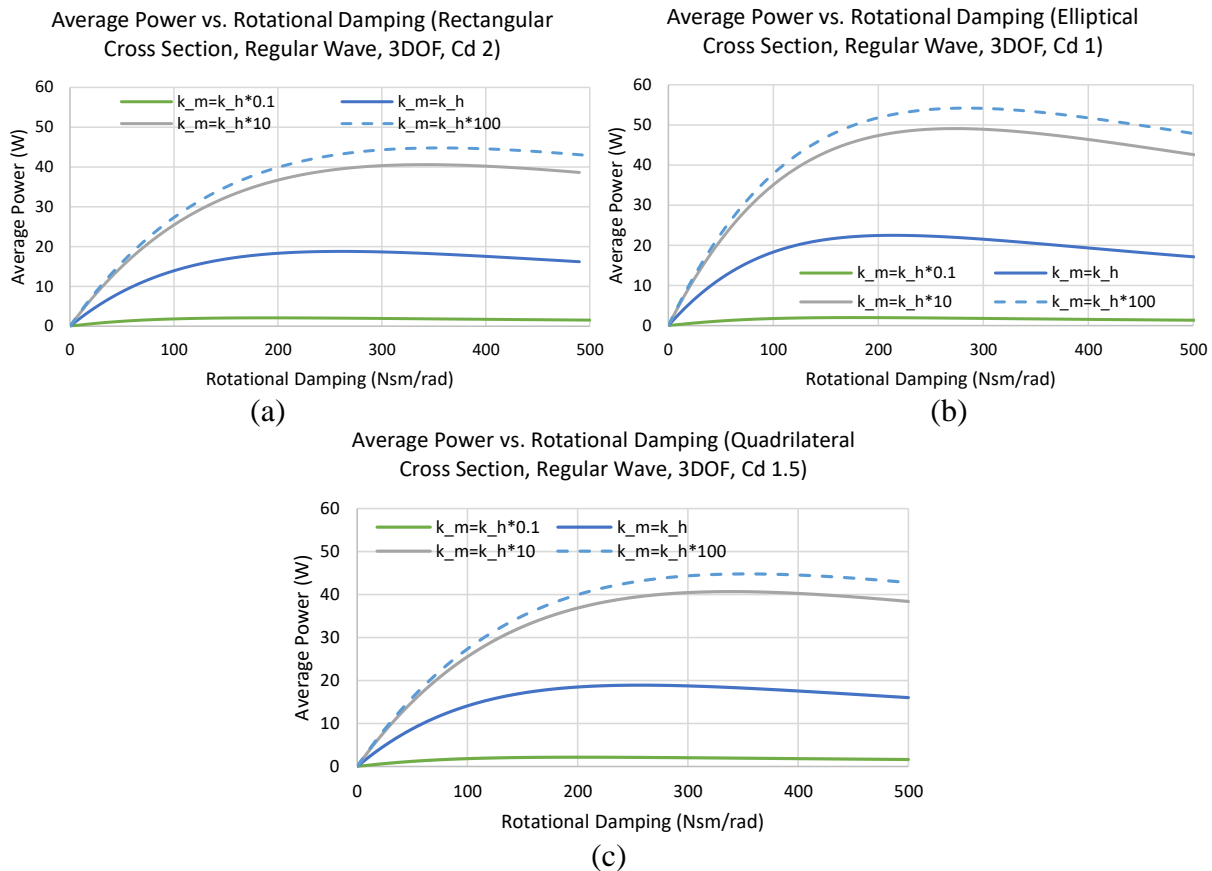


Figure 4.19. 3DOF mooring stiffness study results

4.6 Summary

The aim of this chapter was to develop a power maximization method for a small-sized, two-body attenuator wave energy converter through resonance tuning and numerical modeling. Three different buoy geometries were used for the study with regular and irregular wave conditions. A simplified two-degree-of-freedom (2DOF) model that only allowed pitch was used initially followed by a three-degree-of-freedom (3DOF) model that allowed pitch and heave. The natural frequency was tuned to match the wave frequency for each geometry by adjusting body dimensions to achieve resonance and maximize power generation. After obtaining the

hydrodynamic coefficients in the frequency domain using the BEM solver Ansys AQWA, WEC-Sim was used to perform time domain simulations to determine the optimal damping and maximum power. To demonstrate the effect of drag, four different viscous drag coefficients were used for each geometry. For the 3DOF model, a mooring stiffness study was performed to determine the effect of changing the mooring stiffness.

A major challenge when tuning the device natural frequency to the wave frequency was the small material inertia and added inertia relative to the hydrostatic stiffness. A thin, submerged plate was explored as a method to overcome this problem by increasing added inertia without greatly increasing stiffness. Using the same overall dimension constraint, three typical cross sections were compared: rectangular, elliptical, and quadrilateral. Looking at the 2DOF time domain results, when variation in drag between the shapes was not considered, the difference in power absorption between the shapes was not significant. If an approximate drag coefficient was assigned to each shape, the elliptical cross section had the best power absorption of the three geometries. For the 2DOF model using the approximate drag coefficient comparison, the elliptical shape had a max power of 27.09 W and 7.36% CWR for regular waves and a max power of 8.32 W and 2.26% CWR for irregular waves. For the 3DOF model using the approximate drag coefficient comparison, the elliptical cross section had a max power of 22.52 W and 6.12% CWR for regular waves and 6.18 W and 1.68% CWR for irregular waves. Based on the 3DOF mooring stiffness study with approximate drag coefficients, there was not a significant difference in power between the shapes for low mooring stiffness values, but the elliptical shape had the highest power absorption at larger mooring stiffness values. In addition, the mooring stiffness study illustrated that increased mooring stiffness can be used to increase the relative motion between the bodies and therefore increase the power.

5. Conclusions and Future Work

The goal of this thesis was to examine and optimize the performance of small-sized, oscillating body wave energy converters. Two different types of oscillating body WECs were analyzed: bottom-hinged and attenuator. The objective for the bottom-hinged device was to demonstrate the feasibility of an oscillating surge WEC and desalination system by estimating the system performance through numerical modeling. Using WEC-Sim, the WEC system dynamics and desalination solution-diffusion model were solved simultaneously to estimate the performance under six sea states with different wave conditions. An optimization study was performed under the dominant sea state, W3, to determine the optimal membrane area and needle valve opening height of 0.2 m^2 and $6.0\text{e-}6 \text{ m}$ respectively. Based on the W3 optimized membrane area of 0.2 m^2 , the tuned needle valve opening heights for all six sea states were determined to be $3.0\text{e-}6 \text{ m}$, $4.0\text{e-}6 \text{ m}$, $6.0\text{e-}6 \text{ m}$, $1.1\text{e-}6 \text{ m}$, $1.3\text{e-}5 \text{ m}$, and $1.4\text{e-}5 \text{ m}$.

Using the tuned membrane area and needle valve opening height, irregular wave simulations were performed. The irregular wave simulations illustrated the importance of the accumulator and pressure relief valve to minimize pressure fluctuation and avoid system over-pressurization. According to the irregular wave results, the system will produce desirable amounts of permeate with suitably low concentration and discharge brine effectively. The numerical model estimated that over a 5-day test period, the system will produce 517 L of permeate with 711 ppm concentration, satisfying minimum target requirements of over 400 L permeate and less than 1000 ppm concentration. Preliminary experimental results agreed well with the numerical model, giving permeate salinity of 859 ppm. Some future work for the bottom-hinged device could include adding a second membrane to the numerical model to estimate system performance with two membranes. A wave tank test could also be performed using a physical prototype to further validate the model results.

For the two-body attenuator, the goal was to develop a method of power maximization through resonance tuning and numerical simulation. Using regular and irregular wave conditions, three different buoy cross-section geometries were used for the study: rectangular, elliptical, and quadrilateral. Initially, a simplified two-degree-of-freedom (2DOF) model that only included pitch was used followed by a three-degree of freedom (3DOF) model that included pitch and heave. Four different viscous drag coefficients were used for each geometry to explore the effect of drag. The body dimensions were adjusted for each geometry to maximize power generation by matching the natural frequency to the wave frequency. To overcome the challenge of small material inertia and added inertia relative to hydrostatic stiffness when tuning the natural frequency, a thin, submerged plate was used to increase added inertia without greatly increasing stiffness. WEC-Sim was used to determine optimal PTO damping and maximum power through time domain simulations.

Based on the time domain results, there was not a significant difference in power when variation in drag between the different cross-section geometries was not considered, but the elliptical shape had the highest power if approximate drag coefficients were used. For the 2DOF model with approximate drag coefficients, the elliptical cross section had a max power of 27.09 W and 7.36% CWR for regular waves and a max power of 8.32 W and 2.26% CWR for irregular waves. For the 3DOF model with approximate drag coefficients, the elliptical shape had a max power of 22.52 W and 6.12% CWR for regular waves and 6.18 W and 1.68% CWR for irregular waves. Based on the mooring stiffness variation study for the 3DOF model, there was not much difference in the power results between the different shapes for low mooring stiffness values, but

the elliptical shape had the highest power absorption for larger mooring stiffness values. The mooring stiffness study also demonstrated that increased mooring stiffness can be used to increase relative motion between the bodies in order to increase the power. In the future, additional work could include using computational fluid dynamics (CFD) software to calculate drag coefficients for the different shapes. Also, different wave conditions could be used to examine the device performance with different sea states.

References

- [1] "Water Scarcity." *UN Water*. United Nations, 2021. Web. 17 Apr. 2021.
- [2] WWF. "Water Scarcity." *WWF*. World Wildlife Fund, 2021. Web. 18 Apr. 2021.
- [3] "Water for Life Decade: Water Scarcity." *United Nations*. United Nations, 2014. Web. 18 Apr. 2021.
- [4] "Desalination Worldwide." *Seawater Desalination Huntington Beach Facility*. Poseidon Water, 2018. Web. 18 Apr. 2021.
- [5] "Membrane Desalination Power Usage Put in Perspective." *AMTA*. American Membrane Technology Association, 2016. Web. 18 Apr. 2021.
- [6] "How Much of Each Energy Source Does It Take to Power Your Home?" *McGinley Support Services*. McGinley Support Services, 29 Sept. 2017. Web. 18 Apr. 2021.
- [7] Fouda, A., S. A. Nada, and H. F. Elattar. "An integrated A/C and HDH water desalination system assisted by solar energy: Transient analysis and economical study." *Applied Thermal Engineering* 108 (2016): 1320-1335.
- [8] Falnes, Johannes. "Ocean-Wave Energy." *Johannes Falnes' Web Pages on Wave-energy Teaching*. NTNU, 2016. Web. 18 Apr. 2021.
- [9] Vosough, Amir. "Wave energy." *International journal of multidisciplinary sciences and engineering* 2.7 (2011): 60-63.
- [10] Grimm, Sebastian. "Tides of Transformation: Learnings From the Marine Renewable Energy Sector." *The Bard CEP Eco Reader*. The Bard CEP Eco Reader, 12 Feb. 2021. Web. 20 Apr. 2021.
- [11] Jacobson, Paul T, Hagerman, George, and Scott, George. "Mapping and Assessment of the United States Ocean Wave Energy Resource". United States: N. p., 2011. Web. doi:10.2172/1060943.
- [12] Mafi-Gholami, Davood, et al. "Vulnerability of coastal communities to climate change: Thirty-year trend analysis and prospective prediction for the coastal regions of the Persian Gulf and Gulf of Oman." *Science of the Total Environment* 741 (2020): 140305.
- [13] Huckerby, Jhon, et al. "An international vision for ocean energy." *Ocean energy systems implementing agreement* (2011).
- [14] Aderinto, Tunde, and Hua Li. "Ocean wave energy converters: Status and challenges." *Energies* 11.5 (2018): 1250.

- [15] "Global Wave Energy Industry (2020 to 2025) - Increasing R&D Investment and Focus on Clean Energy Generation Presents Opportunities." *GlobeNewswire*. Research and Markets, 29 Apr. 2020. Web. 18 Apr. 2021.
- [16] Liu, Yijin, et al. "Comparison study of tidal stream and wave energy technology development between China and some Western Countries." *Renewable and Sustainable Energy Reviews* 76 (2017): 701-716.
- [17] Titah-Benbouzid, Hosna, and Mohamed Benbouzid. "Ocean wave energy extraction: Up-to-date technologies review and evaluation." *2014 International Power Electronics and Application Conference and Exposition*. IEEE, 2014.
- [18] Prakash, S. S., et al. "Wave energy converter: a review of wave energy conversion technology." *2016 3rd Asia-Pacific World Congress on Computer Science and Engineering (APWC on CSE)*. IEEE, 2016.
- [19] Falcão, António FO, and Joao CC Henriques. "Oscillating-water-column wave energy converters and air turbines: A review." *Renewable Energy* 85 (2016): 1391-1424.
- [20] Vertechy, R., et al. "Oscillating-water-column wave-energy-converter based on dielectric elastomer generator." *Electroactive Polymer Actuators and Devices (EAPAD) 2013*. Vol. 8687. International Society for Optics and Photonics, 2013.
- [21] Vicinanza, Diego, et al. "Review of innovative harbor breakwaters for wave-energy conversion." *Journal of Waterway, Port, Coastal, and Ocean Engineering* 145.4 (2019): 03119001.
- [22] Takahashi, Shigeo, et al. "Wave power conversion by a prototype wave power extracting caisson in Sakata port." *Coastal Engineering* 1992. 1993. 3440-3453.
- [23] António, F. de O. "Modelling and control of oscillating-body wave energy converters with hydraulic power take-off and gas accumulator." *Ocean engineering* 34.14-15 (2007): 2021-2032.
- [24] "WaveRoller Solution." *AW Energy*. AW Energy, 2021. Web. 19 Apr. 2021.
- [25] Al Shami, Elie, Ran Zhang, and Xu Wang. "Point absorber wave energy harvesters: A review of recent developments." *Energies* 12.1 (2019): 47.
- [26] Voorhis, Rachel. "Point Absorbers: The Technology and Innovations." *Energy and the Environment-A Coastal Perspective*. Energy and the Environment-A Coastal Perspective, 25 July 2012. Web. 19 Apr. 2021.
- [27] López, Iraide, et al. "Review of wave energy technologies and the necessary power-equipment." *Renewable and sustainable energy reviews* 27 (2013): 413-434.

- [28] Alamian, Rezvan, et al. "Evaluation of technologies for harvesting wave energy in Caspian Sea." *Renewable and sustainable energy reviews* 32 (2014): 468-476.
- [29] Gomes, R. P. F., et al. "The dynamics and power extraction of bottom-hinged plate wave energy converters in regular and irregular waves." *Ocean Engineering* 96 (2015): 86-99.
- [30] Bevilacqua, Giovanna, and Barbara Zanuttigh. "Overtopping Wave Energy Converters: general aspects and stage of development." (2011).
- [31] Liu, Zhen, et al. "Experimental study on multi-level overtopping wave energy convertor under regular wave conditions." *International Journal of Naval Architecture and Ocean Engineering* 10.5 (2018): 651-659.
- [32] Blažauskas, Nerijus, Aleksas Pašilis, and Audrius Knolis. "Potential applications for small scale wave energy installations." *Renewable and Sustainable Energy Reviews* 49 (2015): 297-305.
- [33] LiVecchi, A., et al. "Powering the blue economy; exploring opportunities for marine renewable energy in maritime markets." *US Department of Energy, Office of Energy Efficiency and Renewable Energy. Washington, DC* (2019): 207.
- [34] "Guidelines: Waves to Water: Wave-powered Desalination Challenge." *HeroX. American-Made Challenges*, 2021. Web. 19 Apr. 2021.
- [35] "Powering the Blue Economy: Ocean Observing Prize." *American-Made Challenges. American-Made Challenges*, 2021. Web. 19 Apr. 2021.
- [36] Lienhard, John H., et al. "Thermodynamics, exergy, and energy efficiency in desalination systems." (2017).
- [37] Lin, Shihong. "Energy efficiency of desalination: fundamental insights from intuitive interpretation." *Environmental science & technology* 54.1 (2019): 76-84.
- [38] Van der Bruggen, Bart, et al. "A review of pressure-driven membrane processes in wastewater treatment and drinking water production." *Environmental progress* 22.1 (2003): 46-56.
- [39] Rao, Sudhakar M. "Reverse osmosis." *Resonance* 12.5 (2007): 37-40.
- [40] Feher, Joseph J. *Quantitative human physiology: an introduction*. Academic press, 2017.
- [41] Selatile, Mantsopa Koena, et al. "Recent developments in polymeric electrospun nanofibrous membranes for seawater desalination." *RSC advances* 8.66 (2018): 37915-37938.
- [42] "Reverse Osmosis Basics." *TORAY. TORAY*. Web. 19 Apr. 2021.

- [43] Garud, R. M., et al. "A Short Review on Process and Applications of Reverse Osmosis." *Universal Journal of Environmental Research & Technology* 1.3 (2011).
- [44] Daal, L., et al. "Membrane technologies for water treatment and reuse in the power industries." *Advances in Membrane Technologies for Water Treatment*. Woodhead Publishing, 2015. 605-624.
- [45] Maynard, E., and C. Whapham. "Quality and supply of water used in hospitals." *Decontamination in Hospitals and Healthcare*. Woodhead Publishing, 2020.
- [46] Lin, Shihong, and Menachem Elimelech. "Staged reverse osmosis operation: Configurations, energy efficiency, and application potential." *Desalination* 366 (2015): 9-14.
- [47] "What Is Reverse Osmosis?" *Puretec Industrial Water*. Web. 26 May 2021.
- [48] Folaranmi, Gbenro, et al. "Towards Electrochemical Water Desalination Techniques: A Review on Capacitive Deionization, Membrane Capacitive Deionization and Flow Capacitive Deionization." *Membranes* 10.5 (2020): 96.
- [49] "Electrodialysis Using Ion Exchange Membranes." *United Nations Industrial Development Organization*. Web. 26 May 2021.
- [50] Tonner, John. *Barriers to Thermal Desalinization in the United States*. US Department of the Interior, Bureau of Reclamation, Technical Service Center, Water and Environmental Services Division, Water Treatment Engineering Research Team, 2008.
- [51] Xu, Ben, Peiwen Li, and Penghua Guo. "Solar Thermal-Driven Desalination Pursuing Products of Pure Water and Salts and Leaving Minimum Impact to Environment." *Desalination* (2017): 143.
- [52] Warsinger, David M., et al. "Entropy generation of desalination powered by variable temperature waste heat." *Entropy* 17.11 (2015): 7530-7566.
- [53] "Multistage Flash Distillation." *Desalination World*. Desalination World. Web. 19 Apr. 2021.
- [54] Deshmukh, Akshay, et al. "Membrane distillation at the water-energy nexus: limits, opportunities, and challenges." *Energy & Environmental Science* 11.5 (2018): 1177-1196.
- [55] "Ocean Waves." *Oceanography GEOS 3401*. UT Dallas. Web. 18 Apr. 2021.
- [56] Das, S. K., S. N. Das, and P. K. Sahoo. "Investigation of coupled sway, roll and yaw motions of a floating body: numerical modelling for non-linear roll restoring." *Ships and Offshore Structures* 3.1 (2008): 49-56.

- [57] WEC-Sim (Wave Energy Converter SIMulator). (2020). National Renewable Energy Laboratory (NREL) and Sandia National Laboratories.
- [58] 2020, "ANSYS AQWA 2020 R2 AQWA User's Manual."
- [59] "Linearized (Airy) Wave Theory." *mit.edu*. MIT. Web. 19 Apr. 2021.
- [60] Young, Ian R. "Regular, Irregular Waves and the Wave Spectrum." *Encyclopedia of Maritime and Offshore Engineering* (2017): 1-10.
- [61] Chakrabarti, Subrata Kumar. *Hydrodynamics of offshore structures*. WIT press, 1987.
- [62] Martin, Dillon Minkoff. *Hydrodynamic design optimization and wave tank testing of self-reacting two-body wave energy converter*. Diss. Virginia Tech, 2017.
- [63] Babarit, Aurélien. "A database of capture width ratio of wave energy converters." *Renewable Energy* 80 (2015): 610-628.
- [64] Penalba, Markel, Thomas Kelly, and John Ringwood. "Using NEMOH for modelling wave energy converters: A comparative study with WAMIT." (2017).
- [65] Whittaker, Trevor, and Matt Folley. "Nearshore oscillating wave surge converters and the development of Oyster." *Philosophical Transactions of the Royal Society A: Mathematical, Physical and Engineering Sciences* 370.1959 (2012): 345-364.
- [66] Chow, Yi-Chih, et al. "Parametric design methodology for maximizing energy capture of a bottom-hinged flap-type WEC with medium wave resources." *Renewable energy* 126 (2018): 605-616.
- [67] Tom, N. M., et al. "Development of a nearshore oscillating surge wave energy converter with variable geometry." *Renewable Energy* 96 (2016): 410-424.
- [68] Yu, Yi-Hsiang, and Dale Jenne. "Numerical modeling and dynamic analysis of a wave-powered reverse-osmosis system." *Journal of Marine Science and Engineering* 6.4 (2018): 132.
- [69] Flippo, Walt, and Bob Rajabi. "Reduce Hydraulic Accumulator Cost with Back-Up Gas Bottles." *Mobile Hydraulic Tips*. Mobile Hydraulic Tips, 2010. Web. 19 Apr. 2021.
- [70] Energy—Wave, IEC Marine. "Tidal and Other Water Current Converters—Part 2: Design Requirements for Marine Energy Systems." *IEC TS* (2016): 62600-2.
- [71] Baker, Richard W. *Membrane technology and applications*. John Wiley & Sons, 2012.

- [72] Lin, Shihong, and Menachem Elimelech. "Kinetics and energetics trade-off in reverse osmosis desalination with different configurations." *Desalination* 401 (2017): 42-52.
- [73] Dallman, Ann R., and Vincent S. Neary. "Characterization of us wave energy converter (wec) test sites: A catalogue of met-ocean data." *Sandia National Laboratories, Albuquerque, NM* (2014).
- [74] Zheng, Si-Ming, et al. "Numerical study on the dynamics of a two-raft wave energy conversion device." *Journal of Fluids and Structures* 58 (2015): 271-290.
- [75] Liu, ChangHai, QingJun Yang, and Gang Bao. "Performance investigation of a two-raft-type wave energy converter with hydraulic power take-off unit." *Applied Ocean Research* 62 (2017): 139-155.
- [76] So, Ratanak, et al. "Statistical analysis of a 1: 7 scale field test wave energy converter using WEC-sim." *IEEE Transactions on Sustainable Energy* 8.3 (2017): 1118-1126.
- [77] Wang, L., and John V. Ringwood. "Geometric optimization of a hinge-barge wave energy converter." *Proceedings of the 13th European Wave and Tidal Energy Conference, Naples, Italy*. 2019.
- [78] Li, Biao, Fangfang Sui, and Bingsong Yang. "An efficient multi-factor geometry optimization based on motion analysis and resonance response for hinged double-body floating wave energy converter." *Science Progress* 103.3 (2020): 0036850420950151.
- [79] Li, Qiaofeng, et al. "A self-floating oscillating surge wave energy converter." *Energy* (2021): 120668.
- [80] Heras, Pilar, et al. "Numerical and experimental modelling of a wave energy converter pitching in close proximity to a fixed structure." *Journal of Marine Science and Engineering* 7.7 (2019): 218.
- [81] Hoerner, Sighard F. "Fluid-Dynamic Drag. Theoretical, experimental and statistical information." *Copyright by: SF Hoerner Fluid Dynamics, Vancouver, Printed in the USA, Card Number 64-19666* (1965).
- [82] Guillou, Nicolas. "Estimating wave energy flux from significant wave height and peak period." *Renewable Energy* 155 (2020): 1383-1393.

Appendices

Appendix A: W3 Optimization Study Results

Table A1: W3 Optimization Study Average System Pressure (Pa)

		NV Opening Height (m)													
		5.0E-07	1.0E-06	1.5E-06	2.0E-06	2.5E-06	3.0E-06	3.5E-06	4.0E-06	4.5E-06	5.0E-06	5.5E-06	6.0E-06	6.5E-06	7.0E-06
Membrane Area (m ²)	0.1	6.57E+06	6.55E+06	6.20E+06	6.48E+06	6.43E+06	6.35E+06	6.23E+06	6.06E+06	5.84E+06	5.57E+06	5.25E+06	4.94E+06	4.64E+06	4.35E+06
	0.2	6.32E+06	6.21E+06	6.06E+06	5.90E+06	5.70E+06	5.48E+06	5.26E+06	5.03E+06	4.82E+06	4.61E+06	4.41E+06	4.23E+06	4.05E+06	3.88E+06
	0.3	5.59E+06	5.42E+06	5.25E+06	5.07E+06	4.91E+06	4.75E+06	4.59E+06	4.45E+06	4.30E+06	4.16E+06	4.03E+06	3.90E+06	3.77E+06	3.65E+06
	0.4	4.96E+06	4.83E+06	4.71E+06	4.58E+06	4.46E+06	4.35E+06	4.23E+06	4.12E+06	4.02E+06	3.91E+06	3.81E+06	3.71E+06	3.61E+06	3.52E+06
	0.5	4.58E+06	4.48E+06	4.38E+06	4.28E+06	4.19E+06	4.10E+06	4.01E+06	3.92E+06	3.83E+06	3.75E+06	3.67E+06	3.59E+06	3.51E+06	3.43E+06
	0.6	4.32E+06	4.23E+06	4.15E+06	4.08E+06	4.00E+06	3.92E+06	3.85E+06	3.78E+06	3.71E+06	3.64E+06	3.57E+06	3.50E+06	3.44E+06	3.37E+06

Table A2. W3 Optimization Study: Average Permeate Flow Rate (m³/s)

		NV Opening Height (m)													
		5.0E-07	1.0E-06	1.5E-06	2.0E-06	2.5E-06	3.0E-06	3.5E-06	4.0E-06	4.5E-06	5.0E-06	5.5E-06	6.0E-06	6.5E-06	7.0E-06
Membrane Area (m ²)	0.1	1.43E-06	1.42E-06	1.41E-06	1.39E-06	1.37E-06	1.34E-06	1.29E-06	1.22E-06	1.14E-06	1.03E-06	9.02E-07	7.76E-07	6.54E-07	5.38E-07
	0.2	2.65E-06	2.57E-06	2.45E-06	2.32E-06	2.16E-06	1.99E-06	1.81E-06	1.63E-06	1.45E-06	1.29E-06	1.13E-06	9.81E-07	8.38E-07	7.02E-07
	0.3	3.11E-06	2.90E-06	2.69E-06	2.49E-06	2.29E-06	2.10E-06	1.91E-06	1.73E-06	1.50E-06	1.40E-06	1.23E-06	1.08E-06	9.29E-07	7.84E-07
	0.4	3.14E-06	2.93E-06	2.73E-06	2.53E-06	2.34E-06	2.16E-06	1.97E-06	1.80E-06	1.62E-06	1.46E-06	1.30E-06	1.14E-06	9.84E-07	8.34E-07
	0.5	3.15E-06	2.95E-06	2.75E-06	2.56E-06	2.37E-06	2.19E-06	2.01E-06	1.84E-06	1.67E-06	1.50E-06	1.34E-06	1.18E-06	1.02E-06	8.68E-07
	0.6	3.16E-06	2.96E-06	2.77E-06	2.58E-06	2.40E-06	2.22E-06	2.04E-06	1.87E-06	1.70E-06	1.53E-06	1.36E-06	1.20E-06	1.05E-06	8.93E-07

Table A3. W3 Optimization Study: Average Permeate Concentration (ppm)

		NV Opening Height (m)													
		5.0E-07	1.0E-06	1.5E-06	2.0E-06	2.5E-06	3.0E-06	3.5E-06	4.0E-06	4.5E-06	5.0E-06	5.5E-06	6.0E-06	6.5E-06	7.0E-06
Membrane Area (m ²)	0.1	182.88	183.86	185.49	187.86	191.15	196.54	205.09	218.36	238.13	267.54	309.95	367.36	446.80	563.74
	0.2	195.68	203.26	213.97	227.61	246.21	269.78	298.50	333.36	375.87	428.28	494.58	581.62	702.14	884.86
	0.3	251.62	270.45	292.34	317.35	346.03	379.24	418.17	464.44	520.45	589.77	678.29	796.38	965.78	1249.35
	0.4	328.29	352.37	379.52	410.39	445.78	486.79	534.91	592.30	662.05	749.08	861.70	1016.22	1255.19	1617.85
	0.5	403.54	432.07	464.25	500.82	542.81	591.55	648.88	717.48	801.40	907.21	1046.93	1248.57	1690.29	2093.92
	0.6	476.62	509.47	546.55	588.76	637.26	693.65	760.23	840.25	938.87	1064.94	1236.74	1516.26	2538.39	9377.29

Table A4. W3 Optimization Study: Average Recovery

		NV Opening Height (m)													
		5.0E-07	1.0E-06	1.5E-06	2.0E-06	2.5E-06	3.0E-06	3.5E-06	4.0E-06	4.5E-06	5.0E-06	5.5E-06	6.0E-06	6.5E-06	7.0E-06
Membrane Area (m ²)	0.1	0.85	0.74	0.66	0.59	0.53	0.48	0.43	0.39	0.35	0.31	0.27	0.23	0.19	0.16
	0.2	0.92	0.84	0.77	0.71	0.65	0.59	0.53	0.48	0.43	0.38	0.33	0.29	0.24	0.20
	0.3	0.93	0.86	0.80	0.74	0.68	0.62	0.56	0.51	0.46	0.41	0.36	0.31	0.27	0.22
	0.4	0.93	0.87	0.81	0.75	0.69	0.64	0.58	0.53	0.48	0.42	0.38	0.33	0.28	0.24
	0.5	0.94	0.88	0.82	0.76	0.70	0.65	0.59	0.54	0.49	0.44	0.39	0.34	0.29	0.24
	0.6	0.94	0.88	0.82	0.76	0.71	0.65	0.60	0.54	0.49	0.44	0.39	0.34	0.30	0.25

20-25% Recovery

26-30% Recovery

Table A5. W3 Optimization Study: 5-Day Permeate Volume (L)

		NV Opening Height (m)													
		5.0E-07	1.0E-06	1.5E-06	2.0E-06	2.5E-06	3.0E-06	3.5E-06	4.0E-06	4.5E-06	5.0E-06	5.5E-06	6.0E-06	6.5E-06	7.0E-06
Membrane Area (m ²)	0.1	617.76	613.44	609.12	600.48	591.84	578.88	557.28	527.04	492.48	444.96	389.66	335.23	282.53	232.42
	0.2	1144.80	1110.24	1058.40	1002.24	933.12	859.68	781.92	704.16	626.40	557.28	488.16	423.79	362.02	303.26
	0.3	1343.52	1252.80	1162.08	1075.68	989.28	907.20	825.12	747.36	648.00	604.80	531.36	466.56	401.33	338.69
	0.4	1356.48	1265.76	1179.36	1092.96	1010.88	933.12	851.04	777.60	699.84	630.72	561.60	492.48	425.09	360.29
	0.5	1360.80	1274.40	1188.00	1105.92	1023.84	946.08	868.32	794.88	721.44	648.00	578.88	509.76	440.64	374.98
	0.6	1365.12	1278.72	1196.64	1114.56	1036.80	959.04	881.28	807.84	734.40	660.96	587.52	518.40	453.60	385.78

Appendix B: Combined System Pressure and Permeate Flow Rate Plots, Irregular Wave

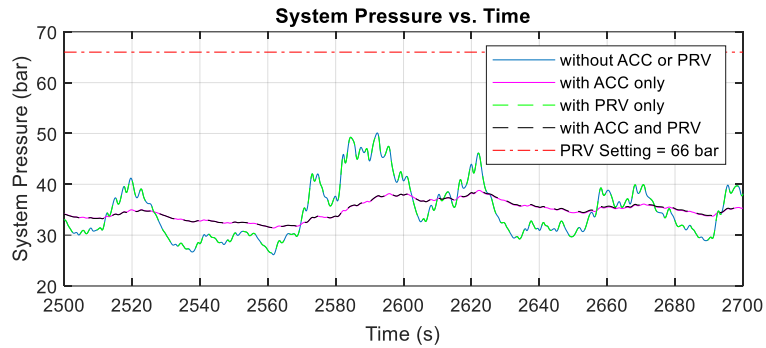


Figure B1(a). System Pressure vs. Time Combined Plots, W1 irregular wave

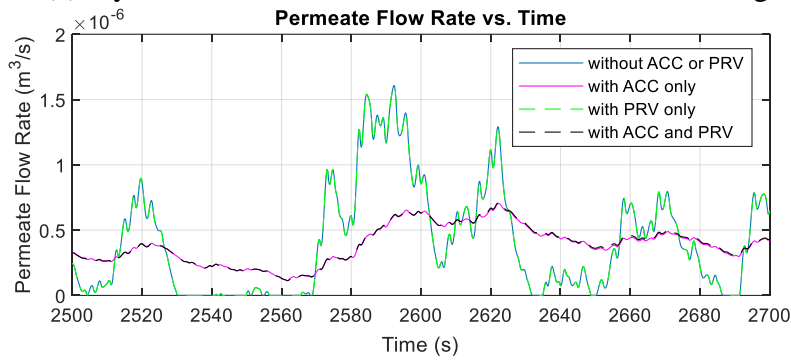


Figure B1(b) Permeate Flow Rate vs. Time Combined Plots, W1 irregular wave

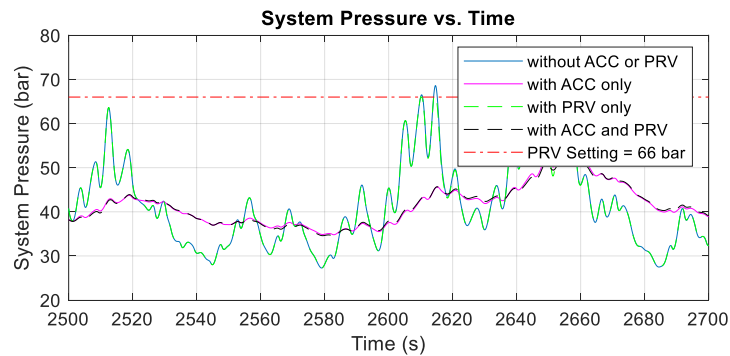


Figure B2(a). System Pressure vs. Time Combined Plots, W2 irregular wave

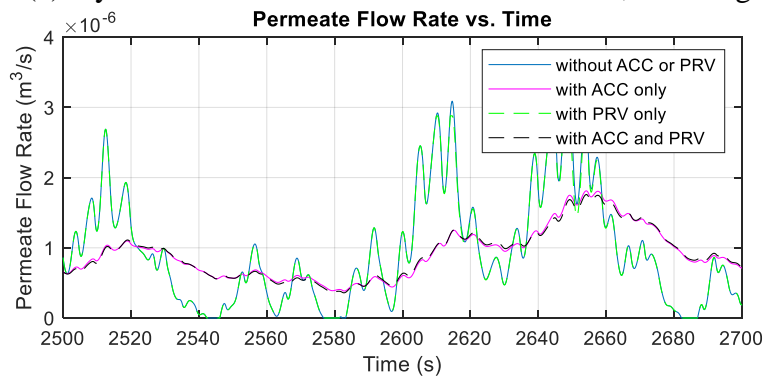


Figure B2(b) Permeate Flow Rate vs. Time Combined Plots, W2 irregular wave

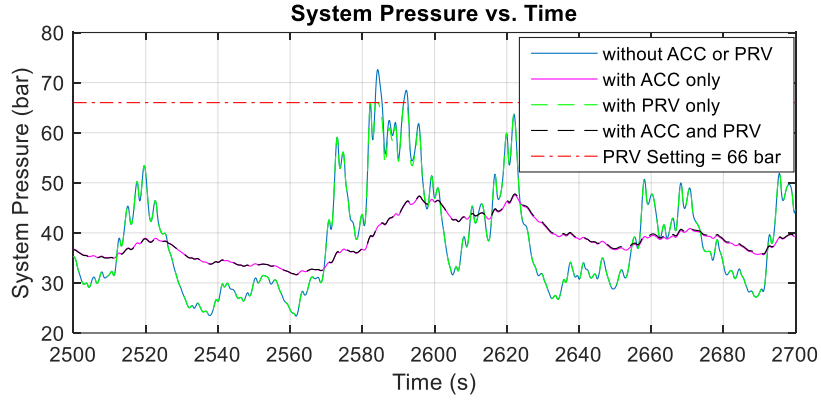


Figure B3(a). System Pressure vs. Time Combined Plots, W3 irregular wave

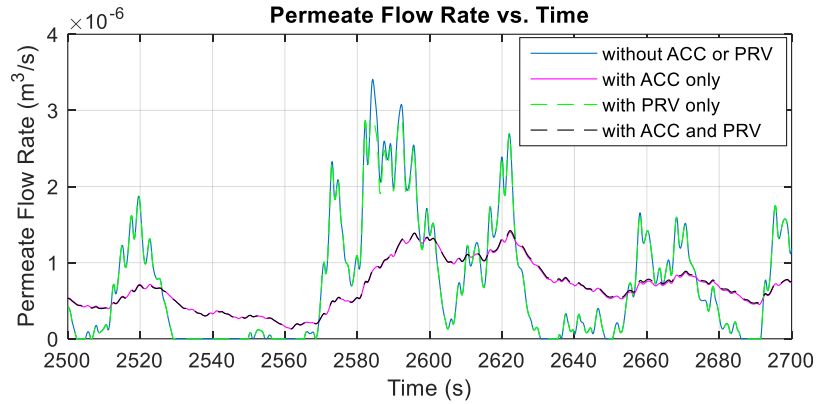


Figure B3(b) Permeate Flow Rate vs. Time Combined Plots, W3 irregular wave

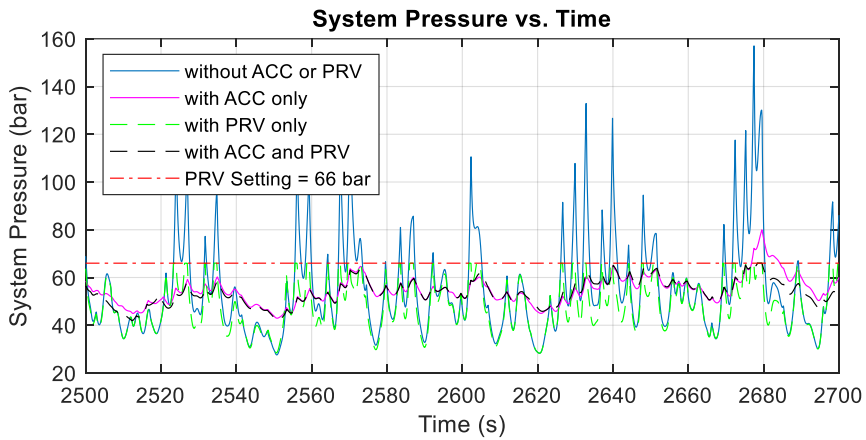


Figure B4(a). System Pressure vs. Time Combined Plots, W4 irregular wave

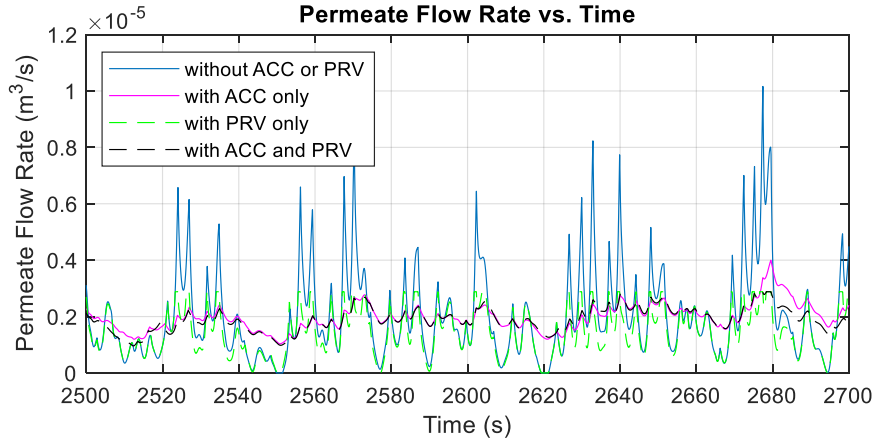


Figure B4(b) Permeate Flow Rate vs. Time Combined Plots, W4 irregular wave

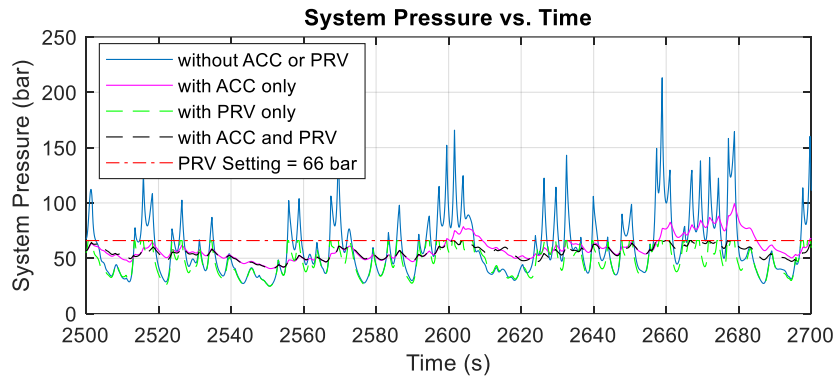


Figure B5(a). System Pressure vs. Time Combined Plots, W5 irregular wave

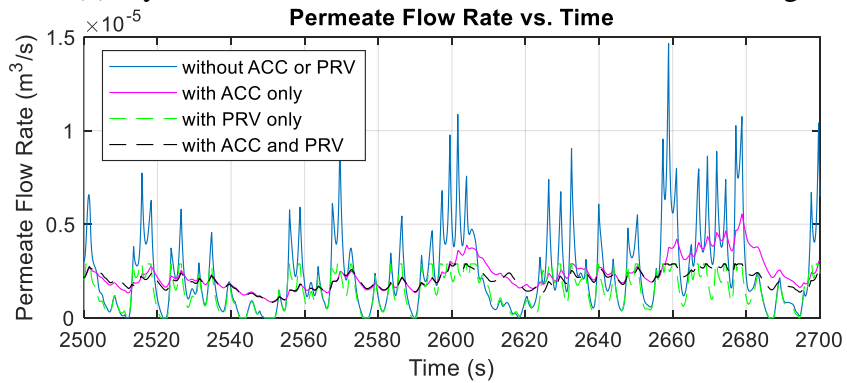


Figure B5(b) Permeate Flow Rate vs. Time Combined Plots, W5 irregular wave

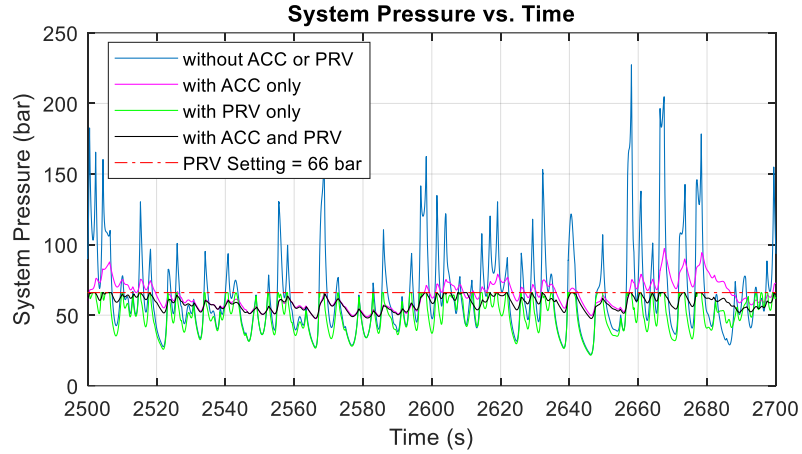


Figure B6(a). System Pressure vs. Time Combined Plots, W6 irregular wave

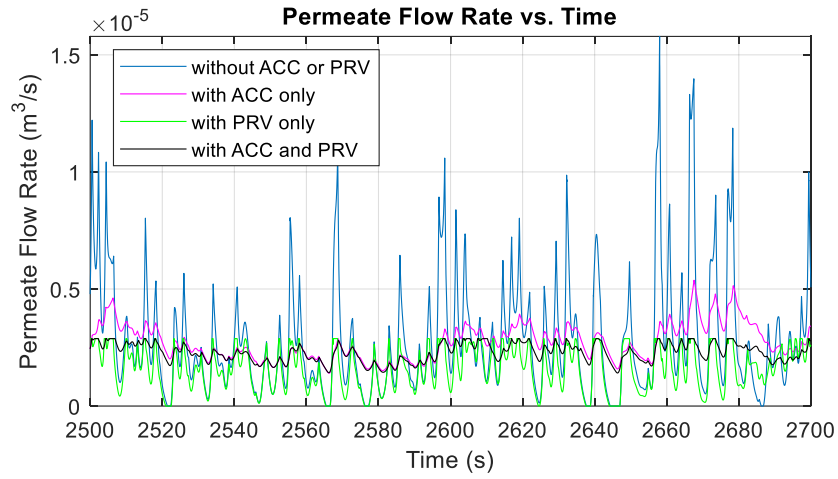


Figure B6(b) Permeate Flow Rate vs. Time Combined Plots, W6 irregular wave

Appendix C: Full Simulation Results, Irregular Wave (w/ ACC and PRV)

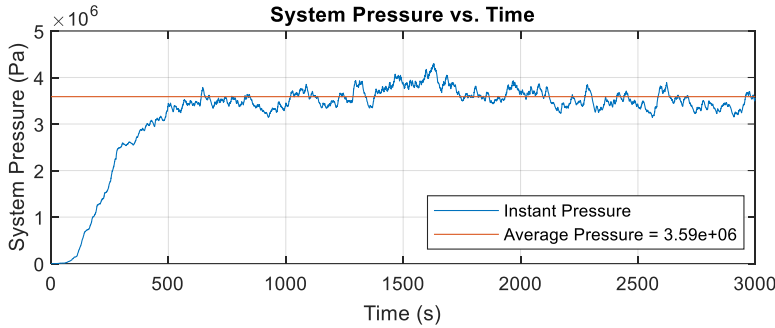


Figure C1(a)

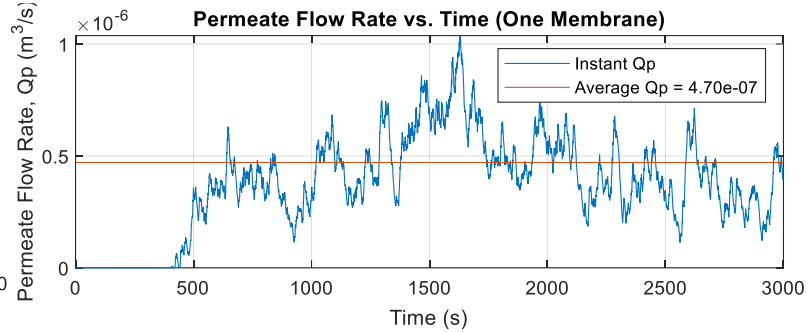


Figure C1(b)

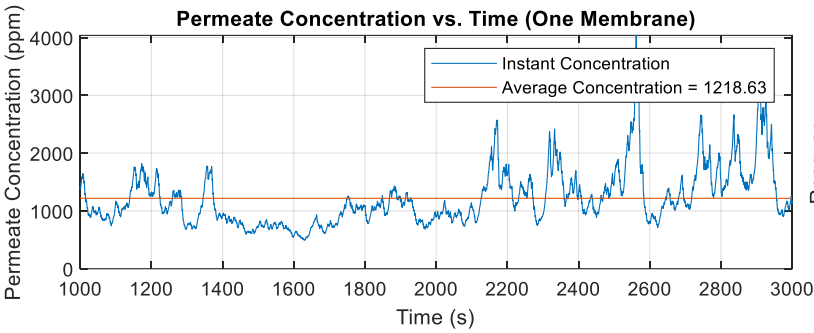


Figure C1(c)

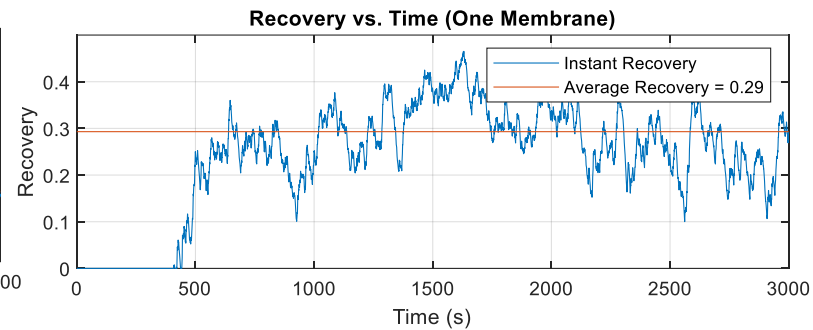


Figure C1(d)

Figure C1. Full Simulation Results, W1 Irregular Wave (w/ ACC and PRV)

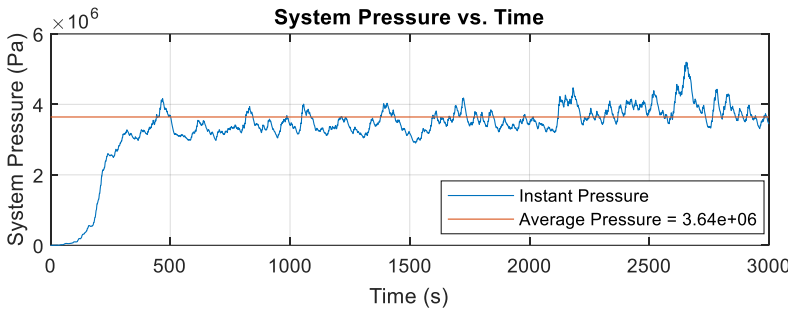


Figure C2(a)

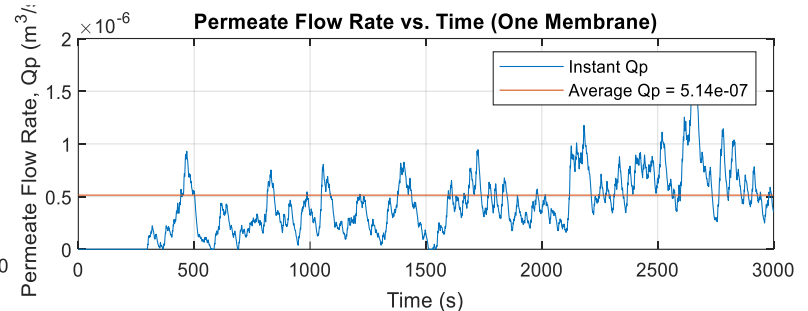


Figure C2(b)

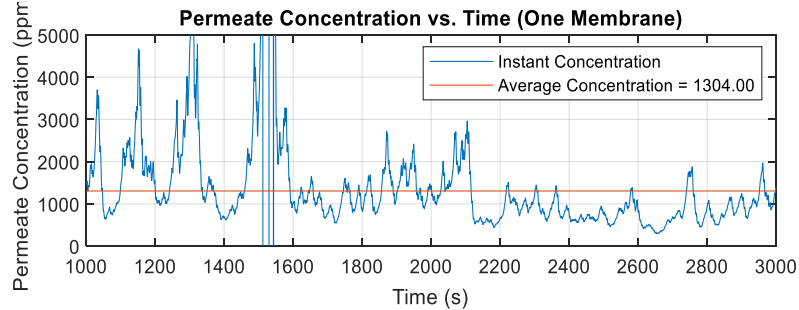


Figure C2(c)

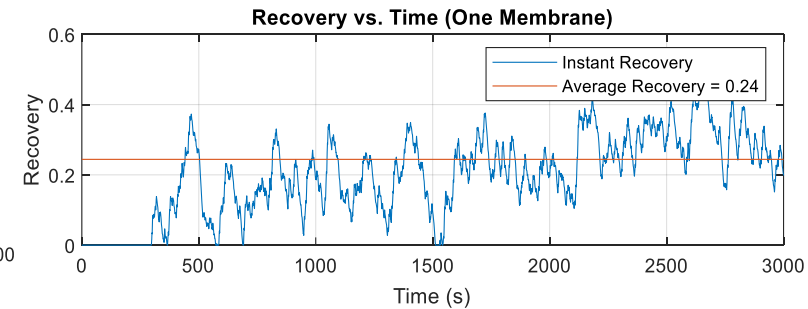


Figure C2(d)

Figure C2. Full Simulation Results, W2 Irregular Wave (w/ ACC and PRV)

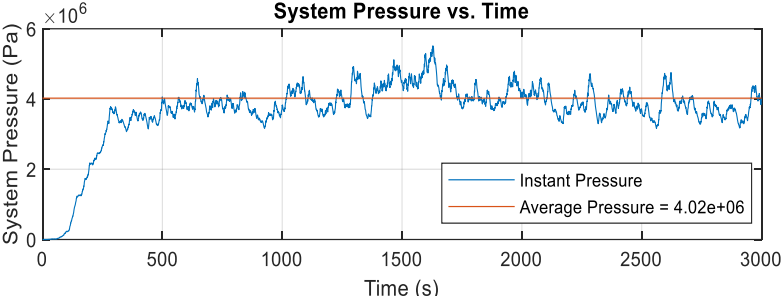


Figure C3(a)

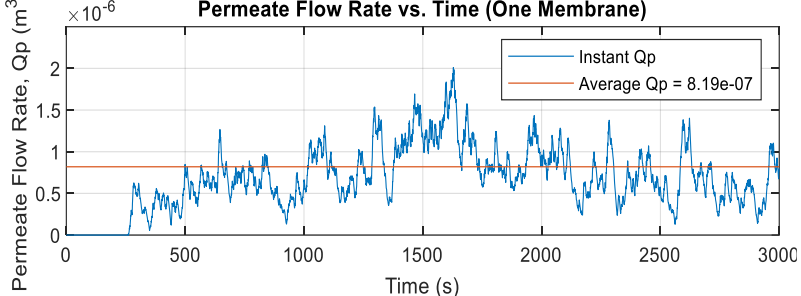


Figure C3(b)

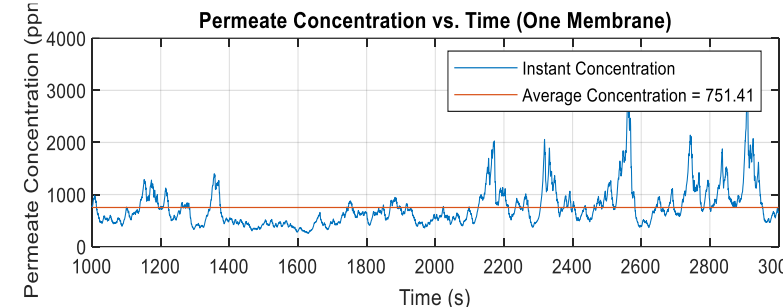


Figure C3(c)

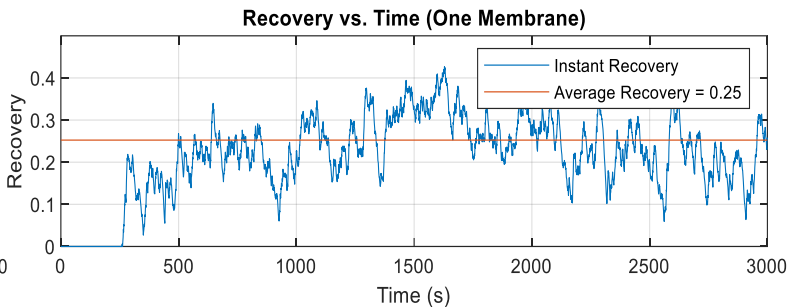


Figure C3(d)

Figure C3. Full Simulation Results, W3 Irregular Wave (w/ ACC and PRV)

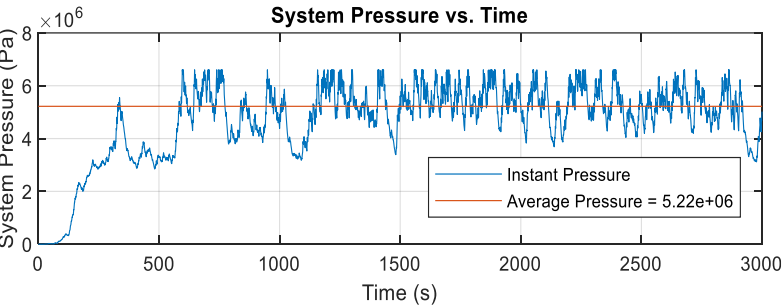


Figure C4(a)

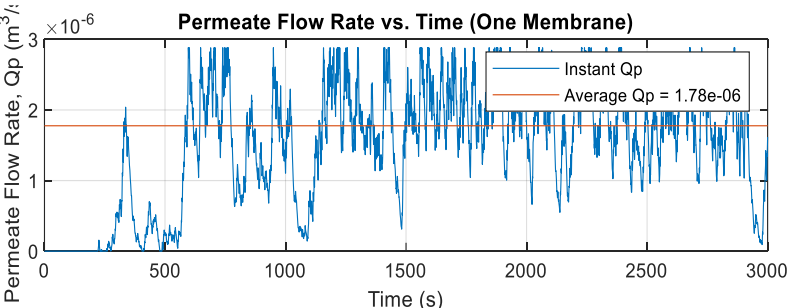


Figure C4(b)

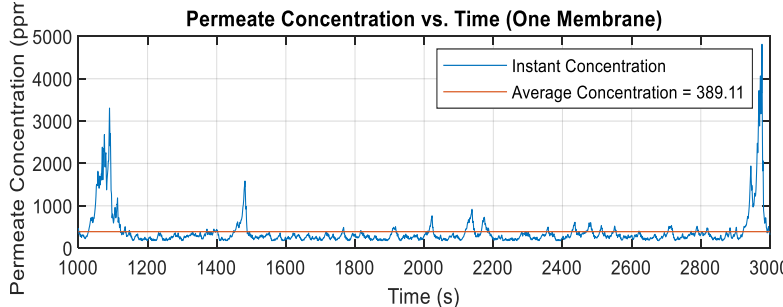


Figure C4(c)

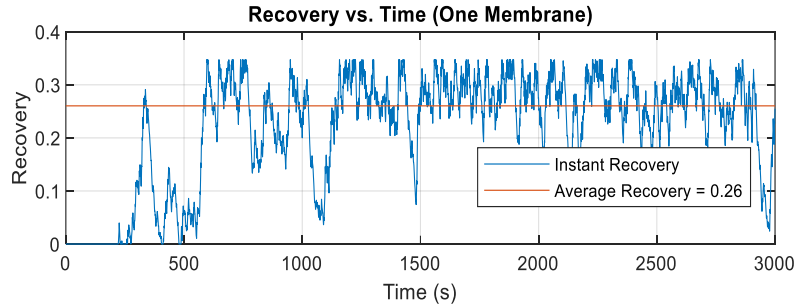


Figure C4(d)

Figure C4. Full Simulation Results, W4 Irregular Wave (w/ ACC and PRV)

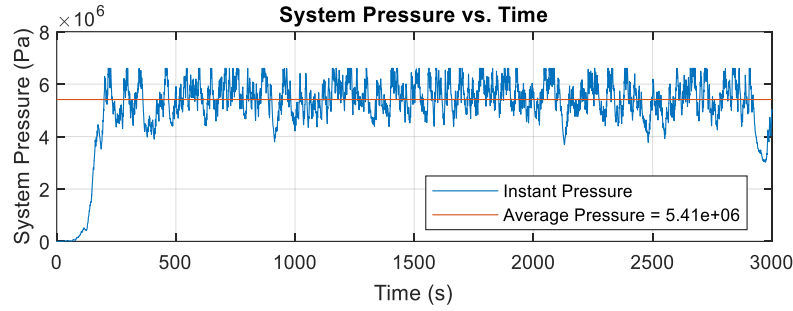


Figure C5(a)

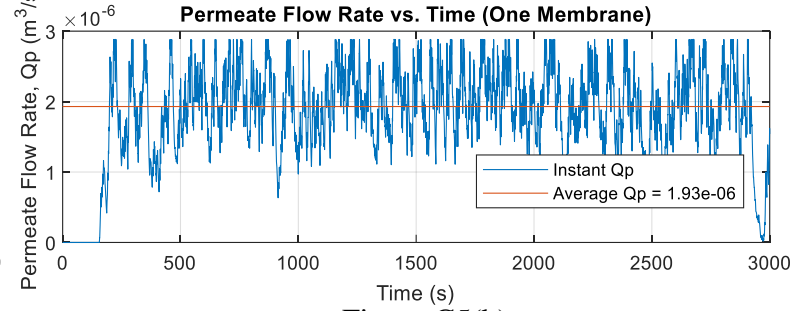


Figure C5(b)

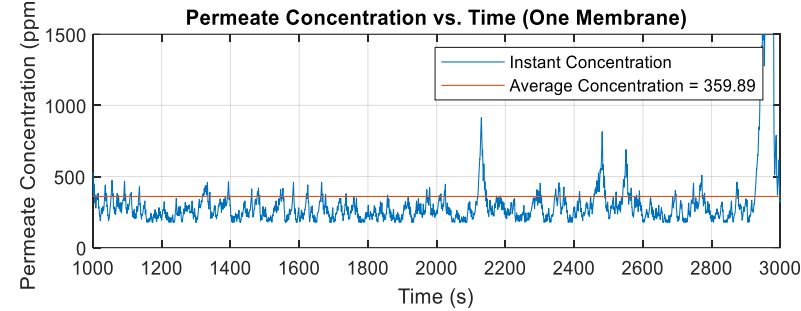


Figure C5(c)

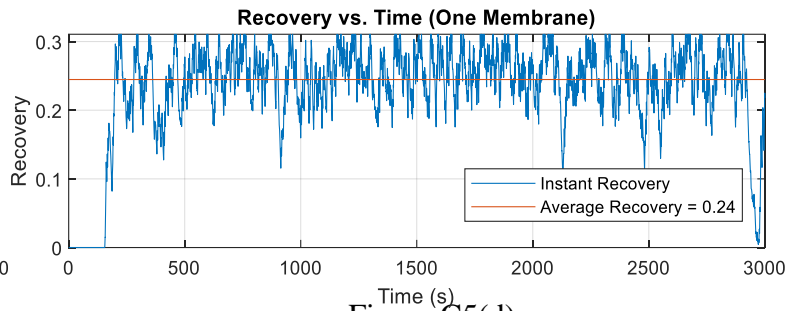


Figure C5(d)

Figure C5. Full Simulation Results, W5 Irregular Wave (w/ ACC and PRV)

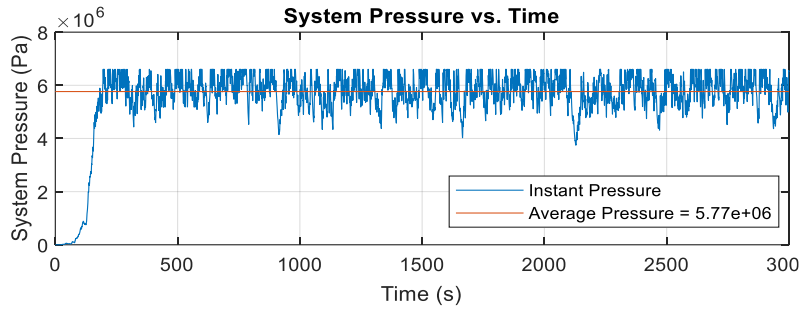


Figure C6(a)

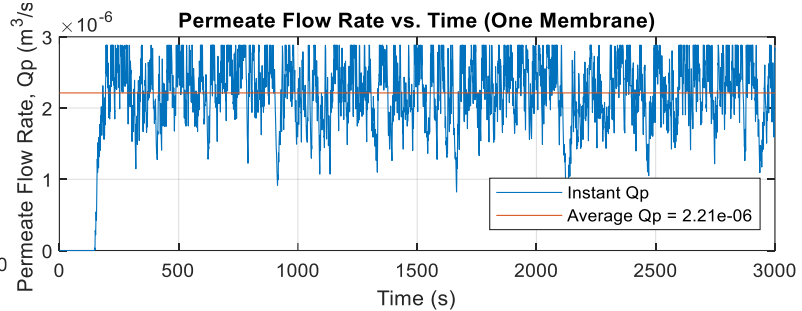


Figure C6(b)

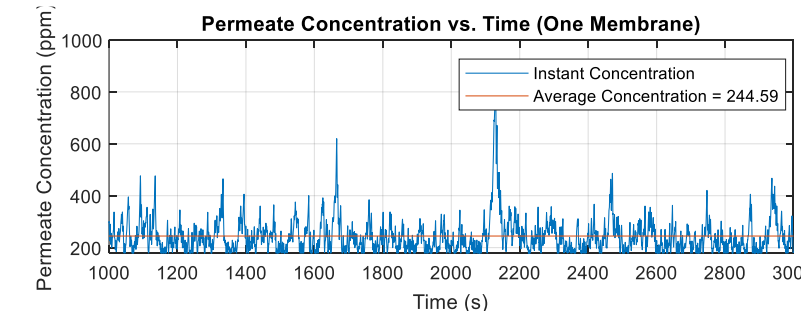


Figure C6(c)

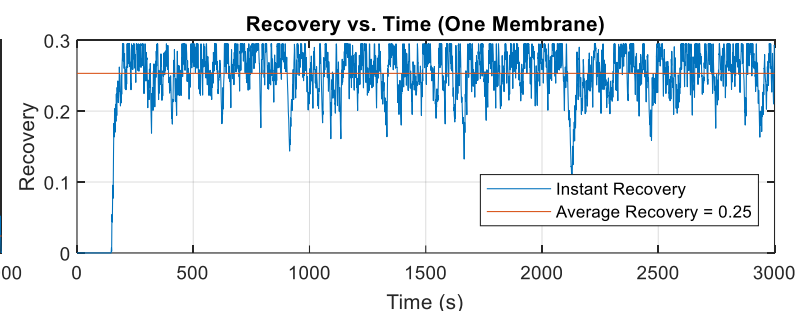


Figure C6(d)

Figure C6. Full Simulation Results, W6 Irregular Wave (w/ ACC and PRV)